Politecnico di Torino
Master's degree in Nanotechnologies for ICTs

Politecnico
di Torino

Bulk and surface modifications for highly efficient and stable medium-bandgap hybrid perovskite solar cells

Author: **Sara Salera**

Student ID: 302951
Advisor: Prof. Matteo Cocuzza
Co-advisor: Dr. Yinghuan Kuang
Academic Year: 2023-24

Acknowledgements

I would like to express my sincere gratitude to Dr.Yinghuan Kuang and Dr. Tom Aernouts, who provided me with the invaluable opportunity to undertake this project within the esteemed research group at EnergyVille.
This work would not be possible without the enduring help and assistance of Cristian Villalobos Meza, who patiently supported and guided me throughout the journey of completing this thesis.
I would also like to extend my gratitude to all the colleagues in Energy Ville, who helped and supported me, both practically and emotionally, especially during the (several) rainy days in Genk.

I would like to acknowledge Prof. Cocuzza for his prompt communication and reassuring words, which provided me with much-needed encouragement and tranquility throughout this process.

Finally, I would like to dedicate this thesis to those who I hold dear to my heart.
To my parents, who supported me through thick and thin, and especially through a two-day drive to Belgium.
To Silvia, who somehow balances holding the fort down with her myriad responsibilities, and to Nano, we're all rooting for you now.
To Ed, you are my home anywhere we are.

Abstract

In today's environmental scenario, the pursuit of efficient, cost-effective, and environmentally sustainable strategies to harvest renewable energy is accelerating.
Solar cells are a promising solution for sustainable energy production, offering efficient photovoltaic energy conversion. Among these, perovskite solar cells have gathered significant attention due to their high efficiency and low-cost fabrication processes. However, the practical application and marketability of perovskite solar cells are limited by their lower performances compared to Silicon counterparts, and their instability over time.

One reason for these limitations is the mismatch in energy levels between the different layers of the structure of the perovskite solar cell. Electrons and holes have to pass through each layer and each different interface, and the ease with which this occurs, directly affects the collection efficiency of the carriers and the final power conversion efficiency of the device. Interface passivation can be employed to modify these interfaces and promote better energy alignment.

In this thesis, three interfaces of a medium-bandgap hybrid inverted perovskite solar cell are treated. Different quantities and deposition techniques of two self-assembled monolayers and two inorganic salts are studied. Emphasis is brought on the analysis of the performance and of the stability. The devices are furthermore characterized using different spectroscopy techniques, such as photoluminescence, to gather further insight into the behaviour of the passivated devices.

Contents

List of Figures

List of Tables

Symbols and abbreviations

Symbols

Ag Silver.

BCP Bathocuproine.

CH_3 Methyl group.

CIGS Copper indium gallium selenide.

C_{60} Carbon 60.

CdS Cadmium solfide.

CdTe Cadmium telluride.

CsBr Caesium bromide.

CsI Caesium iodide.

C Carbon.

FAI Formamidinium iodide.

$FAPbI_3$ Formamidinium lead iodide.

GaAs Gallium arsenide.

MACl Methylammonium chloride.

MAI Methylammonium iodide.

$MAPbI_3$ Methylammonium lead iodide.

Me – 4PACz [4-(3,6-Dimethyl-9H-carbazol-9-yl)butyl]phosphonic acid .

MeO – 2PACz (2-(3,6-Dimethoxy-9H-carbazol-9-yl)ethyl)phosphonic acid.

N_2 Nitrogen gas.

NiOx Nickel oxide.

PbI_2 Lead iodide.

Pb Lead.

Si Silicon.

TiO_2 Titanium dioxide.

LiF Lithium fluoride.

2PACz [2-(9H-carbazol-9-yl)ethyl]phosphonic acid.

C

CTL Charge transport layer.

CVD Chemical vapor deposition.

D

DSSC Dye-Sensitized solar cells.

E

EQE External quantum efficiency.

ETL Electron transport layer.

F

FF Fill factor.

FWHM Full width half maximum.

H

HTL Hole transport layer.

I

IPA Isopropanol.

IQE Internal quantum efficiency.

ITO Indium tin oxide.

P

PCE Power conversion efficiency.

PL Photoluminescence.

PSC Perovskite solar cell.

PV Photovoltaic.

PVD Physical vapor deposition.

S

SAM Self-assembled monolayer.

SEM Scanning electron microscopy.

SSPL Steady-state photoluminescence.

T

TCO Transparent conductive oxide.

TEAI Thiopheneethylammonium iodide.

TPC Transient photo-current.

TPV Transient photo-voltage.

TRPL Time-resolved photoluminescence.

U

UV Ultraviolet.

X

XRD X-ray diffraction.

Physical quantities

$\mathbf{I_0}$ Dark saturation current (A).

$\mathbf{I_L}$ Current generated by light (A).

$\mathbf{I_{sc}}$ Short-circuit current (mA).

$\mathbf{I}$ Photocurrent (A).

$\mathbf{J_{sc}}$ Short-circuit current density ($\mathrm{mA \cdot cm^{-2}}$).

$\mathbf{P_{MP}}$ Maximum power point (W).

$\mathbf{P_{in}}$ Input power (W).

$\mathbf{P}$ Power (W).

$\mathbf{T}$ Absolute temperature (K).

$\mathbf{V_{MP}}$ Maximum power voltage (V).

$\mathbf{V_{oc}}$ Open-circuit voltage (V).

$\mathbf{V}$ Voltage (V).

$\mathbf{k_B}$ Boltzmann's constant ($\mathrm{m^2 \cdot kg \cdot s^{-2} \cdot K^{-1}}$).

$\mathbf{n}$ Ideality factor.

$\mathbf{q}$ Electron charge (C).

$\mathbf{r_A}$ Ionic radius for the ion in the A site of ABX_3 (Å).

$\mathbf{r_B}$ Ionic radius for the ion in the B site of ABX_3 (Å).

$\mathbf{r_X}$ Ionic radius for the ion in the X site of ABX_3 (Å).

$\mathbf{t}$ Goldschmidt tolerance factor.

1 | Introduction

The world is dealing with a critical climate crisis, with threatening consequences, such as the widely acknowledged temperature increase. Rising carbon dioxide levels in the atmosphere, caused by the use of fossil fuels, are prompting efforts to transition away from conventional methods of energy production and toward renewable energy sources, such as tidal energy, wind energy, biomass energy, and solar energy. Among these, solar energy is the most abundant, due to the presence of the sun, which emits a large amount of energy due to fusion of hydrogen nuclei, in the form of solar radiations. Solar energy is available everywhere without any cost and it can be easily converted into electricity with solar photovoltaics (PV).

Solar PV is one of the most cost-effective technologies for electricity generation and its capacity is increasing, from around five gigawatts in 2005 to approximately 1.18 terawatts in 2022 [3]. It contributed in 2023 to 5.4% out of the total 30.2% share of renewable electricity (figure 1.1a) and in 2023 alone it accounted for three-quarters of renewable capacity additions worldwide [4].

Looking to the future, the global energy portfolio is transitioning more towards renewable energy, and it is projected to add more renewable capacity, within the next four years, than has been installed since the first commercial renewable energy power plant was built over a century ago [4]. Solar PV and wind will account for 95% of global renewable expansion, benefiting from technology improvement, complementary renewable energy policies, increased financing and dramatic cost reductions. The latter, can be illustrated from figure 1.1b for example, which shows the price experience curve for PV modules, i.e. the relationship between the cumulative shipments of a product and its average sales price over time, depicting how the cost of producing PV modules decreases as more of them are manufactured and sold [5] [1].

[1] In figure 1.1b, the last data point indicates the module shipment volume and average spot market price at the end of 2022.

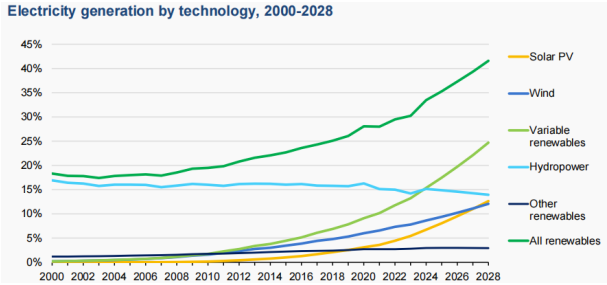

(a)

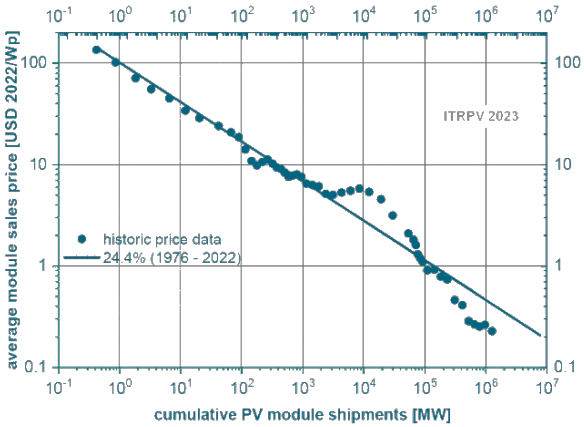

(b)

Figure 1.1: (a) Share of renewable electricity generation by technology (2000-2028), from [4], and (b) learning curve for module spot market price as a function of cumulative PV module shipments, reproduced with permission from [5].

The building blocks of PV systems include cells, modules, panels and arrays.
The photovoltaic **cell** converts solar radiation directly into current electricity. Solar cells are the building blocks for modules, which serve as the building blocks for panels and complete PV systems [6] (see figure 1.2).
From a commercial standpoint, solar cells are initially investigated at the laboratory level. Afterwards, attention shifts towards understanding their integration within modules and panels, which are commercialized and utilized in everyday applications.

The metric to compare solar cells is based on the **power conversion efficiency** (PCE), which is defined as the ratio of the output power to the input power given by the light.

Working principle and cause of losses in solar cells

The working principle of solar cells is based on the photoelectric effect, i.e. "the emission of electrons or other free carriers when light shines on a material" [7].

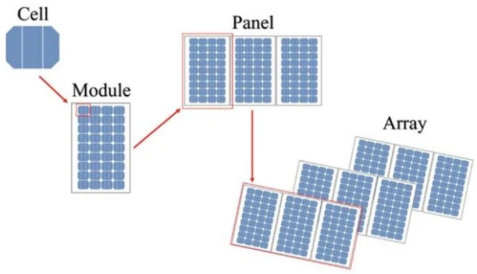

Figure 1.2: The basic building blocks for PV systems: cells, modules, and arrays, reproduced with permission from [6].

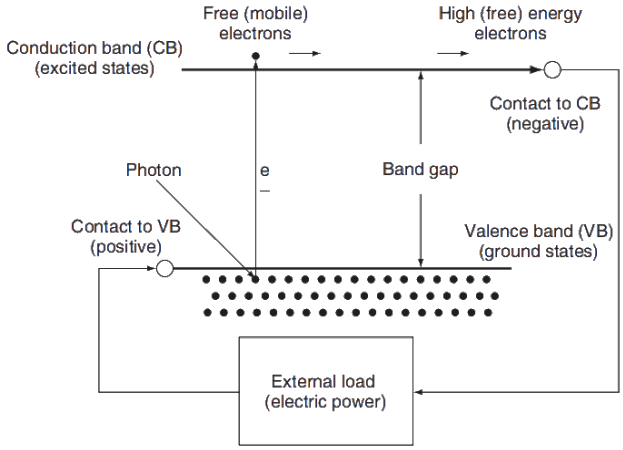

Figure 1.3: Schematic of a solar cell, reproduced with permission from [8].

On a general basis, solar cells are typically made of a semiconductor, able to absorb light, sandwiched between two selective contacts. When exposed to sunlight, if the incident photons have sufficient energy, i.e. exceeding the value of the band-gap, electrons in the valence band of the semiconductor material absorb the photons energy and move to the conduction band. There, a contact selective to the conduction band (an n-doped semiconductor), collects conduction-band electrons and drives them to the external circuit. The electrons lose their energy by doing work in the external circuit. Then, a second contact, selective to the valence band (a p-type semiconductor), returns them to the valence band with the same energy they started with, via the return loop of the circuit. The movement of electrons in the external circuit and contacts is the electric current [8]. This mechanism is shown in figure 1.3.

Sunlight is a spectrum of photons distributed over a range of energy (figure S1a). Undoubtedly, the energy of those photons and the band-gap of the material are strictly linked to the accomplishment of the photoelectric effect and consequently, to the efficiency of

the device. In fact, only photons with energy higher than the band-gap can be absorbed and contribute to the current formation. Additionally, the excess energy of those photons is lost in a thermalization process, where the excited electrons "relax to the conduction band edge" [9].

The dependency on the band-gap for absorption of photons and the thermatization process, are examples of intrinsic losses of PV devices. Further sources of intrinsic losses are discussed in detail in the literature [10, 11].

Intrinsic losses are unavoidable even in an ideal device, while *extrinsic* losses are theoretically avoidable [10]. Extrinsic losses include series resistance, parasitic recombination and contact shadowing, which are explained in detail in the literature [12].

In 1961, W.Shockley and H.Queisser [13] determined a power conversion efficiency limit for single-junction devices with specific band-gaps taking only fundamental loss processes into account [14]. The **Shockley-Queisser limit** is used as theoretical limit to quantify the performance of devices, and their proximity to ideality. It is shown in figure 1.4 for a solar cell operated at 298.15 K and illuminated with the AM 1.5G [2] spectral irradiance as a function of the band-gap energy and the band-gap wavelength.

Small discrepancies from the Shockley-Queisser limit can be found in the literature, due to a different standard sunlight spectrum, a different cell temperature or different numerical methods [18–24].

Photovoltaic cells generations

Advances related to materials and manufacturing methods have had a significant role behind the development of solar PV, resulting in their categorization into four generations based on their development stage, as shown in figure 1.5 [25]. Each class of PV devices displays distinct characteristics, progression and working principle. These distinctions have contributed to varying efficiencies achieved over time, based on the distinct Shockley-Queisser limits.

For simplicity, the focus will be mainly on solar cells, as they are the fundamental components of PV systems.

[2] "The AM1.5 standard spectrum, established by the American Society for Testing and Materials (ASTM) [15], serves as a uniform method for testing and certifying various solar cell types. The spectrum simulates solar distribution in the Earth's atmosphere after passing through 1.5 atmospheric thicknesses, covering wavelengths from 280 nm to 4000 nm and their corresponding intensities. And the AM1.5G spectrum encompasses the full range of solar radiation, including both direct and scattered radiation" [16].

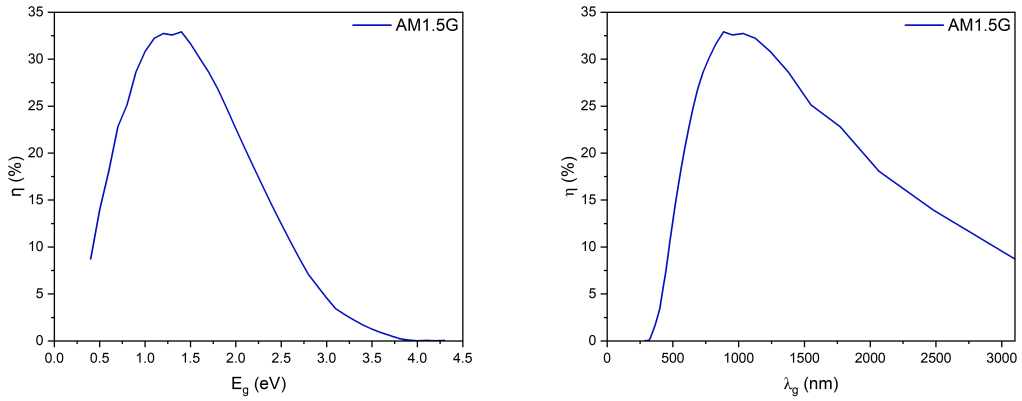

(a) (b)

Figure 1.4: Shockley-Queisser limit for a solar cell operated at 298.15 K and illuminated with the AM 1.5G spectral irradiance as a function of (a) the band- gap energy and (b) the band-gap wavelength. Plotted with the tabulated values of [17].

The **first generation** is based on mono-, poly-, multicrystalline silicon (Si), and single III-V junctions [3], such as gallium arsenide (GaAs).
Silicon based solar cells were the first to appear on the market, due to an already developed Si-based semiconductor production for microchips [27]. Today, crystalline silicon is the dominant PV technology, with a market share of more than 97% in 2023 [4]. This is due to their relatively high efficiencies, which increased from 6% when they were first introduced in 1954 [28], to 27.09% in 2023 [29, 30], and their high durability in time, close to 30 years [31].

The **second generation** is based on thin film photovoltaic cell technology of microcrystalline silicon, amorphous silicon, copper indium gallium selenide (CIGS) and cadmium telluride/cadmium sulfide (CdTe/CdS) photovoltaic cells. They were initially designed with the intent to reduce costs, and they showed improved mechanical properties ideal for flexible applications, but reduced efficiencies [25].
Thin-film technology contributed to about 5% of the total PV market in 2021 [32] and shows relatively high values of the efficiency compared to the first generation. In 2023, the highest efficiency recorded for CIGS solar cells was 23.64% [33, 34], 22.6% for CdTe devices [33], while for amorphous silicon devices, 14.0% [33, 35].

The **third generation** relies on nanomaterials and emerging technologies. They include organic molecules and polymers, quantum dots, dyes, perovskites, and modified structure

[3] "A III-V compound semiconductor is an alloy, containing elements from groups III and V in the periodic table" [26].

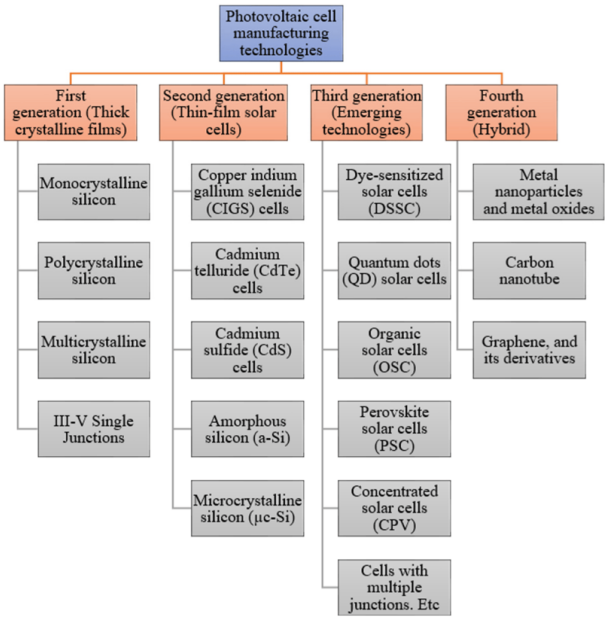

Figure 1.5: Photovoltaic cell generations, from [25].

of the previously developed devices.

Organic solar cells are based on conductive organic polymers or small organic molecules for light absorption and charge transport [36]. They are attractive due to their low cost and solution-processability of the molecules, but they are not widely produced commercially. This is in part due to their relatively low efficiencies, the highest of 19.2% in 2022 [37, 38].

Similar values are obtained for *quantum dot solar cells*, which established a 18.1% efficiency in 2023 [38, 39].

Dye-Sensitized solar cells (DSSC) rely on a highly porous, nanocrystalline layer of titanium dioxide (TiO_2) in contact with an electrolyte solution containing organic dyes that absorb light. They are promising due to their simple fabrication, low material costs, transparence, color capability, and mechanical flexibility [25], but lack in efficiency and stability. In fact, the highest efficiency recorded for DSSC is 13% ([37, 40]), clearly critical when compared to their second and first generations counterparts.

Multi-junction cells were conceived with the intention to overcome the Shockley-Queisser limit. They are based on a stack of different light absorbers with decreasing band gap energies, so that the highest-energy photons are absorbed by the material with the largest band-gap, and lower-energy photons pass through the layer to reach a smaller band-gap semiconductor, maximizing the number of photons used to convert sunlight in energy [9]. In this way, two connected ideal semiconductor junctions could reach an efficiency limit of 46% under the standard solar spectrum and intensity, while three junctions could

reach 52% efficiency and, theoretically, up to 68% efficiency, with infinite junctions [41]. The highest efficiency achieved has a value of 39.5% in 2022 for a four-junction solar cell [42, 43].

Perovskite solar cells employ perovskite materials as light absorbers. They present many advantages, and relatively high efficiencies, but only at the laboratory level, due to inefficiencies related to the exposure to the ambient. Further details and explanations follow in section 1.1.

The **fourth generation** is based on nanostructures such as metal nanoparticles and metal oxides, carbon nanotubes, graphene, and their derivatives. Graphene and its derivatives are a promising area of research and their advantages in PV applications include flexibility, environmental stability, low electrical resistivity, and photocatalytic features. Nonetheless, they are in the early stages of research and development [25].

Additional information on the fourth generation can be referenced in the existing literature [44].

Figure 1.6 shows the highest confirmed conversion efficiencies for research cells of different technologies, updated to March 2024, while figure S1b shows the obtained efficiencies compared to the relative Shockley Queisser limit, updated to December 2023.

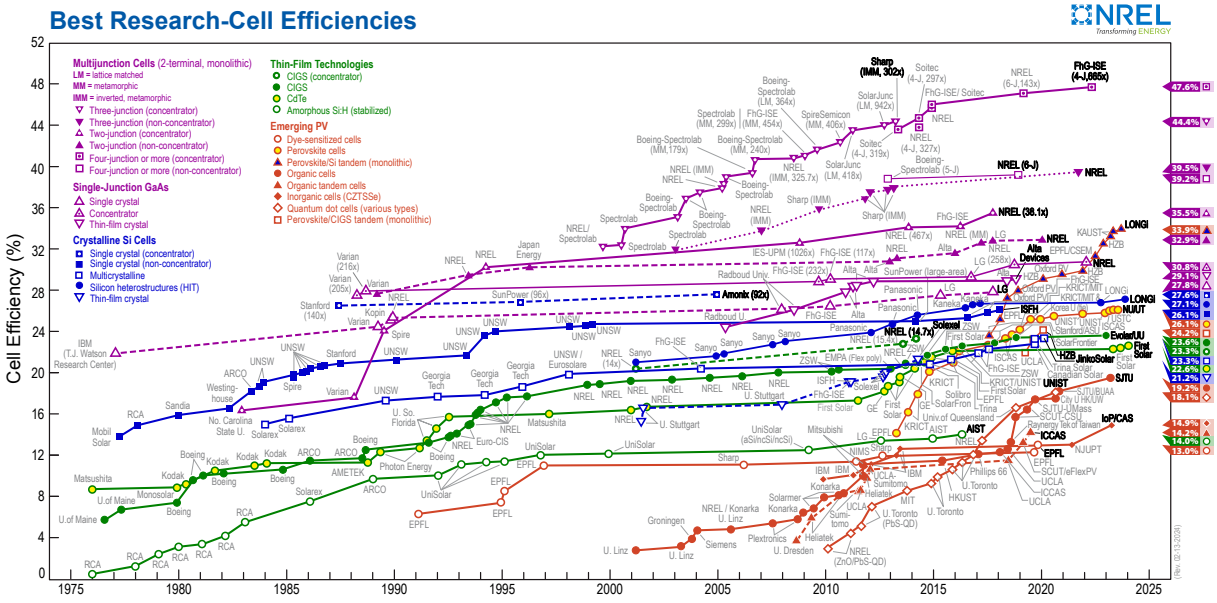

Figure 1.6: Best research-cell efficiency chart, from [45].

1.1. Perovskite solar cells

Perovskite solar cells (PSCs) are based on a perovskite material which acts as light absorber and charge carrier conductor.
They were first introduced by Tsutomu Miyasaka et al. in 2009 with an efficiency of 3.8% [46], and with a rapid development over the past fourteen years, they reached an efficiency of 26.1% for single-junction devices in 2023 [47]. This rapid improvement makes PSCs expected to be comparable to crystalline silicon devices in the future, surpassing other kinds of cells which suffered impediments in further improvement [48]. However, the limited values of durability of PSCs pose a challenge to their commercialization. To enter the market, they must comply with the stability criteria for thin-film photovoltaic cells, which allow a maximum 10% degradation in initial performance over 1000 hours, or for crystalline silicon solar cells, which allow only a 5% decrease in initial performance [49].
Additional issues are related to toxicity and scalability.

Perovskites

Perovskites are a broad class of materials with a general stoichiometric formula ABX_3, where A and M are cations, while X is an anion. They exhibit a crystal structure defined as a "network of corner-sharing BX_6 octahedra" [50], as shown in figure 1.7.

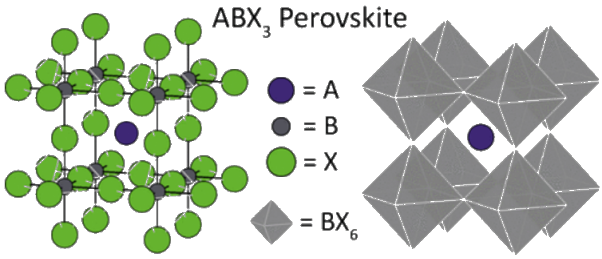

Figure 1.7: Perovskite crystal structure, showing all the atoms (left) or only the BX_6 octahedral network and A atoms (right), reproduced with permission from [50].

The amount of natural perovskite minerals is limited, while synthetic ones can exist in many complex formulas, such as metallic perovskites, hybrid organic-inorganic perovskites, metal-free perovskites, and noble gas-based perovskites, depending on their elemental compositions [50]. Practically, one can combine a selection of elements at the respective sites of the compound, satisfying the charge neutrality condition, making perovskites broadly researched optoelectronic materials.

Formability, geometric stability and distortion of crystal structures of perovskite materials in the ABX_3 form can be estimated with the *Goldschmidt tolerance factor*, defined as

$$t = \frac{(r_A + r_X)}{\sqrt{2}(r_B + r_X)} \tag{1.1}$$

where r_A, r_B and r_X are the ionic radii for the ion in the A, B and X sites, respectively [51]. A value between 0.8 and 1.0 indicates a cubic structure, while larger or smaller values of tolerance factor usually result in nonperovskite structures [52].
Further studies have determined that the Goldschmidt tolerance factor is not sufficient to predict the formation of the perovskite structure, but other parameters are needed. For a detailed analysis, consult the literature [53, 54].

In terms of photovoltaic applications, *halide perovskites* are mostly employed, and they are characterized by halides as their X anions.
Halide perovskites display many useful characteristics such as high light absorptivity, great charge-carrier mobility, long exciton diffusion length, low exciton binding energy and tunable band-gap [55].
Tuning the band-gap allows optical properties to be tailored for specific applications. In photovoltaics, it would mean broadening the light absorption, aiming to absorb all visible and some of the near-infrared light of the solar spectrum (as only an ideal light absorber would) [56]. The band-gap can be varied by replacing the cations A and M with other cations, or by changing the halide of the B-X bond.

Preparation methods of perovskite films

High performance and quality of the perovskite layer are closely correlated in PV devices, thus it is crucial to fabricate high quality films with controlled morphology, crystallinity and corresponding optoelectronic properties.
The development of perovskite film morphology during the crystallization significantly influences several key factors of the final perovskite layer such as the efficiency of charge dissociation, the dynamics of charge recombination, and diffusion lengths. The crystallization behavior is strongly influenced by various critical factors, including the surrounding environment, precursor composition, solvents, additives used and the deposition method employed [54].

The *surrounding environment* influences the perovskite layer during its formation. In fact, most perovskites are deposited and annealed in nitrogen (N_2) filled gloveboxes and the presence of moisture due to the hydrogen in air could deteriorate or improve film

properties [57]. The humidity has to be carefully controlled during the film formation.

The *precuror stoichiometric composition* and *solvents* affect film formation and quality as well. Solvents are especially crucial in solution-based methods, and the solubility of the precursors with the chosen solvent is of primary importance.

Additives can be included in the precursor solutions enhancing crystallinity, film coverage, and resulting device performance [54].

The *deposition methods* are different, and include solution processing, vapour deposition, and hybrid vapour-solution processing.
Solution processing entails low cost and ease of fabrication. The most widely used technique is spin-coating, which employs the centripetal force of a rotating sample. It can either be static or dynamic [58], where the former consists in releasing the solution on a still substrate, then put into rotation, while in the dynamic case the solution is released on a sample which is already rotating. During the rotation the excess solvent evaporates and the creation of the perovskite layer takes place [59].
It can either be carried out with one single solution being spin coated (one-step), or with the sequential spin coating of two different solutions, containing the precursors of the perovskite (two-step sequential deposition technique).
Both the viscosity of the fluid and the speed affect the thickness of the resulting layer.
After the spin coating, *quenching* may be employed, for crystal nucleation and growth [60]. Often a thermal treatment may be also applied after the spin coating to initiate or accelerate the reaction between the precursors. Thermal annealing consists in laying the samples on a hotplate at different temperatures and for different durations of time, based on the material and the purpose. The heat affects the atoms in the crystal lattice, leading to changes of the physical and sometimes also chemical properties.

Vapour deposition techniques are a broad group of techniques, which usually result in high-quality perovskite films but require the use of expensive vacuum facilities. As for the solution processing, it can be carried out in one step or in two-step sequential evaporations. They can either belong to the physical vapor deposition (PVD) or to the chemical evaporation deposition (CVD) one.
One the techniques employed to deposit thin films throughout this thesis is thermal evaporation, part of the physical vapor deposition (PVD) family. It relies on the condensation of vapors on the substrate surface the material to be deposited is evaporated from the source due to heating at high temperatures.
A more exhaustive discussion of vapour deposition techniques can be found in the literature [61].

Hybrid vapour-solution processes combine the previously discussed solution and vapour processes.

Structure of perovskite solar cells

The easiest structure of perovskite solar cells is based on a perovskite active layer sandwiched between charge transport layers (CTLs) and two electrodes. When the device is illuminated, the perovskite layer absorbs the light, so to generate photoexcited charges which are then transported to the relative CTLs. Charge transport layers, either electron transport layers (ETLs) or hole transport layers (HTLs), have the task of transporting selected photoexcited charges to the respective electrodes.

There are two main architectures of perovskite solar cells, as depicted in figure 1.8: mesoporous and planar (n-i-p and p-i-n). The mesoporous architecture is based on a mesoporous electron transport layer within which the perovskite self assembles [62]. The planar architecture instead, has compact charge transport layers and resembles the one of conventional silicon-based solar cells [63].
Based on the order of the layers, it can be either *regular* (n-i-p), which consists of glass/transparent conductive oxide (TCO)/ETL/perovskite/HTL/electrode, or *inverted* (p-i-n), i.e. glass/TCO/HTL/perovskite/ETL/electrode.

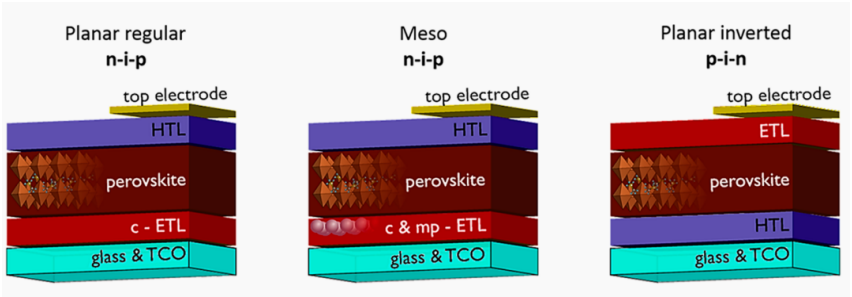

Figure 1.8: PSCs structures, adapted with permission from [64]. Copyright 2018 American Chemical Society.

Interface passivation

Despite the notorious increase of performances of PSCs over the past decade, there are still limiting factors to further increments of the efficiencies. In particular, one can look at the interfaces where several important physical processes occur.

In the first place, the perovskite layer interface is host to several surface and bulk defects, which hinder the device performance. Such defects include vacancies, interstitial defects,

lattice distortion by accumulated charges, and dissolved impurities [65, 66].
They can be attributed to the rapid crystallization due to wet chemical processes, which leads to the formation of various crystal defects. Additionally, the crystal bonds in these perovskites are predominantly of ionic bonding characters, with a small fraction of valence bonding characters [67, 68], which makes these crystals more sensitive to the environment (humidity, oxygen, temperature). Crystal defects can also grow after the perovskite layer has formed, during other steps of the device fabrication process, and during the operation [69].
The defects present in the perovskite layer, both inside the grains and at the grain surfaces, have significant negative implications on charge carrier transport and charge carrier extraction processes. They can capture photogenerated carriers, leading to nonradiative recombination losses. Additionally, they can reduce the lifetime of carriers and induce ion migration and diffusion. Carriers trapped by defects and migrating charged ions from the bulk phase to the surface and grain boundaries accumulate at interfaces, causing band bending, alterations in energy level arrangement, built-in electric field changes, and nonradiative recombination losses at the interface [70, 71].

The behavior of carriers within the device is heavily influenced by the perovskite itself, but also by the interfaces adjacent to it, namely the HTL/perovskite interface and the perovskite/ETL interface. The efficiency of flow of photogenerated carriers from the light-absorption layer to the n/p-type semiconductor relies on these interfaces.
Electrons and holes have to pass through several layers and encounter different interfaces. When energy levels at the interfaces match, electrons and holes can pass through smoothly. If that is not the case, imperfect interface energy band arrangement may be the cause of non-radiative recombinations of the interface [71].
Figure S2 illustrates potential scenarios of energy level alignment at metal/organic and organic/organic interfaces. In cases where vacuum level alignment does not take place, charge transfer or chemical/physical interactions may occur, leading to the formation of a dipole layer or band bending. Further details can be found in the literature [72].

To address these challenges, *interface passivation* or *engineering* techniques are employed. This involves treating the interface between different materials to minimize defects or imperfections at the boundary, or aligning the energy levels between different materials. This helps to reduce the loss of charge carriers, enhance the efficiency of charge transport, and improve overall device performance. Various methods can be utilized for interface passivation, including employing self-assembled monolayers (SAMs), alkali salts or organic salts [73].

Challenges for the commercialization of PSCs

In addition to the relatively low efficiencies, which may be enhanced through interface passivation, other challenges hinder the commercialization of PSCs. These include the long-term stability, toxicity and scalability.

Long-term stability

The durability of PSC in outdoor conditions is compromised due to degradation. This is due to several factors, which can be classified as extrinsic and intrinsic [74].
Extrinsic factors are related to the environment and include moisture, oxygen and ultraviolet (UV) light exposure. Oxygen oxidises the organic compound of the cell, while the moisture is present due to the hygroscopic [4] nature of amine salts [31].

Intrinsic factors are due to intrinsic instability of the bulk perovskite material and the interface between the perovskite and the charge transport layers. These issues include phase transitions of the perovskites, such as the irreversible shift of methylammonium lead iodide ($MAPbI_3$) from a tetragonal to cubic phase at 55°C, or the transition of formamidinium lead iodide ($FAPbI_3$) from the semiconducting α phase to the photoinactive δ phase in the ambient environment [76]. Further details on the intrinsic instability of perovskites can be found in the existing literature [76, 77].

The toxicity is attributed to the presence of lead (Pb) in the devices, which raises environmental concerns [78]. Appropriate encapsulation is crucial to prevent Pb leakage in the environment, ensuring the safety and commercial viability of these devices. [78].

Scalability

The term *scalability* refers to the shift from small-area solar cells, to large-area mini-modules ($<200\,cm^2$) and sub-modules ($200\text{-}800\,cm^2$), which serve as the basis for commercialized PV devices. The increase of area is inevitably followed by a loss in efficiency, due to higher series resistance, lower shunt resistance, non-uniform coating and the inactive area of bus bars and interconnections. For PSCs, the efficiency experiences a greater deterioration as the area increases, compared to other types of solar cells [79].

Further research has to be conducted on achieving uniform coating over large-area substrates, obtaining better control of film formation, developing procedures for fabricating and integrating perovskite modules, and comprehending the influence of device architecture on module interconnection performance, as well as the reliability and stability of

[4] Hygroscopic: absorbing or attracting moisture from the air [75].

module operation.

1.2. Thesis objective and organization

This thesis focuses on interface passivation of wide-bandgap hybrid inverted perovskite solar cells, aiming to enhance their efficiency and long-term stability.
Chapter 2 introduces the technical sides of the fabrication and characterization techniques employed. The subsequent chapters are dedicated to three investigated regions of the device:

- chapter 3 examines the passivation of the interface between the hole transport layer and perovskite, referred to as **bottom layer modifications** (see figure 1.9a);
- chapter 4 delves into passivation of the perovskite, referred to as **bulk modifications** (see figure 1.9b);
- chapter 5 examines the passivation of the interface between perovskite and electron transport layer, referred to as **top layer modifications** (see figure 1.9c).

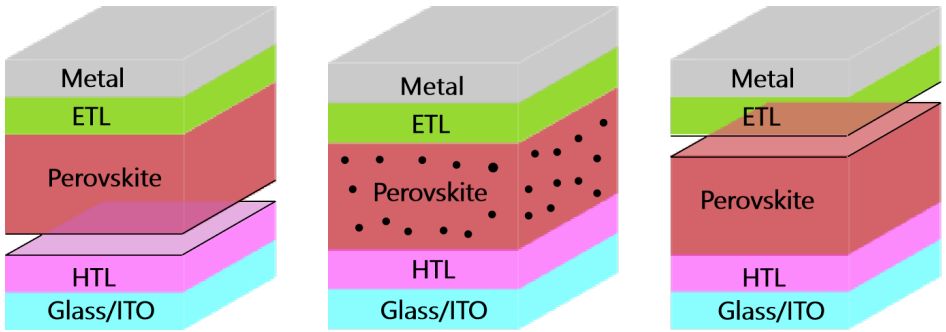

Figure 1.9: Schematic representation of: (a) "bottom layer modifications", (b) "bulk modifications" and (c) "top layer modifications".

2 | Fabrication and characterization

2.1. Fabrication

The fabrication work consisted in sequentially depositing the different layers of the stack of the inverted perovskite solar cell. It has been carried out completely in the laboratories at EnergyVille, Genk. The structure of the reference cell is described in the following section, alongside the different tools and techniques employed.

2.2. Reference cell

The reference cell is the base device for the modifications implemented in the thesis.

The different materials chosen for the reference cell are listed in table 2.1 and shown in figure S3a. A thorough table, including materials, thicknesses and deposition techniques, can be found in the appendix (table S1).

Components	Materials
Base substrate	Glass and indium tin oxide (ITO)
Hole transport layer	Nickel oxide (NiOx)
Perovskite	$FAPbI_3$
Electron transport layer	Lithium fluoride (LiF) Carbon 60 (C_{60}) Bathocuproine (BCP)
Metal	Silver (Ag)

Table 2.1: Different layers and materials of the reference cell.

The **base substrates** are 3x3 cm squares, 0.7cm thick.They are made of glass and have two ITO stripes, which are on one side on top of which the rest of the layers will be deposited.

Before depositing the HTL, the substrates have to be cleaned. This is done to allow the glass/ITO substrates to be properly ready for the depositions. It is carried out with an ultra-sonicator in a diluted cleaning agent, water, acetone and isopropanol (IPA) baths. An ultra-sonicator is a tool which employs sound energy to agitate particles in a liquid, which leads to a cleaning effect.

The **hole transport layer**, of NiOx, is deposited with linear sputtering, with a suited tool, in a high-vacuum chamber (base pressure $10^{-7} : 10^{-8}$ Torr). Linear sputtering is part of the PVD family, and it is based on condensation of vapors on the substrate surface and the material to be deposited is evaporated from the source due to ion bombardment [80]. In particular, DC sputtering was employed, where the power source is DC.
Afterwards it is annealed, on a hotplate at 300°C for 20 minutes. The thickness is 15 nm.

The **perovskite** used is FAPbI3 based [81] and it is composed of an organic and an inorganic part. The inorganic part is constituted by lead iodide (PbI_2), while the organic one is a solution of methylammonium iodide (MAI), formamidinium iodide (FAI), methylammonium chloride (MACl) and a solvent, ethanol.

The perovskite is deposited via a hybrid approach, i.e. a two-step vapor-solution sequential deposition. Initially a 200 nm-thick PbI_2 layer is thermally evaporated on top of the previously deposited HTL, and then $100\mu L$ of an organic solution is dynamically spin coated on top for 35 seconds at 3000rpm. To conclude, the sample is annealed in air at 130°C for 15 minutes. This last step is used to complete the crystallization of the perovskite film.

The organic solution can be prepared in different concentrations: different thicknesses of the PbI_2 layer, require different concentrations.
In the reference cell, for a 200 nm thick layer of PbI_2, the optimal concentration of the organic solution for a complete conversion of the PbI_2 into perovskite, is 0.43M.

The **electron transport layer**, composed by 0.8 nm of LiF, 30 nm of C_{60} and 5 nm of BCP, is deposited in one unique step via thermal evaporation. This is carried out with a suited tool, in a high-vacuum chamber (base pressure $10^{-7} : 10^{-8}$ Torr).
Despite being collectively labeled as ETL, it is essential to point out that C_{60} is the primary material serving this function. LiF is introduced for passivation [82] and BCP acts as a buffer layer between the metal and C_{60} [83].

The **metal** is deposited via thermal evaporation. sks (figure 2.1a) are used during the deposition, in order to define the active area of the twelve cells and the electrodes contacting the bottom ITO. In figure 2.1b it is possible to see the final sample, where the internal twelve rectangles correspond to the cells, while the upper and lower rectangles are used to contact the bottom part of the cells.

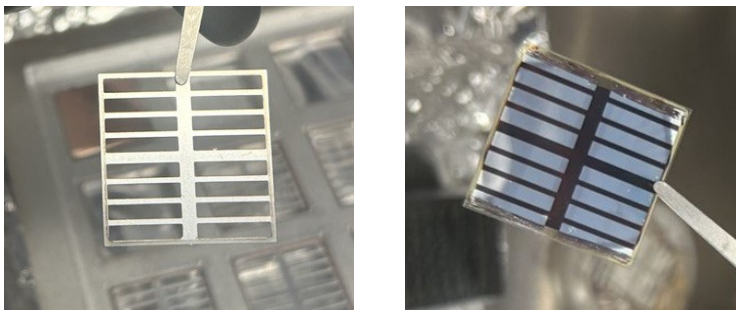

(a) (b)

Figure 2.1: (a) Mask used for the metal thermal evaporation and (b) the finished sample.

2.3. Characterizations and tests

2.3.1. Solar simulator

The solar simulator is a tool used to simulate 1-Sun illumination with light intensities according to the AM1.5 spectrum. It applies different voltages across the cell to obtain the current versus voltage curve (I-V); important parameters such as efficiency, short-circuit current (I_{sc}), open-circuit voltage (V_{oc}) and fill factor (FF) are obtained from the I-V curve.

Electrical parameters

The I-V curve of a solar cell is the result of the superposition of the dark IV curve of the solar cell diode with the current generated by light. The diode law reads:

$$I = I_0[exp(\frac{qV}{nk_BT}) - 1] - I_L \tag{2.1}$$

where I_0 is the dark saturation current, V is the applied voltage, q is the absolute value of electron charge, k_B is the Boltzmann's constant, T is the absolute temperature (in Kelvin), n is an ideality factor and I_L is the current generated by light. The curve is in the fourth quadrant, but it is flipped by convention, as in figure 2.2. From the crossing of the curve with the x and y axes, two important parameters are defined: the **short circuit current**, I_{sc}, i.e. the current when the voltage is null, and the **open circuit voltage**, V_{oc}, the voltage when the current is null. For an ideal cell, the short circuit current and the current generated by light coincide, thus I_{sc} represents the highest value of current achievable from the solar cell. In the same way, the open circuit voltage is the highest achievable voltage in the device.

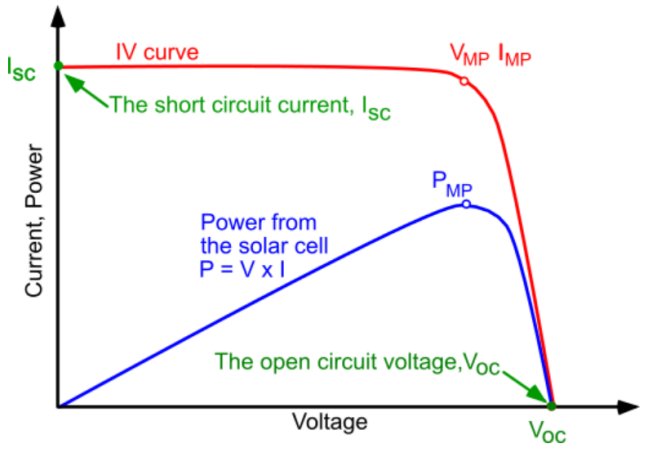

Figure 2.2: I-V curve and P-V curve of a solar cell, from [84].

In picture 2.2, other than the curve of the current, also the power is shown. It is given by the product of the voltage and the current:

$$P = V \cdot I \tag{2.2}$$

On this curve, it is possible to identify the maximum power point, P_{MP}, and as a consequence, on the I-V curve, the maximum power voltage, V_{MP} and the maximum power current, I_{MP}.
The maximum power is needed to identify the **fill factor**, FF:

$$FF = \frac{P_{MP}}{V_{oc} \cdot I_{sc}} \tag{2.3}$$

which represents the biggest area of the rectangle that can fit under the I-V curve and is a measure of the quality of the solar cell.

The power conversion efficiency is defined as the ratio of the output power to the input power given by the light, and can be expressed in terms of the V_{oc} , the I_{sc} and the FF, as follows:

$$\eta = \frac{P_{out}}{P_{in}} = \frac{V_{oc} \cdot I_{sc} \cdot FF}{P_{in}} \tag{2.4}$$

where P_{in} is the input power.

2.3.2. Thermal stability test

Concerning *stability*, when the PSC is outdoor, it experiences exposure to various stressors, including heat, light, humidity, and oxygen, leading to a gradual degradation of the cell

over time. To investigate these factors, accelerated ageing protocols are implemented to simulate the effect of years of outdoor operation within a condensed timeframe of weeks or months. During these tests, PSCs are exposed to higher levels of at least one of the stressors they would be exposed to during normal outdoor operation.
Several tests can be carried out in a laboratory, controlling the stress conditions, such as air, humidity, temperature, or another stressor of interest [85].

In this work a *thermal* stability test was performed. It involved leaving the samples on a hot-plate at 85°C for 1000 hours. It was carried out in the dark, in an N_2 filled glovebox. The samples were periodically monitored during the 41-day period, to evaluate the decrease of performance over time.

The samples subjected to the thermal stability test presented a different solar cell layer stack. In particular, a 70 nm-thick ITO layer is sputtered between the electron transport layer and the metal, to avoid metal diffusion to the lower layers, due to the high temperature. The ITO is deposited with the help of a mask. The metal is then deposited with a different mask than the one described for the reference cell (figure 2.1a), with smaller areas, to deposit silver only outside of the actual active area of the cells, once again to avoid any potential metal diffusion. The final sample is shown in figure 2.3b.
Table S2 lists the layers, materials and deposition techniques used in the reference cell modified for the thermal stability test.

Due to the presence of the more resistive ITO, the performance of the cells is much lower with respect to those cells having silver as the top electrode.

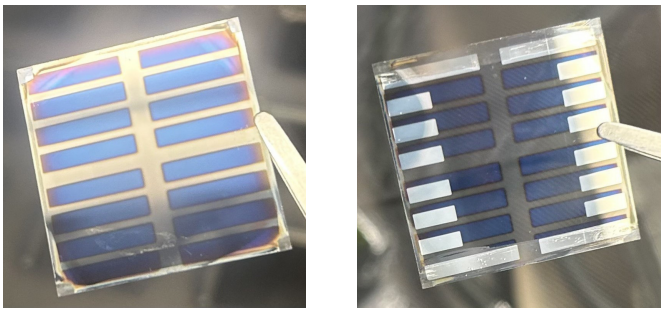

(a) (b)

Figure 2.3: (a) Layer of ITO on top of the ETL (before deposition of the metal) and (b) finished sample for the thermal stability test.

2.3.3. External Quantum Efficiency

The quantum efficiency is defined as the ratio of the carriers collected by the solar cell to the number of incident photons with a distinct energy.
It is divided in external quantum efficiency (EQE) and internal quantum efficiency (IQE). EQE is the ratio of number of charge carriers collected by the solar cell to the number of incident photons, while IQE only takes into account the absorbed photons [86]. This is the reason why the value of IQE is always higher than EQE.

Ideally, if all photons of the range of wavelengths considered were absorbed and the resulting minority carriers collected, then the quantum efficiency would be a square curve constant at 1, dropping solely for photons with energy below the band gap. This does not happen in reality, due to recombination effects.

The EQE can also be used to obtain a current density by integrating the EQE values with the AM1.5G spectrum, and it should be approximately equal to the short-circuit current density J_{sc}, given by I_{sc} divided by the area, measured in the J-V sweep:

$$J_{sc}(\lambda) = q \int_{\lambda_1}^{\lambda_2} EQE(\lambda) \cdot \Phi_{ph}^{AM1.5}(\lambda)\, d\lambda \tag{2.5}$$

where λ_1 and λ_2 are the initial and final wavelengths, and $\Phi_{ph}^{AM1.5}$ is photon flux corresponding to the AM1.5 spectrum.

2.3.4. Photoluminescence spectroscopy

Photoluminescence spectroscopy, or PL, is a characterization technique which exploits a photon flux. Light is directed onto a sample, causing photoexcitation and the subsequent release of photons as carriers return to the relaxed state. This occurs when the impinging photons have an energy greater than the band gap energy, thus the energy of the emitted photon is directly related to the band gap energy.
The information obtained with PL spectroscopy is related to material imperfections and impurities [87].

A schematic version of a classical PL setup is shown in figure 2.4.

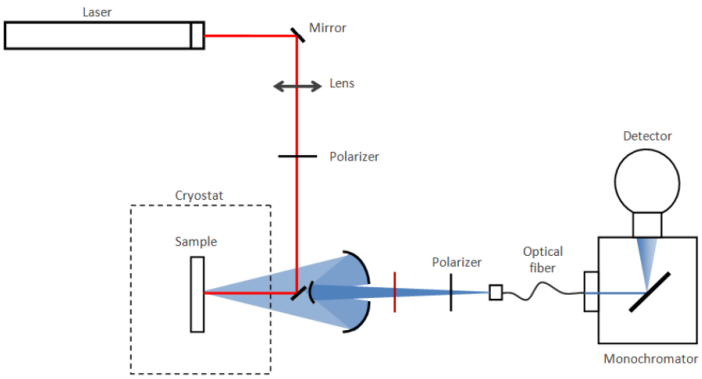

Figure 2.4: Classical PL setup, from [88].

There are two approaches to measure PL: steady-state and time-resolved. In the steady-state case, the sample is continuously illuminated with a constant light source and it mainly provides information on the band gap. In the time-resolved case instead, the sample is pulsed with a short, intense light source, and the emitted photoluminescence is monitored over time.

The **time-resolved photoluminescence** (TRPL) can provide information on charge-carrier processes in PSCs, including charge separation, trapping, and surface and bulk recombination. To obtain insight into these phenomena, different calculations can be made with the TRPL spectra.
A first analysis could be fit the TRPL curve with the continuity equation [89]:

$$\frac{dn}{dt} = G - k_1 n - k_2 n^2 - k_3 n^3 = G - n R_t(n) \tag{2.6}$$

where n is the charge carrier density, G stands for the charge-density generation rate, k_1 is first order charge-recombination rate, k_2 the second order recombination rate, k_3 the third order recombination rate and $R_t(n)$ is the total charge recombination rate:

$$R_t = k_1 + nk_2 + n^2 k_3 \tag{2.7}$$

The first-order recombination rate represents the processes involving only one particle (such as conduction-band electron, valence-band hole, or an exciton); the second-order recombination rate describes those processes involving two particles and k_3 those processes involving three particles, i.e. Auger recombination.
Due to lack of data of the tool, this method cannot be implemented.

A second less precise way to interpret TRPL results [90], is to fit the experimental results

with a bi-exponential function, such as

$$I(t) = A_1 exp(\frac{-t}{\tau_1}) + A_2 exp(\frac{-t}{\tau_2}) \tag{2.8}$$

where τ_1 is the fast decay lifetime and τ_2 is the slow decay lifetime. The fast decay lifetime is related to the charge trapping process at the perovskite surface, while τ_2 is related to the recombination process in the bulk [91].

The **steady-state photoluminescence** (SSPL) provides information on the band gap. In SSPL plots, a peak is observed due to the emission of photons by excited semiconductor materials. The peak corresponds to a wavelength which is related to the bandgap of the material, due to a relationship which allows to calculate the band gap from the peak wavelength:

$$E_g = \frac{h \cdot c}{\lambda} \tag{2.9}$$

where h is Planck's constant, c is the speed of light and λ is the wavelength.
The peak is around 800 nm, and the product $h \cdot c$ is ∼1240 nm, thus the band gap of the utilized perovskite is ∼1.55 eV.

2.3.5. Scanning electron microscopy

Scanning electron microscopy (SEM) is an imaging technique based on a focused beam of electrons impacting on a sample surface [92]. When this happens, the electrons interact with the atoms of the surface producing different electrons detected by detectors. These signals can be used to gather insights into the topography and composition of the surface. The detectors are based on the type of electrons collected: secondary and back-scattered. The latter derive from deeper regions of the sample, while the first originate from surface regions, therefore they carry different types of information.

A schematic version of a classical SEM setup is shown in figure 2.5.

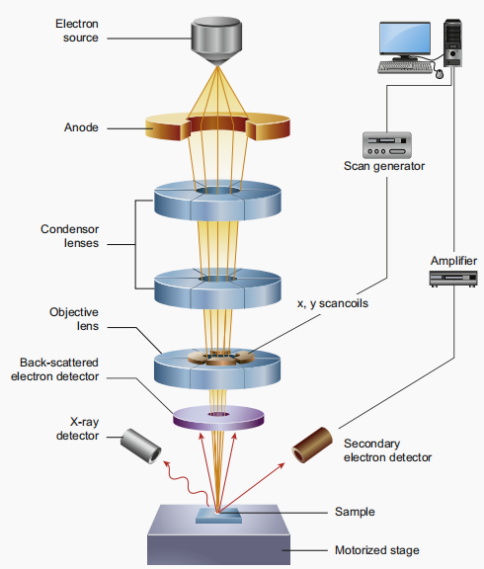

Figure 2.5: Classical SEM setup, reproduced with permission from [93].

2.3.6. Transient photocurrent and photovoltage

The transient photocurrent (TPC) and transient photovoltage (TPV) techniques are based on a perturbation by a modulated light on the device, and they give information on properties such as the charge carrier lifetime [94].

For TPV, the solar cell is kept at open-circuit conditions and it is connected to an oscilloscope (figure 2.6a), while in the TPC, it is kept at short-circuit conditions and it is connected to a small resistor (figure 2.6b).

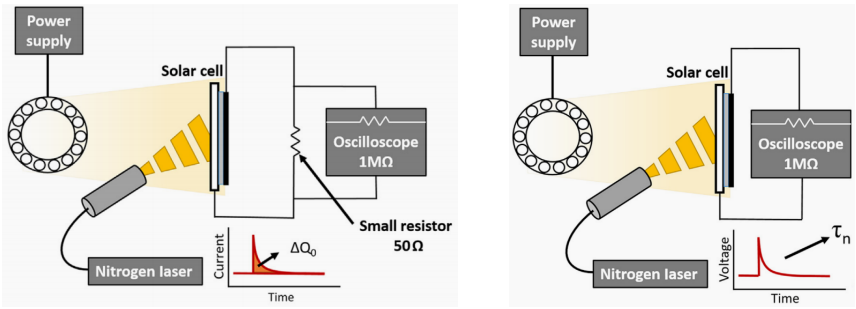

(a) (b)

Figure 2.6: (a) Set-up for the TPC technique and (b) set-up for the TPV technique, both reproduced with permission from [94].

For the TPV, the cell is initially exposed to a continuous light source, promoting a constant V_{oc}. Once the V_{oc} is stable, the solar cell is excited with an additional short-lived laser

pulse that generates a small perturbation of the V_{oc}. The change in V_{oc} is proportional to the photo-generated carriers by the laser pulse.
In the TPC instead, a perturbation of the current is generated, via a laser pulse. The resulting transient current is measured and integrated over time to calculate the amount of photo-generated charges induced by the pulse.

2.3.7. X-ray diffraction

X-ray diffraction analysis (XRD) is a technique used to identify the crystal structures present in a sample, evaluate the orientation of crystals and the average size of crystal grains in micro/poly-crystalline materials.
It is based on the diffraction of X-ray radiation: the sample is irradiated by a monochromatic X-ray radiation, the radiation is diffracted by the crystals in the sample and the intensity of the diffracted radiation is analyzed at different detection angles.

The XRD spectrum shows the intensity of the X-ray radiation detected as a function of the detection angle.

A schematic version of a classical XRD setup is shown in figure 2.7.

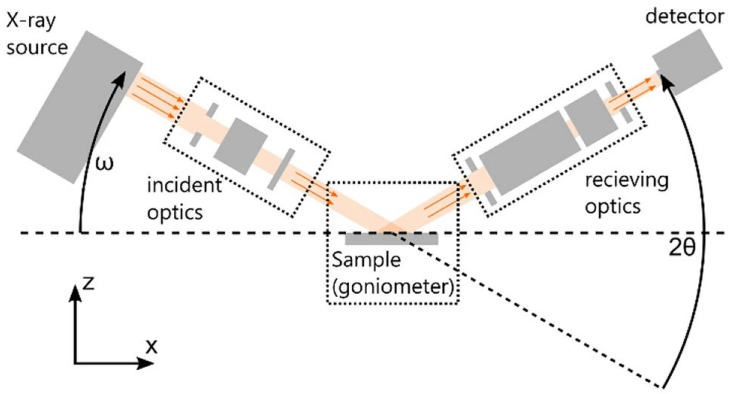

Figure 2.7: Classical XRD setup, reproduced with permission from [95].

3 | Bottom layer modifications

This chapter is dedicated to the "bottom layer modifications", i.e. at the interface between hole transport layer and perovskite. The approach is based on the use of self-assembled monolayers, following different ideas and concepts.

3.1. Self-assembled monolayers in perovskite solar cells

To help mitigate the issues related to losses at the interfaces (see section 1.1), one of the approaches implemented, especially in the latest years, is the use of self-assembled monolayers.

SAMs are, as defined by Ali et al [96], "ordered arrays of organic molecules formed by the spontaneous absorption onto a surface of molecular constituents from a vapor or liquid phase."
Their peculiarities include their growth, which is based on solution-phase transport of adsorbate molecules to the solid-liquid interface, adsorption on the substrate and two-dimensional molecular organization [97] and their structure, (figure 3.1), which includes an "ancoring group", which chemically attaches to the surface atoms. The variety of SAM molecules and consequently of head groups, leads to an incredibly broad use of SAMs for different applications.

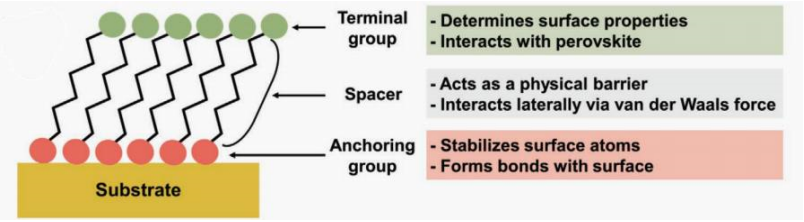

Figure 3.1: Structure of a SAM, adapted with permission from [98]. Copyright 2020 Advanced Energy Materials.

Historically, they have been used in light emitting diodes [99], field-effect transistors [100] and lately in photovoltaics. In relation to perovskite solar cells, they have the great asset of having a fabrication compatible with that of PSCs, which makes it easy to integrate them in the PSCs' structure.

In the past years SAM molecules have been implemented, either at the perovskite interfaces or in the perovskite itself, to obtain several positive effects and as a consequence, improve the overall performance of the cell [96, 98].
Some of these effects may include:

- influencing the morphology and increasing crystal quality of the perovskite layer, as noticed by Li et al [101], who connected the better cristallinity of the perovskite layer to the modifcation of the ETL with a self-assembled monolayer, and by other groups [102–104];

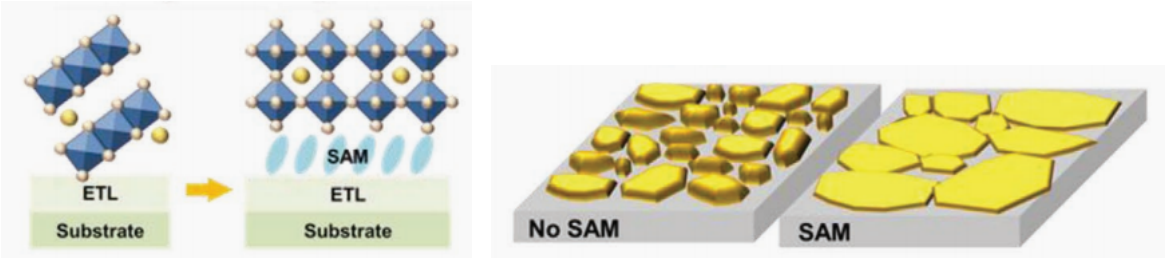

(a) (b)

Figure 3.2: Effect of SAMs in PSCs: (a) on crystallinity and (b) on grain size, adapted with permission from [98]. Copyright 2020 Advanced Energy Materials.

- deactivating surface dangling bonds to reduce charge traps at the interfaces between layers, as described by Wang et al. [105], who noticed a decrease in trap-assisted recombination, or by Yang et al. [106], who studied exciton lifetimes related to passivation of defects in perovskite films (with SAM-modified layers);

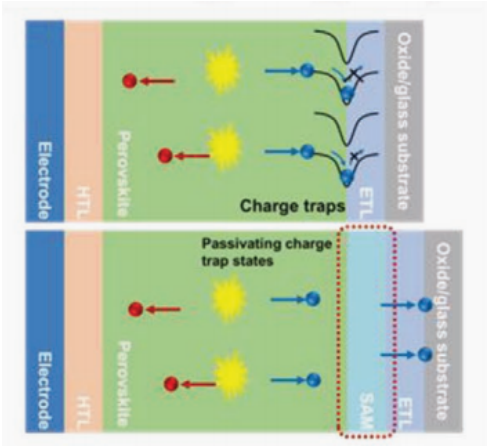

Figure 3.3: Effect of SAMs in PSCs: charge traps, adapted with permission from [98]. Copyright 2020 Advanced Energy Materials.

- affecting the interfacial dipole moment leading to a change in workfunction of the surface, which controls the energy barrier at the interfaces, and in turn the flow of carriers [106, 107];

- increasing the charge transfer from the perovskite layer to the next one, as determined by Azmi et al [108] and Bai et al [109], who studied the "quenching" (decrease) in photoluminescence, strictly related to an increase in charge transfer, with modification of charge transfer layers with SAMs;
- increasing the long-term stability of the cells, affecting the moisture resistance of the perovskite layer [110];
- reducing or eliminating the hysteresis [111, 112].

SAMs can be incorporated into the PSCs structure in different fashions. A recent one is the use of a SAM layer *in place of* the charge transport layer. In the case of n-i-p PSCs, one of the first cases was the one by Topolovsek et al in 2017 [113], who used self-assembled siloxane-functionalized fullerene molecules, eliminating the use of TiO_2 (which was the reasond behind a few disadvantages, such as the need of high temperature sintering). For HTLs in inverted PSCs, the first example was in 2018 with Magomedov et al [114], who used a new hole transporting material (V1036) on ITO. SAMs replacing charge transport layers have proved successful so far, and additonally, they reduce material consumption and cost [115].

A few cases regard the use of SAMs directly into the perovskite, as done by Zheng et al [2], who incorporated SAM molecules into the perovskite precursor solution in order to obtain the HTL and the perovskite layer in one step.

SAMs can otherwise be implemented as passivation layers, mostly in relation to the perovskite adjacent interfaces, which are critical for the performance of the cell. It may help in terms of energy band alignment, benefiting the compatibility between the charge transport layer and the perovskite.
In the case of n-i-p PSCs this has been carried out in several occasions, as in the already quoted Li et al [101] or [102–104, 106, 108, 111], while for inverted PSCs, a couple of different examples, who in particular use NiOx as hole transport layer, are Alghamdi et al [1], or Mann et al [116].

This chapter is dedicated to the use of one type of SAM on top of sputtered NiOx, following different deposition protocols, to try to improve the performance of the solar cell.

3.1.1. Implementation of SAMs on top of the NiOx

Common techniques for deposition of SAMs into PSCs are based on both vapor-phase and liquid-phase applications.

In this section, the spin coating method has been applied. Different cases have been studied: different concentrations of the applied SAM solution, adding steps after the spin coating to improve the deposition step, and optimizing the perovskite's organic solution concentration after the incorporation of a SAM layer.

Me-4PACz

The type of SAM implemented is [4-(3,6-Dimethyl-9H-carbazol-9-yl)butyl]phosphonic acid and is commonly called **Me-4PACz**.

It is based on 4PACz, a carbazole[1] based self-assembly monolayer, with one alkyl chain[2] and four carbon (C) atoms. Me-4PACz, in figure 3.4a, differs from 4PACz, shown in figure 3.4b, for the methyl group (CH_3) attached to the carbazole molecule.

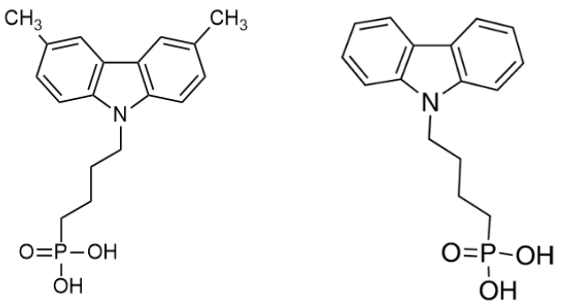

(a) (b)

Figure 3.4: (a) Me-4Pacz structure, from [119] and (b) 4PACz structure, from [120].

Rinsing

As anticipated, a key component of SAM growth is the 2D molecular organization. During the growth of a SAM, there may be an *excess* of unbound molecules, which may turn out to damage the performance of the cell [121]. To remove them, a *rinsing* process can be used. It consists in spin coating solvent on the sample. The solvent will evaporate, thus it has no impact on the stack of the cell (it does not constitute an additional layer), but it helps removing excess molecules.

3.2. Electrical results

[1] "Carbazole is an aromatic heterocyclic organic compound. It has a tricyclic structure, consisting of two six-membered benzene rings fused on either side of a five-membered nitrogen-containing ring" [117].
[2] "An alkyl group is an alkane missing one hydrogen" [118].

3.2.1. Optimal sequence of steps

The first investigation was on the appropriate sequence of steps to deposit Me-4PACz on nickel oxide (the HTL). In fact, based on the literature, there are different approaches on the order of annealing and rinsing, or on the eventual need of both. For example, Cassella et al [121] do a "postrinse", i.e. rinsing after annealing, while Alghamdi et al [1], only anneal after spin coating.

Four types of cells were compared: the reference, as described in section 2.2, only annealing (red in figure 3.5), annealing and rinsing (blue) and only rinsing (green).

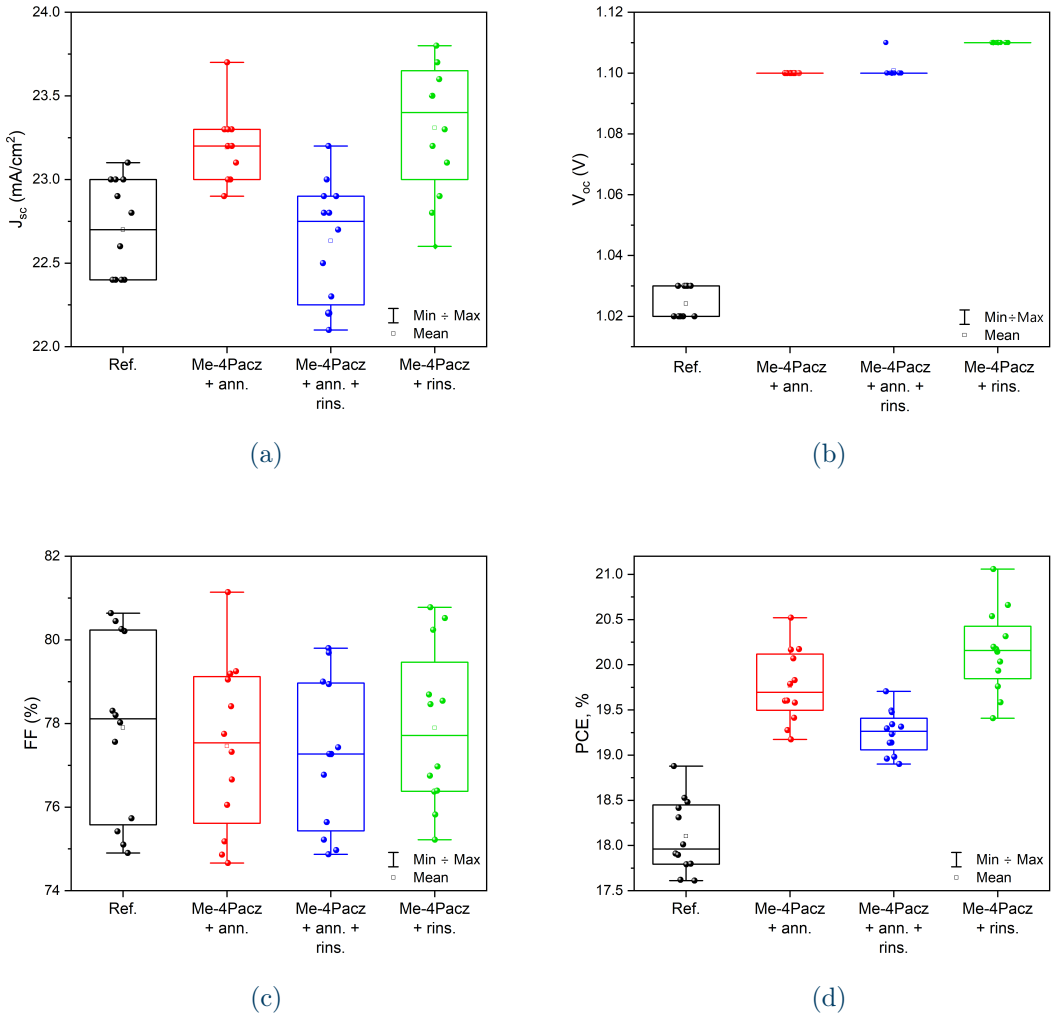

Figure 3.5: Statistics on (a) J_{sc} , (b) V_{oc} , (c) FF, (d) PCE of cells: reference, Me-4PACz on top of NiOx (different combinations of annealing and rinsing).

For this first type of test, a *standard* concentration of $0.33\,\mathrm{mg\,mL^{-1}}$ for the Me-4PACz

was used. It was spin coated at 3000 rpm for 30 seconds (similarly to the organic part of the perovskite which is spin coated at the same speed but for 35 seconds). The annealing was at 100 °C for 10 minutes inside the glovebox and the rinsing was both static and dynamic, one after the other, of $100\mu m$ of ethanol (the same solvent used for the Me-4PACz solution).

From the results in figure 3.5, it is quite clear how the best combination of steps is to only rinse after spin coating.
It is relevant to note the great boost of V_{oc} with Me-4PACz compared to the reference cell in figure 3.5b. Increasing the V_{oc} in fact, is not an easy task, due to the already obtained values close to the theoretical Shockley-Queisser limit [17].

3.2.2. Optimal concentration of Me-4PACz

In the first test, a standard concentration of Me-4PACz of $0.33\,\mathrm{mg\,mL^{-1}}$ was used, based on previous experiences of the group in Energy Ville. To be more thorough, in a second test, different concentrations of the SAM solution were analyzed.

In particular *higher* values were used, to inspect whether the rinsing step was no longer effective when more SAM solution is spin coated on the NiOx layer.

In figure 3.6 the comparison of a reference cell, and cells with increasing concentrations of Me-4PACz on top of NiOx is shown. The concentrations of the Me-4PACz solution are $0.33\,\mathrm{mg\,mL^{-1}}$ (as in figure 3.5), $0.7\,\mathrm{mg\,mL^{-1}}$ and $1\,\mathrm{mg\,mL^{-1}}$. (As in the previous paragraph the SAM was spin coated at 3000 rpm for 30 seconds, and afterwards annealed at 100 °C for 10 minutes).

From the results, the helping effect of Me-4PACz once again catches the eyes, in particular for the V_{oc}. Concerning instead the concentration of the SAM, the differences are not as relevant, but a too high amount of it seems to hinder the performance. From these results, we assumed $0.33\,\mathrm{mg\,mL^{-1}}$ to be a good compromise.

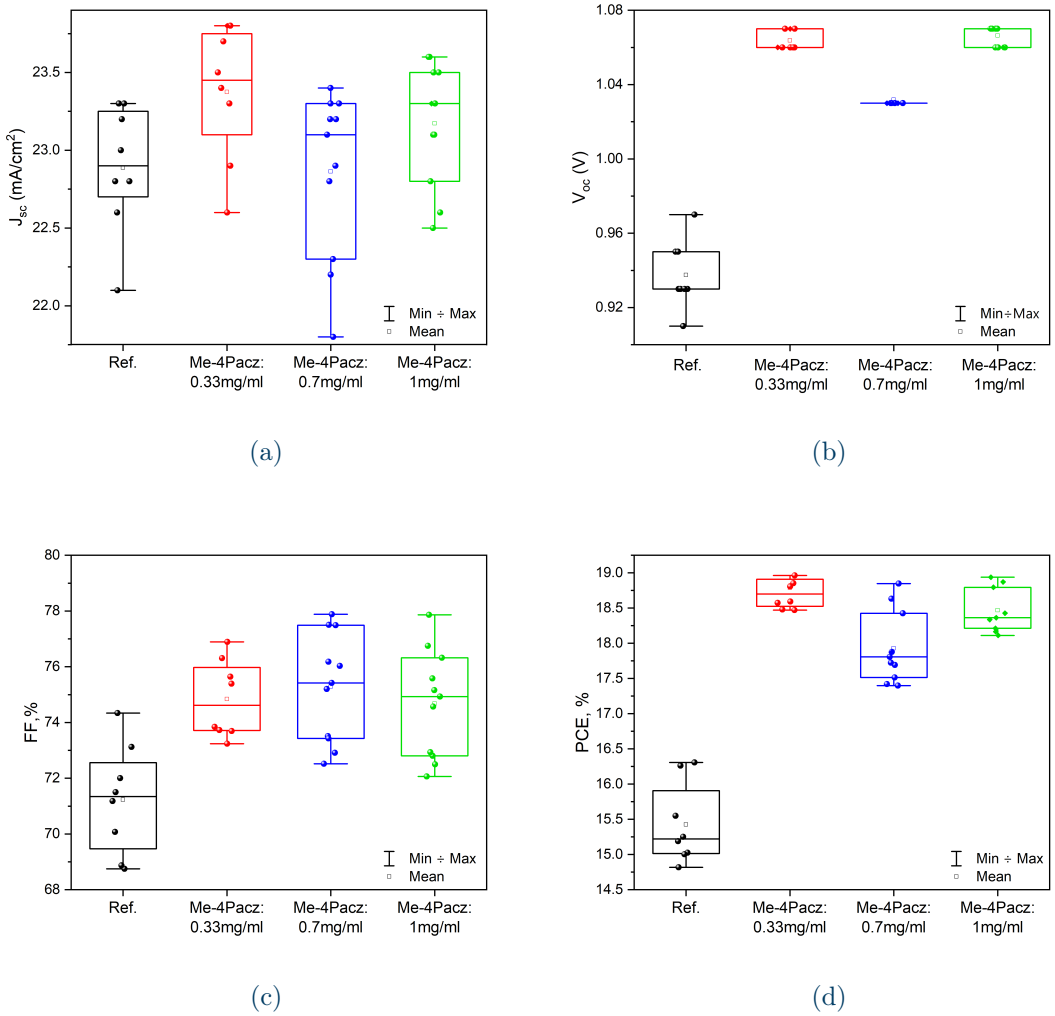

Figure 3.6: Statistics on (a) J_{sc} , (b) V_{oc} , (c) FF, (d) PCE of cells: reference and different concentrations of Me-4PACz solution.

3.2.3. Optimal concentration of perovskite

Once the optimal amount of Me-4PACz and the correct sequence of steps is established, one could wonder whether there are any other factors to manipulate to boost the performance. In particular, the concentration of the organic solution of the perovskite could have an impact. In fact, modifying the NiOx-perovskite interface with the SAM, a slight change in the perovskite layer itself could benefit the performance.

A third test was performed with different concentrations of the organic solution of the perovskite: since the reference is 0.43M, a sample with a lower one (0.41M) and a higher one (0.45M) were fabricated.

In figure 3.7, the samples called "Me-4PACz + 0.41M/0.43M/0.45M" refer to devices with Me-4PACz on top of NiOx with a 0.41M/0.43M/0.45M concentration of the organic solution of the perovskite.

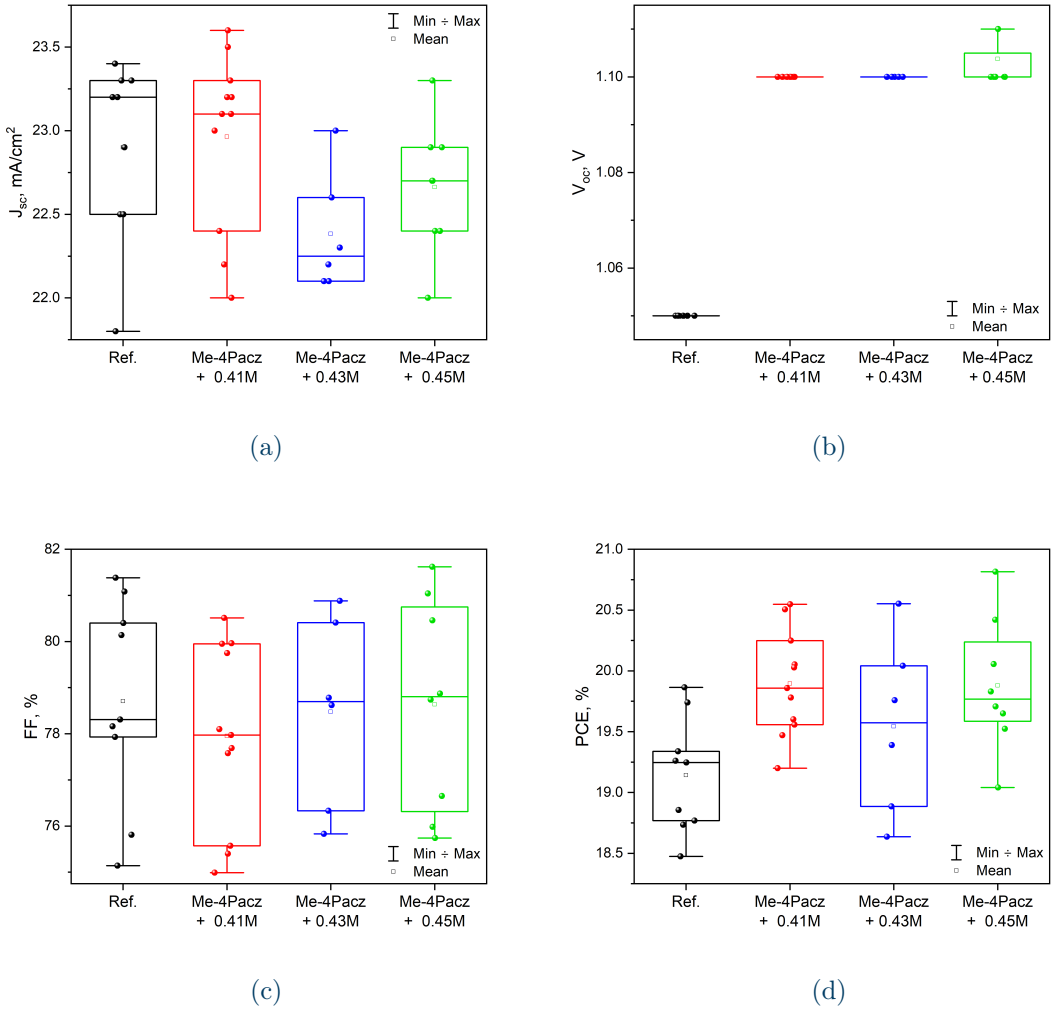

Figure 3.7: Statistics on (a) J_{sc} , (b) V_{oc} , (c) FF, (d) PCE of cells: reference, Me-4PACz and different concentrations of the organic solution of the perovskite.

From the results in figure 3.7, it is possible to see a slight difference when changing the concentration. In particular, while the V_{oc} is almost unaffected by the change in concentration, the FF increases with increasing concentration. The combination of higher V_{oc} and higher FF for 0.45M, are probably the reason behind the higher efficiencies for this concentration. Lower concentrations (0.41M) instead, seem to hinder the performance.

If the concentration is increased even more, up to 0.47M, a reduction of the performance

is observed (figure S4).

In conclusion, the passivation of the NiOx interface with Me-4PACz significantly enhances the performance of the solar cell. The observed improvement in V_{oc}, and consequently in PCE, can likely be attributed to the facilitated transport of charge carriers between the HTL and perovskite layers following the passivation of the HTL surface. Yamaguchi et al [122], conducted similar experiments using a similar SAM, [2-(9H-carbazol-9-yl)ethyl]phosphonic acid, commonly called 2PACz, on NiOx in an inverted PSC. They used density functional theory calculations and electron spin resonance measurements to determine the work function of NiOx. They observed an increase in the effective work function of the NiOx layer, resulting in a higher flux of electrons transferring from the perovskite layer to the HTL. This reduction in minority carrier density near the perovskite layer surface led to a decrease in the effective surface-recombination velocity, consequently enhancing both V_{oc} and Jsc values.

The final parameters used for the characterizations and tests are listed in table S3. Throughout the rest of the manuscript, this type of devices will be referred to as **bottom interface** cell and its structure is shown in figure S3b.

3.2.4. Thermal stability test

One of the expected positive side effects of SAMs in the structure of the perovskite solar cells is the increased stability [110].

Figure 3.8 shows the thermal stability test conducted for reference and *bottom interface* cells. In particular, figure 3.8d shows a considerable decrease in PCE of both samples after 1000 hours. However, the reference cells maintain 19.5% of their original performance, while the *bottom interface* cells retain 32.6%. This demonstrates how the incorporation of Me-4PACz on the top of the hole transport layer effectively improves the stability of solar cells, likely due to enhanced interface contact [109].

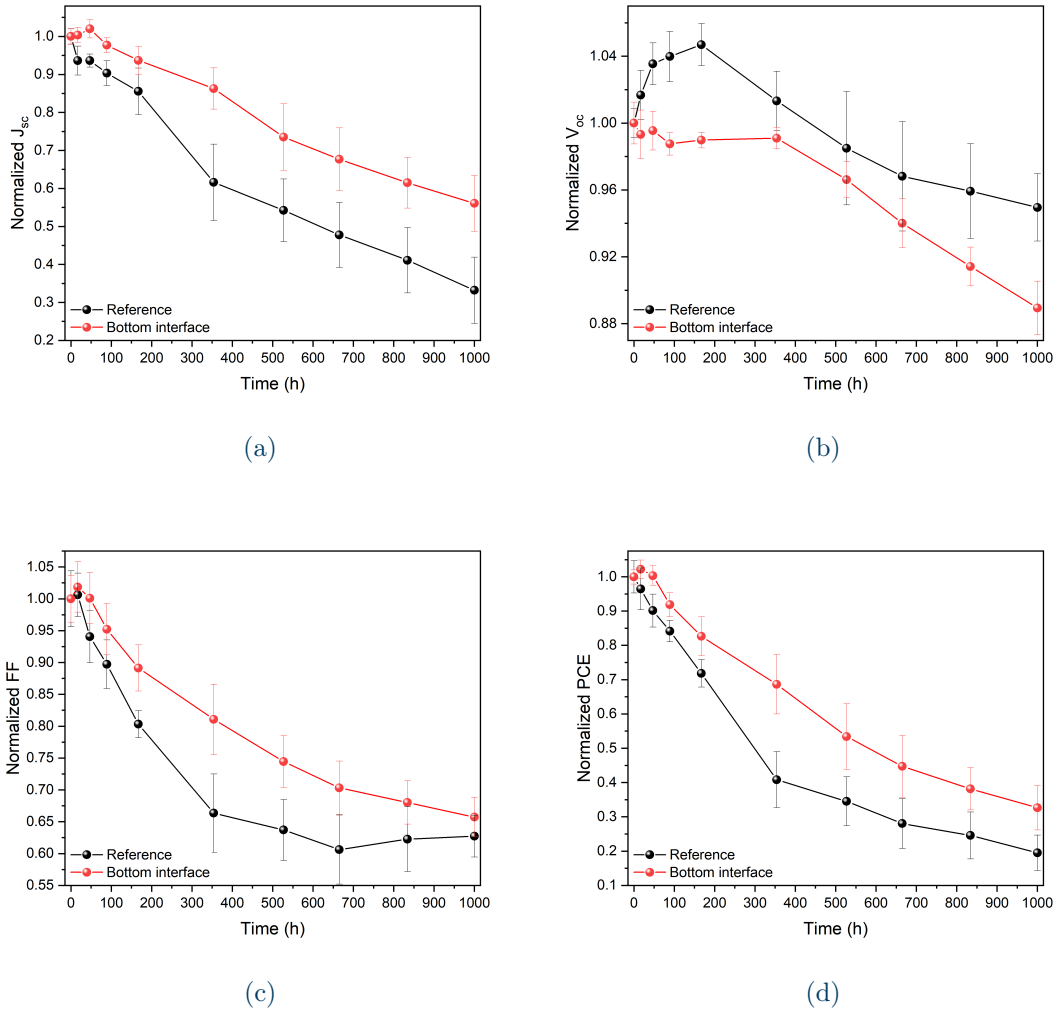

Figure 3.8: Results of the thermal stability test of (a) J_{sc} , (b) V_{oc} , (c) FF, (d) PCE of the reference and *bottom interface* cells.

3.3. Material characterizations

3.3.1. External quantum efficiency

The external quantum efficiency plot shows how efficiently the solar cell converts photons at different wavelengths into electric current.

In figure 3.9b, where the EQE spectra of the reference and *bottom interface* cells are shown, it is revealed a consistent performance for values of the wavelength between 400 nm and 800 nm, followed by a decline beyond 800 nm. This decline corresponds to a wavelength of $\sim$ 800 nm, as photons with energy below the band gap are not absorbed by the perovskite.

According to relationship 2.9, this wavelength aligns with the 1.55 eV band-gap of the perovskite used in the study.

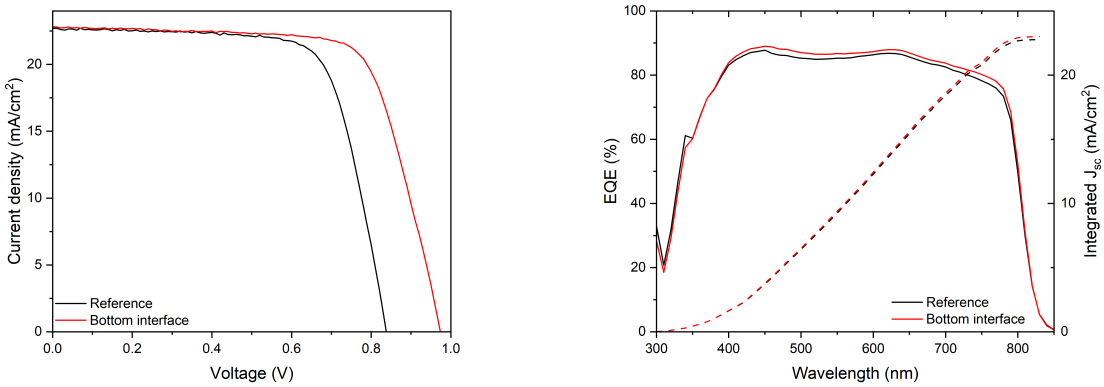

(a) (b)

Figure 3.9: (a) J-V curves and (b) EQE spectra and the integrated J_{sc} of reference and *bottom interface* cells.

The EQE plots of the two types of cells show the same behaviour, with slightly higher intensities of the *bottom interface* curve in the range of approximately 400-800 nm, compared to the reference.
This is also reflected by the current curve obtained via relationship 2.5, resulting in a slightly higher integrated J_{sc} of 23.16 mA cm^{-2} for the bottom interface device with respect to the measured 22.93 mA cm^{-2} value for the reference device. The discrepancy between the integrated J_{sc} from EQE and the values from the J-V scan in figure 3.9a is within an acceptable range of about $\sim$ 0.2 mA cm^{-2} for the reference device, and $\sim$ 0.3 mA cm^{-2} for the *bottom interface* device, respectively.

3.3.2. Photoluminescence

Photoluminescence analyses are divided into *time-resolved* and *steady-state* measurements (section 2.3.4).

The steady-state luminescence analysis of the reference and *bottom interface* cells is shown in figure 3.10. The intensity of the *bottom interface* curve is higher, pointing to possibly reduced recombination in the perovskite layer compared to the reference cell [1].

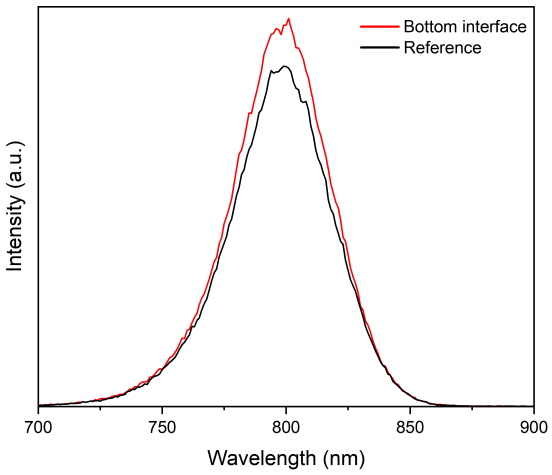

Figure 3.10: Steady-state photoluminescence of reference and *bottom interface* cells.

No horizontal shift is observed. An horizontal variation would indicate a different bandgap, but both devices utilize the same perovskite.

The time-resolved photoluminescence results of the reference and *bottom interface* cells, alongside with their exponential fitting following equation 2.8, are shown in figure S5. The parameters of the exponential fitting in figure S5 are listed in table S4.

3.3.3. Scanning electron microscopy

Top view scanning electron microscopy (SEM) was performed for both reference and *bottom interface* cells.

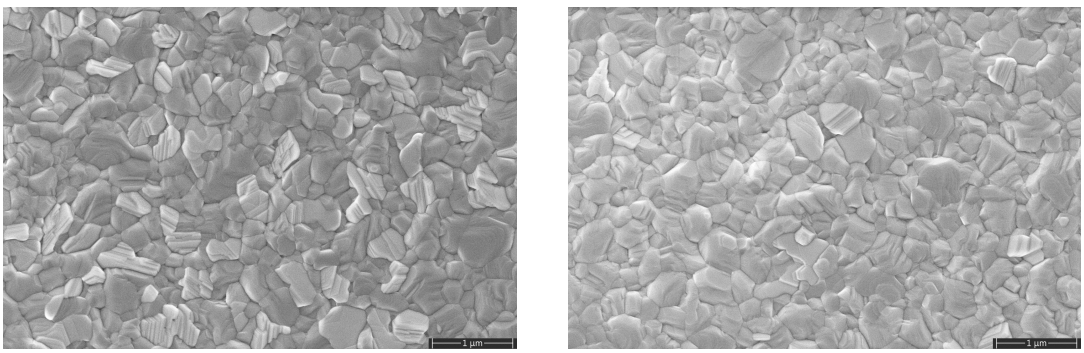

(a) (b)

Figure 3.11: Top SEM of (a) reference and (b) *bottom interface* cells.

In figure 3.11 it is possible to see the polycrystalline nature of the perovskite film and no significant differences between the two types of films, implying that with or without the Me-4PACz layer, the morphological properties are retained.

At the same time, it is possible to note the presence of a few whiter grains, visible as well in figure 3.11 and in figure 3.12, where these grains are shown at a higher magnification. This type of grains is believed to be due to residual lead iodide [123]. The presence of unreacted PbI_2 is considered the cause of intrinsic instability of the film under illumination, leading to degradation under inert atmosphere and faster degradation upon exposure to illumination and humidity [124]. The lack, or near absence, of these grains in the *bottom interface* case compared to the reference, may be linked to the slightly increased stability when NiOx is passivated with Me-4PACz.

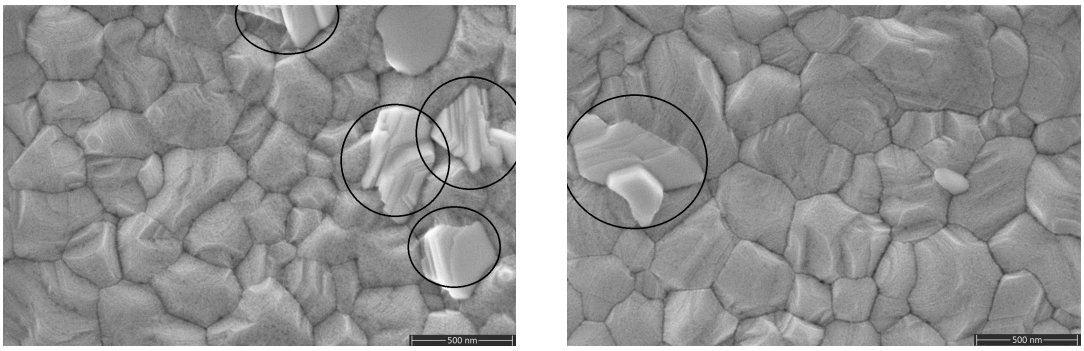

(a) (b)

Figure 3.12: Zoom of the top SEM of (a) reference and (b) *bottom interface* devices.

3.3.4. Transient photocurrent and photovoltage

To analyze the transient photocurrent and transient photovoltage results, the decay time was calculated. It is defined as the time to reach about 37% of the initial potential decay.

For TPV, the reference cell has a lower decay time (1.56 µs) compared to the *bottom interface* cell (1.61 µs), possibly indicating a better charge extraction [125]. For TPC instead, the reference cell has a *higher* decay time of 1.19 µs, with respect to the *bottom interface*'s 1.14 µs, suggesting less non-radiative recombination [126].

The decay constants for the cells in figure 3.13 are resumed in table S16.

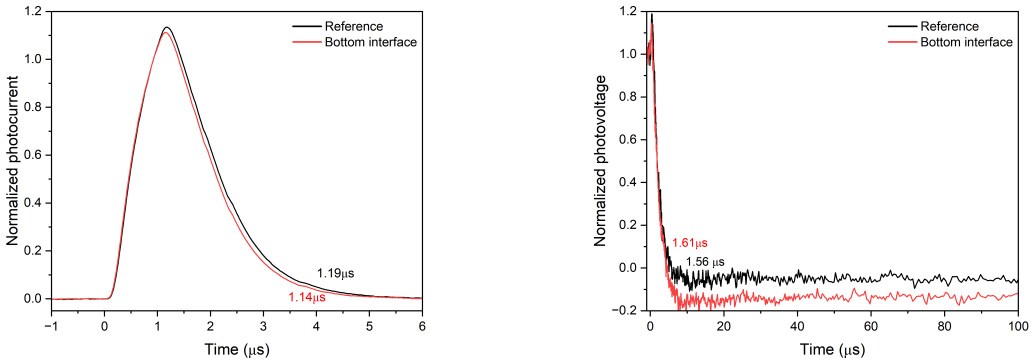

(a) (b)

Figure 3.13: (a) TPC and (b) TPV for the reference and *bottom interface* cells.

3.3.5. X-ray diffraction

The XRD patterns of the reference and *bottom interface* cells are shown in figure 3.14.

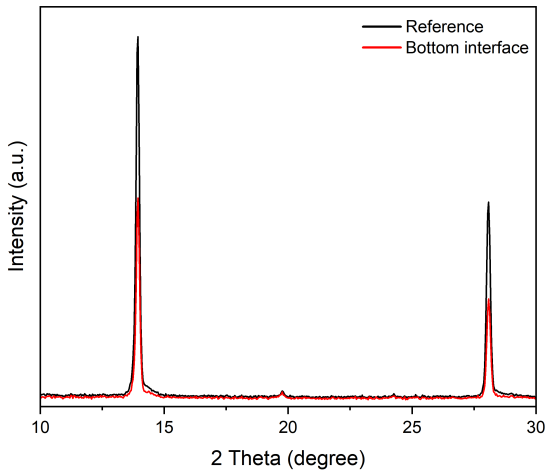

Figure 3.14: Comparison of XRD patterns of reference and *bottom interface* cells.

There are two dominant peaks, around 13.98° for the (001) plane, and around 28.3° for the (002) plane [127]. Additionally, it is possible to see how the two types of cells have the same dominant peaks, since peaks are associated to the presence of crystalline materials, a class Me-4PACz does not belong to.

An interesting approach could be to measure the XRD spectra of sputtered NiOx alone, and of sputtered NiOx and Me-4PACz on top of it, to see the differences brought by

the SAM. This was done by Alghamdi et al [1], who spin-coated (2-(3,6-Dimethoxy-9H-carbazol-9-yl)ethyl)phosphonic acid, commonly called MeO-2PACz, on sputtered NiOx. They noticed no significant differences between the two films, indicating that MeO-2PACz does not change the crystal structure of NiOx (figure S6). At the same time, analyzing the addition of the perovskite, first on top of bare NiOx and then on top of NiOx and MeO-2PACz (figure S7), they noticed more discrepancies, as for example the disappearance of a peak due to residual PbI_2, indicating improved perovskite crystallinity.

In the XRD spectra of our samples, there are no such significant variations. The peaks are the same, but it is possible to observe higher intensities in the reference curve, which might indicate enhanced crystallinity with respect to the *bottom interface* device [128]. In fact, the peak intensity in an XRD pattern is related to the number of crystallographic planes in the sample that are appropriately aligned to satisfy the Bragg's law for constructive interference.
It is important to point out that lower XRD peak intensity does not necessarily imply lower overall performance of the solar cell (which would contradict figures 3.5, 3.6, 3.7). The self-assembled monolayer is positively influencing the device in other ways, possibly through improved interface quality, surface passivation, or other beneficial effects.

A further way to gain information from the XRD data is to calculate the full width half maximum (FWHM) of the dominant peaks. The results for the plots in figure 3.14 are listed in table S5. The lower value of FWHM of the *bottom interface* device compared to the reference one, might be due to a decrease of vacancies or dislocation in the perovskite film [129].

4 | Bulk modifications

Additives can be included in the perovskite precursor to improve crystallinity, film coverage, passivation of defects and overall resulting device performance [54, 130].

In this chapter, an attempt at additive engineering was carried out, following the approach by Zheng et al [2], who obtained a power conversion efficiency of 24.5%, with the use of SAMs into the perovskite precursor. In particular, their objective was to reduce the number of processing steps: introducing a SAM into the perovskite precursor, both the hole transport layer and the perovskite spontaneously formed in one step. This means that the perovskite was deposited, in one step, directly on top of the ITO, rather than the NiOx, reducing the complexity and cost of the process. Testing different concentrations of Me-4PACz, they demonstrated that the optimal one was of $0.25\,\mathrm{mg\,mL^{-1}}$, for a 1.55 eV bandgap perovskite, similar to the one implemented in this study.

In this next section, two types of SAMs into the perovskite precursor were implemented, maintaining however the same cell structure, i.e. without eliminating NiOx, as in the case of Zheng et al.

All of the layers of the cell are the same as the reference one, and the organic solution of the perovskite is spin coated with the standard settings.

4.1. 2PACz

Other than Me-4PACz, a second SAM has been used, based on the molecule [2-(9H-carbazol-9-yl)ethyl]phosphonic acid and commonly called **2PACz**. As 4PACz (figure 4.1a), it is a carbazole based self-assembly monolayer, with one alkyl chain and two carbon atoms. The 2PACz molecule is shown in figure 4.1b.

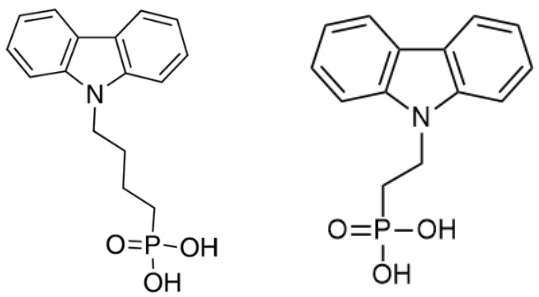

(a) (b)

Figure 4.1: (a) 4PACz structure and (b) Me-2PACz structure, from [119].

4.2. Electrical results

Both for Me-4PACz and 2PACz, three different concentrations were tested: $0.05\,\mathrm{mg\,mL^{-1}}$, $0.1\,\mathrm{mg\,mL^{-1}}$ and $0.15\,\mathrm{mg\,mL^{-1}}$. The results, in figures 4.2 and 4.3, show the cells with SAM in the perovskite precursor, compared to the reference one; the only difference lays in the perovkite, and more precisely, in the organic solution (the inorganic part, PbI_2, is thermally evaporated in the same way for all types of cells).

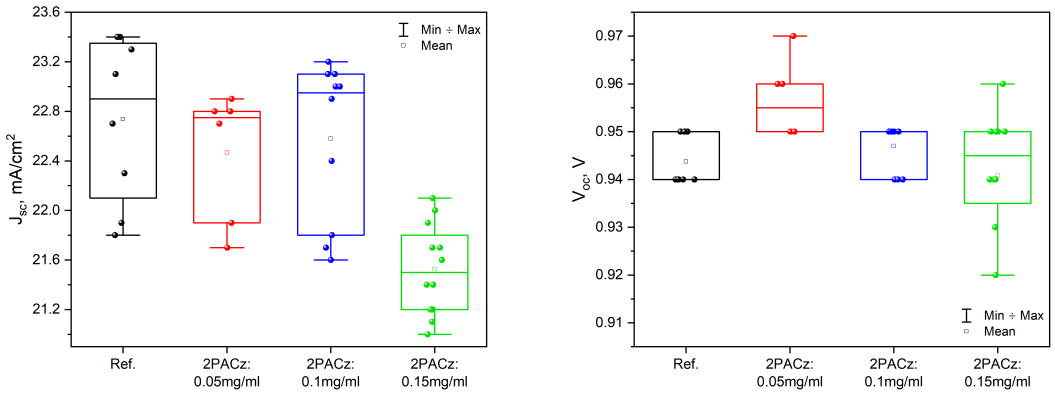

(a)

(b)

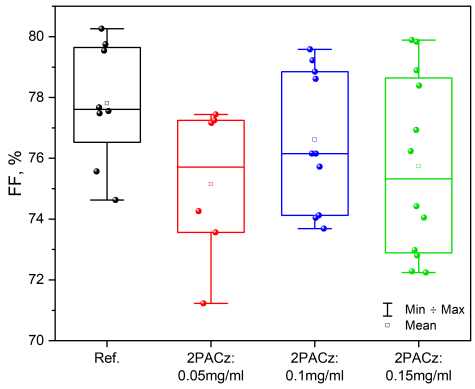

(c)

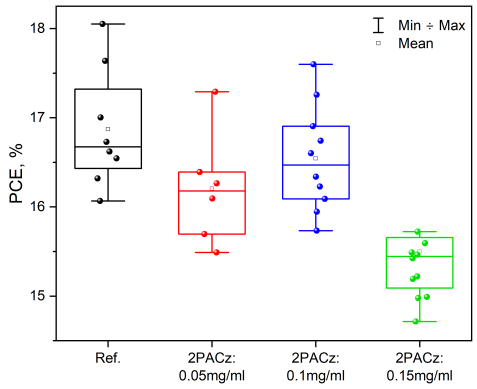

(d)

Figure 4.2: Statistics on (a) J_{sc} , (b) V_{oc} , (c) FF, (d) PCE of cells: reference and different concentrations of 2PACz in the perovskite precursor solution.

For 2PACz, all of the values seem to be lower than the reference, except for the V_{oc} , which is comparable. Overall, looking at the PCE, in figure 4.2d, we can affirm 2PACz in the perovskite precursor solution does not benefit the performance.

The same can be observed for Me-4PACz, in figure 4.3, where no concentrations seem to have positive effects.

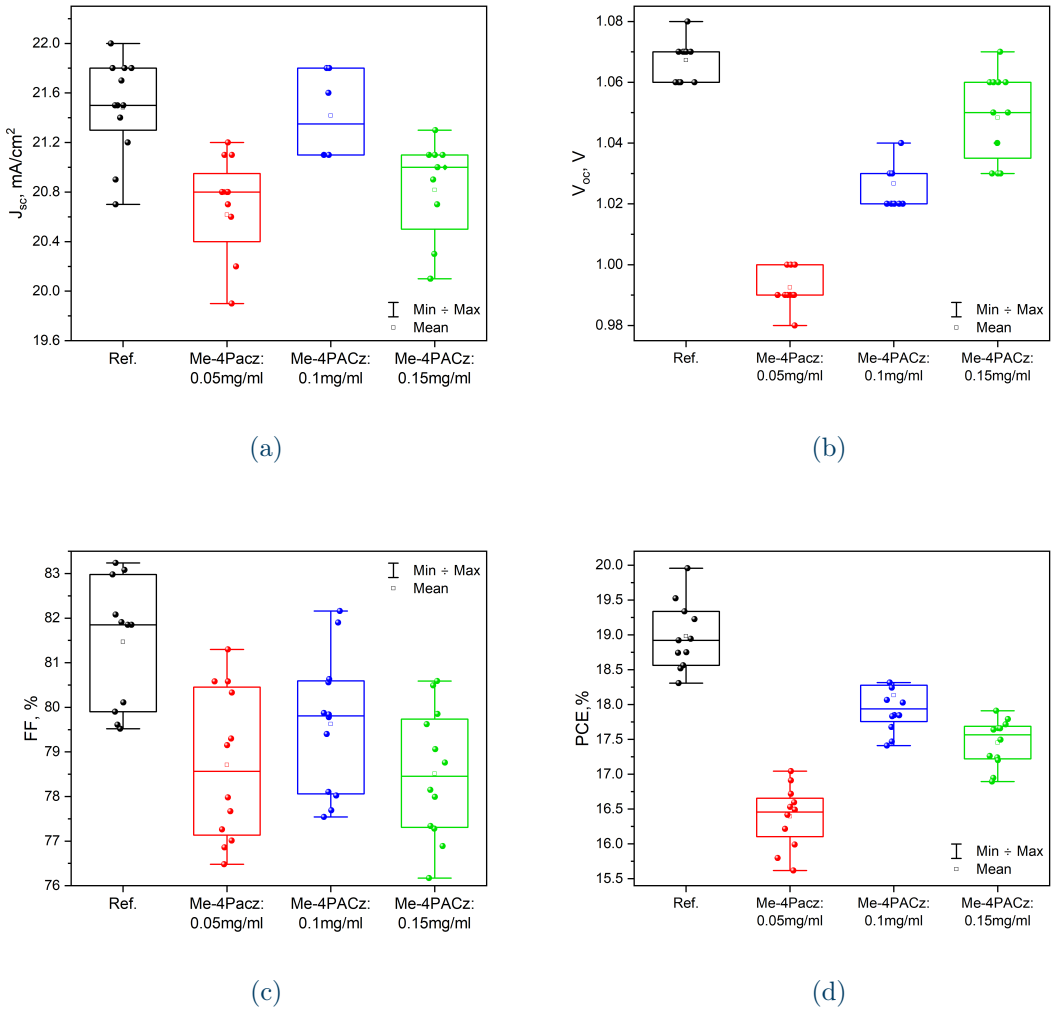

Figure 4.3: Statistics on (a) J_{sc} , (b) V_{oc} , (c) FF, (d) PCE of cells: reference and different concentrations of Me-4PACz in the perovskite precursor solution.

Increasing the concentrations even further to $0.2\,\mathrm{mg\,mL^{-1}}$ and $0.4\,\mathrm{mg\,mL^{-1}}$, leads to an even worse performance (figure S8).

The difference between these results and those of Zheng et al [2], may be partly due to the diverse structures of the devices. Firstly, they did not incorporate a hole transport layer (NiOx) in their work, a component that we chose to include in our cells. Secondly, they utilized a different perovskite, deposited in one step, whereas we employed a two-step sequential deposition process.

4.3. Material characterizations

The characterizations and tests were carried out on cells with Me-4PACz on top of NiOx (*bottom interface* cell) and a 0.1 mg mL^{-1} concentration of Me-4PACz in the perovskite precursor.
The final choice of layers is listed in table S6 and throughout the rest of the manuscript, this type of cell will be referred to as **Me-4PACz treated** (figure S3c). In simpler terms, the *Me-4PACz treated* cell is the *bottom interface* cell (table S3) with a difference in the perovskite organic solution, which includes Me-4PACz.

4.3.1. External quantum efficiency

The EQE spectra in figure 4.4 for the *Me-4PACz treated* devices are shown in figure 4.4b. As expected from the results in figure 4.3a, the *Me-4PACz treated* curve is slightly lower than the *bottom interface* one, with values of integrated J_{sc} of 22.69 mA cm^{-2} and 23.16 mA cm^{-2} respectively.

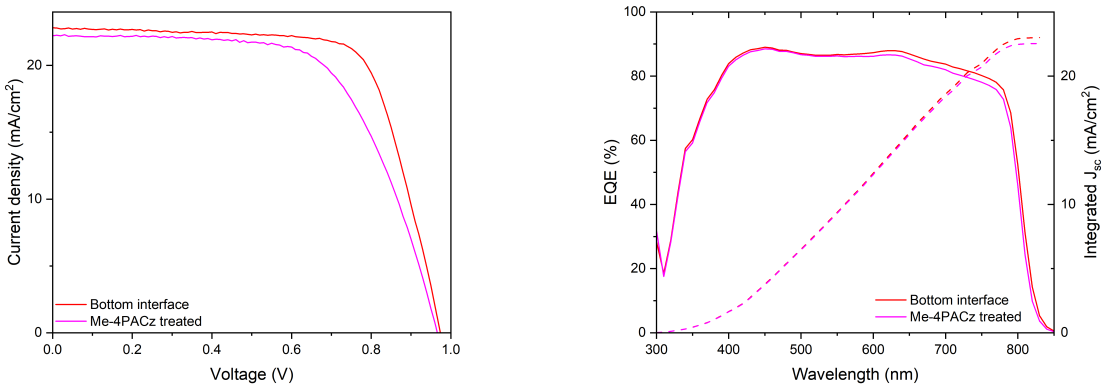

(a) (b)

Figure 4.4: (a) J-V curves and (b) EQE spectra and the integrated J_{sc} of *bottom interface* and *Me-4PACz treated* devices.

The discrepancy between the integrated J_{sc} from EQE and the values from the J-V scan in figure 4.4a is about $\sim$ 0.8 mA cm^{-2} for the *Me-4PACz treated* device, and about $\sim$ 0.9 mA cm^{-2} for the *bottom interface* devices.

Furthermore, in figure 4.4a, the *Me-4PACz-treated* slope is less pronounced than the *bottom interface* one, indicating that the series resistance is higher [131]. It may be due

to the presence of non-conducting molecules, belonging to the SAM, which hinder the transport of charges.

4.3.2. Photoluminescence

Figure 4.5 displays the steady-state luminescence analysis of both the *bottom interface* and *Me-4PACz treated* cells.
The *bottom interface* curve exhibits a lower intensity, suggesting a potential reduction in the recombination of electron-hole pairs compared to the *Me-4PACz treated* cell [132]. Additionally the graph reveals an unchanged horizontal position of the peak, implying that the bandgap remains unaltered after the inclusion of Me-4PACz in the perovskite precursor.

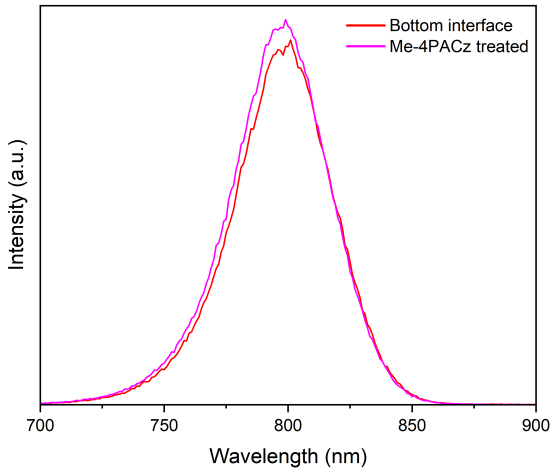

Figure 4.5: Steady-state photoluminescence of *bottom interface* and *Me-4PACz treated* cells.

The time-resolved photoluminescence results of the *bottom interface* and *Me-4PACz treated* cells, alongside with their exponential fitting following equation 2.8, are shown in figure S9. The parameters of the exponential fitting in figure S9 are listed in table S7.

4.3.3. X-ray diffraction

The XRD patterns of the *bottom interface* and *Me-4PACz treated* cells are shown in figure 4.6, alongside the FWHM values listed in table S5.

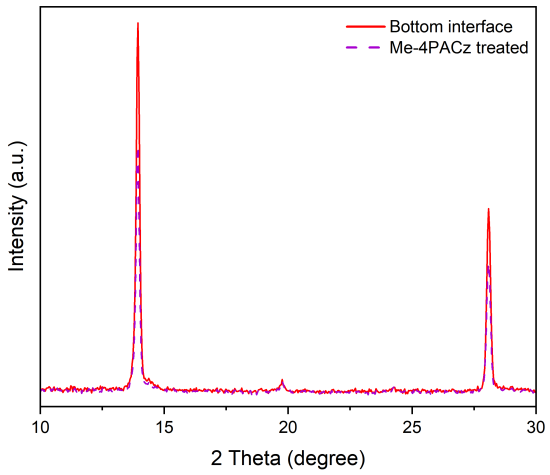

Figure 4.6: Comparison of XRD patterns of *bottom interface* and *Me-4PACz treated* cells.

As in figure 3.14, showing the XRD plot of the reference and *bottom interface* devices, the two samples have the same peaks, with a difference in the intensity. In this case, the *bottom interface* films have higher intensity, indicating a possible enhanced crystallinity with respect to the *Me-4PACz treated* ones.
The differences observed in the XRD plot may be due to alterations in the crystal structure of the resulting perovskite film. In fact, Me-4PACz could have influenced the nucleation and growth of the perovskite crystal, leading to differences in crystal size, orientation, and overall morphology. For example, Zheng et al [2] noticed, with the help of scanning electron microscopy images (figure S10), that the average grain size of a perovskite film with Me-4PACz in $0.5\,\mathrm{mg\,mL^{-1}}$ concentration is slightly larger than that of a perovskite film without the SAM; increasing the concentration of Me-4PACz to $2\,\mathrm{mg\,mL^{-1}}$ instead, reduces the size again.

5 | Top layer modifications

Once both the interface between hole transport layer and perovskite, and the perovskite itself, have been altered, the only (relevant) interface left is the top one, between perovskite and ETL. In this case, as for the additives in the perovskite structure (chapter 4), several can be the approaches: Lewis acids/bases [133], polymers [134], organic halide salts [135], SAMs [112] and more.

For this work, two inorganic salts, caesium iodide (CsI) and caesium bromide (CsBr), were employed on top of the perovskite surface.

It is crucial to point out that realizing modifications on the upper interface could be more critical than realizing them on the lower one, due to the delicate nature of the perovskite layer, posing a challenge in discerning whether the applied modifications are effectively detrimental to the overall cell performance, or solely harmful to the integrity of the perovskite. As a consequence, the initial focus was exclusively dedicated to investigating the influence of solvents on the perovskite surface integrity.

The choice of solvents was dictated by the inorganic salts themselves, CsI and CsBr, knowing with certainty of their solubility in methanol [136]. Methanol is a highly polar solvent, where polarity is, as defined by Katritzky et al [137], the "capacity of a solvent for solvating dissolved charged or dipolar species". In simpler terms, polar solvents, which have large dipole moments, can dissolve substances with similar polarities, such as ionic or polar compounds.
Solvents can be classified as more or less polar, based on a scale [138], where water is at the top of the list. Generally, a more polar solvent might be considered "stronger", as it is more effective in dissolving salts. However, this strength could potentially lead to increased damage to the perovskite, adding an additional layer of complexity to the solvent selection process.

5.1. Influence of different solvents on the perovskite surface

Testing the influence of the solvents, involved spin coating 100 µL of methanol, ethanol or isopropanol onto the perovskite surface, at 3000 rpm for 30 seconds, followed by annealing at 100 °C for five minutes.

Given that solvents evaporate, as observed in the rinsing step detailed in chapter 3, they do not constitute an additional layer, thus no effects are expected from the solvent. If a

worse performance of the cell is observed, the solvent has likely damaged the perovskite surface.

Regarding the solvents, methanol is more polar than ethanol, followed by IPA. From previous experience in the laboratory, IPA has no known effect on the used perovkite, hence the the most interesting results would be the one of ethanol and methanol.

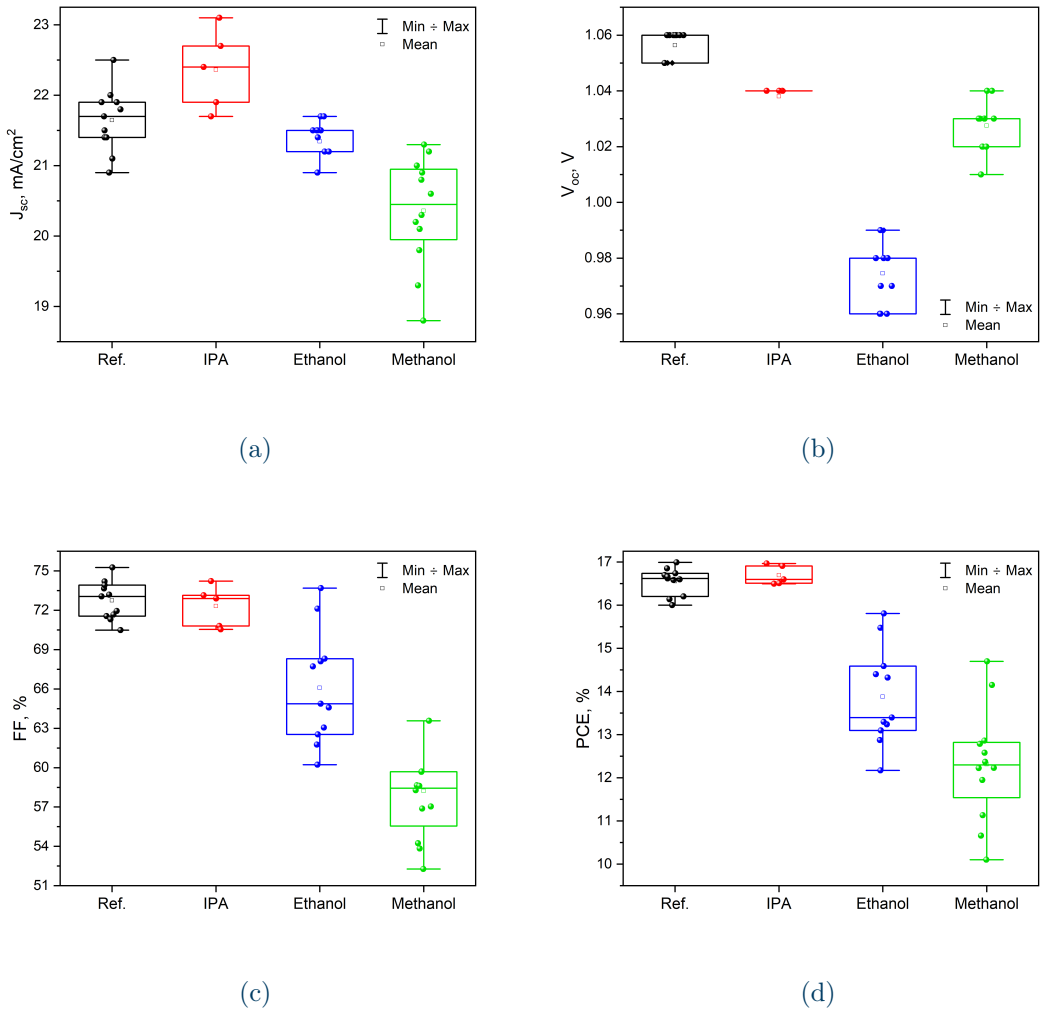

Figure 5.1: Statistics on (a) J_{sc} , (b) V_{oc} , (c) FF, (d) PCE of cells: reference and different solvents on the perovskite surface.

The results in figure 5.1, confirm what was expected. The samples with IPA, the least polar solvent, have a very similar performance to the reference cell; on the contrary, as the polarity of the solvent grows, from IPA to ethanol to methanol, the performance degrades, indicating damage to the perovskite surface. These results lead us to the conclusion that

using methanol or ethanol, will not boost the performance, independently of the salt itself.

5.2. The solubility issue

While the effect of the solvent on the perovskite is of elementary importance, a second crucial factor to consider is the solubility of the two salts. As a consequence, coincidentally with the "solvent tests", the strength of methanol, ethanol and IPA on CsI were tested (only CsI was used, due to the similar nature of CsI and CsBr).
As learnt from Baumeler et al [136], who examined the same materials on a slightly different perovskite solar cell, CsI is soluble in methanol. Following their results, who concluded that the optimal concentration of CsI for passivation of their devices was of $2.5\,\mathrm{mg\,mL^{-1}}$, we obtained both a $2.5\,\mathrm{mg\,mL^{-1}}$ and $5\,\mathrm{mg\,mL^{-1}}$ solution of CsI in methanol, requiring only a few hours in the ultra-sonicator.
Challenges emerge with less polar solvents. Using ethanol, only a $2.5\,\mathrm{mg\,mL^{-1}}$ solution was achieved, whereas a $5\,\mathrm{mg\,mL^{-1}}$ solution failed to dissolve. Clearly, using IPA, the least polar solvent, the dissolution of the salt becomes even more challenging: not even a $1\,\mathrm{mg\,mL^{-1}}$ solution was accomplished.

Combining these results with those showed in figure 5.1, a seemingly unbeatable challenge rises: ethanol and methanol effectively dissolve the salt but harm the perovskite, whereas IPA leaves the surface unaffected, but a solution of CsI with it is not achievable.
A tentative approach to divert from these problems, detailed in section 5.3, is the introduction of a "protection layer" between the perovskite and the solution of salt; this would allow the use of more polar solvents, such as methanol, but at the same time adding an additional layer of complexity to the choice of materials and the structure of the cell.

Table S8 lists the relevant results obtained for different solvents and percentages of them, in terms of dissolution of CsI. The results obtained with different percentages of IPA and ethanol spin coated on the perovskite surface, are shown in figure S11.

5.3. Use of a protection layer for the perovskite

The protection layer of choice was constituted by a solution of thiopheneethylammonium iodide (TEAI), spin coated on top of the perovskite and afterwards annealed.

A first test was carried out, with TEAI only followed by ethanol or methanol (IPA was no longer considered, due to its inability to dissolve CsI). The samples are compared to the *bottom interface* cell (all of the samples, when compared to the *bottom interface* cell rather than the *reference* one, have Me-4Pacz on top of NiOx as well).

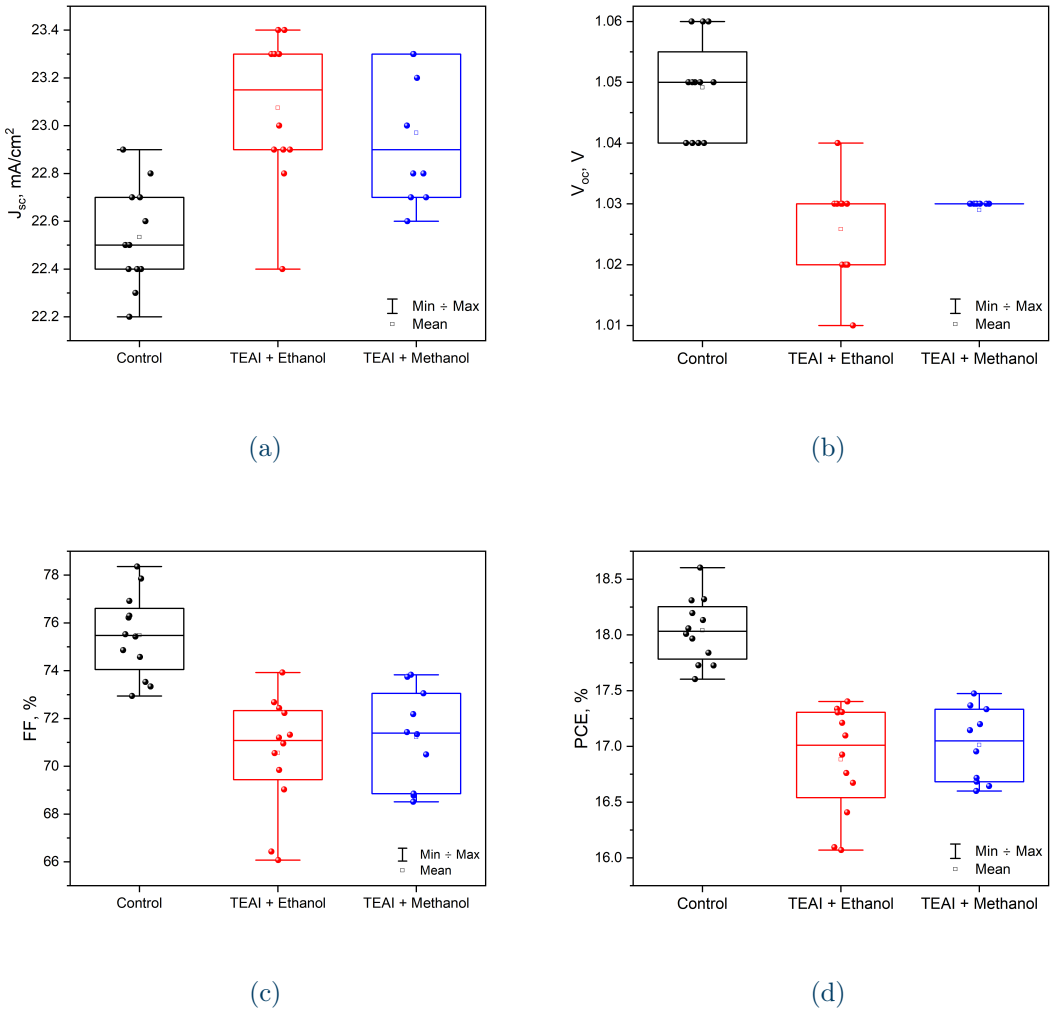

Figure 5.2: Statistics on (a) J_{sc} , (b) V_{oc} , (c) FF, (d) PCE of cells: *bottom interface* and different solvents combined with the protection layer (TEAI).

From the results in figure 5.2, two clear conclusions can be drawn. With the addition of the protection layer, the differences between methanol and ethanol become almost irrelevant: the two performances, in red and blue in figure 5.2, are essentially equivalent, contrarily to figure 5.1, where the higher polarity lead to a worsening effect on the results. On a second note, despite the incorporation of TEAI, there is a clear drop in the performance. Ideally, a good result would lead to no differences compared to the *bottom interface* cell, analogously to those cells treated solely with plain IPA on top of the perovskite surface (figure 5.1). The observed disparity in results suggests that even with the protective layer, the two polar solvents damage the perovskite surface.

This issue is observed with the addition of CsI as well, always following TEAI, for solutions

of CsI both in ethanol and methanol (figure S12). The salt solution was spin coated with the same settings.

Different combination of settings of the spin coating could still be tried: varying speed and time of rotation, the thickness of the resulting layer changes. After the results of the "solvent tests" though, we assumed safe to conclude that the main issues, the solubility and the deterioration of the perovskite, derive from the use of solvents.

What if there was a way to include the salts *without* solvents? This could be done via thermal evaporation. It would have different advantages: in terms of time for example, due to the fact that the thermal evaporation includes all samples at once, while the spin coating has to be executed sample by sample. Additionally, it would eliminate the need for solvents. Most importantly, successful evaporation could serve as a valuable asset for scaling up, eliminating the spin coating, which is not effective for large area cells [79].

5.4. Evaporated CsI and CsBr

Evaporating the two salts, the most crucial parameter to control is the thickness. Different thicknesses were tested, starting from as thin as 0.3 nm, up to 4 or 5 nm.

Regarding CsI, slightly better results were observed for 1.5 nm (figure S13) than for thinner layers. This encouraged us to increase the thickness, up to 4nm, as shown in figure 5.3. It is possible to see a slight improvement for a thickness of 3nm, while increasing to 4nm leads to a drop in the performance.

Regarding CsBr instead, the results were similar, but no thickness exceeded the performance of the *bottom interface* devices (figure S14).

To conclude, the presence of 3 nm of evaporated CsI seems to have a slightly positive influence on the performance of the cell.

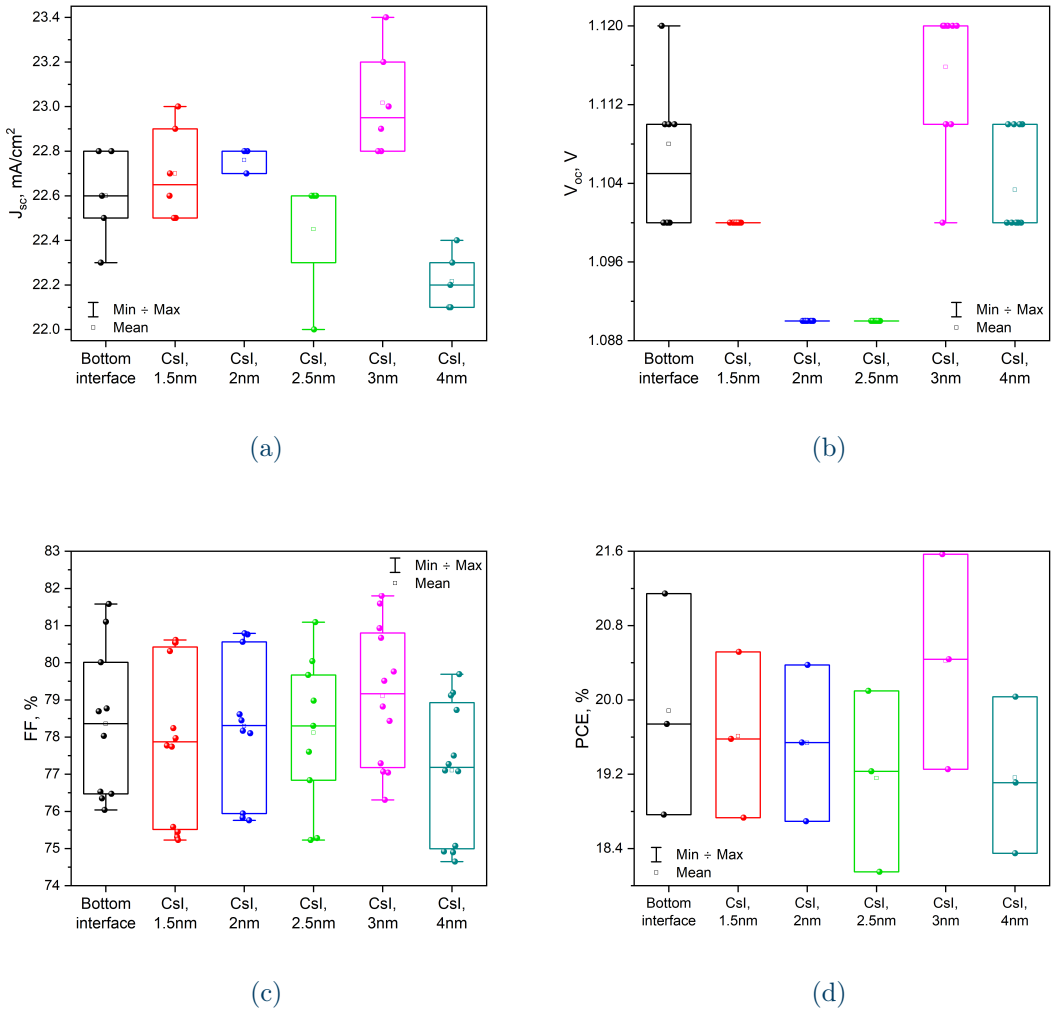

Figure 5.3: Statistics on (a) J_{sc} , (b) V_{oc} , (c) FF, (d) PCE of cells: *bottom interface* and evaporated CsI.

5.5. Thermal stability test

The tests were carried out for both reference and *bottom interface* cells with the addition of 3nm of evaporated CsI between the perovskite layer and the ETL, referred to as **reference + CsI**, and **bottom interface + CsI** devices.
They are described in tables S9 and S10, and shown in figure S3d and S3e respectively.

In the thermal stability test, a small modification to the cell structure was made to include a further examination in the same test.
The reason behind this lays in the LiF layer, depicted by us as a built-in part of the ETL, which is actually an additional layer introduced for surface passivation [82].

Notably, Baumeler et al. [136] suggest that the CsI layer is expected to contribute to stability improvement. To assess whether the CsI *alone* can enhance stability without the presence of LiF, cells of the same type were fabricated with and without LiF. If this were successful, it would eliminate the need for the LiF layer, reducing material and time consumption.

The first results in figure 5.4 show the comparison between the reference cell (table S1), the reference cell with the addition of CsI but not LiF, and the reference cell with both CsI and LiF (table S9).
For clarity, table S11 lists the stack of the three samples in figure 5.4 (please note that the ITO between electron transport layer and metal is introduced only for the sake of the thermal stability test, as detailed in section 2.3.2).

The same analysis was done for the *bottom interface* cells in figure 5.5: *bottom interface* cells (table S3) were compared to those with the addition of CsI without LiF and with the addition of both CsI and LiF (table S10).
Table S12 lists the stack of the three types of cells of the test in figure 5.5.

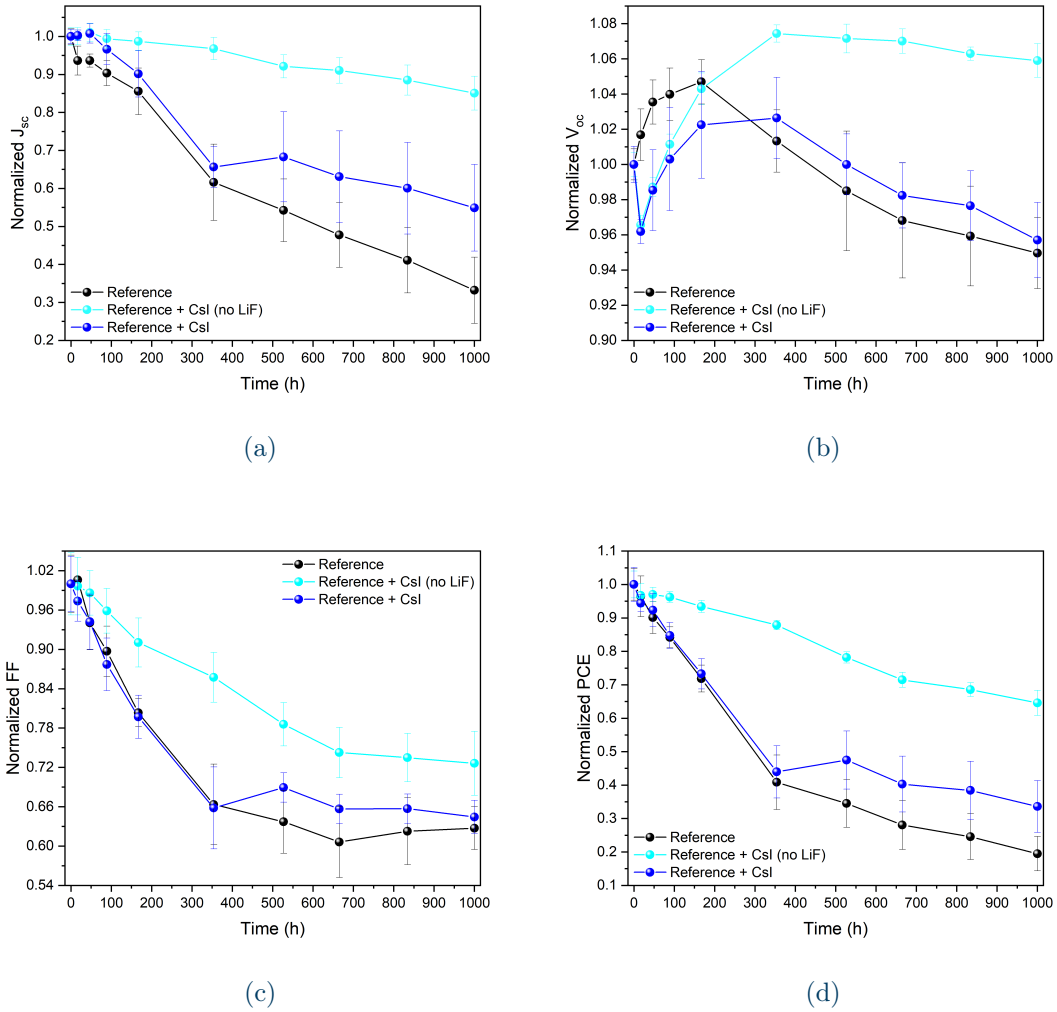

Figure 5.4: Results of the thermal stability test of (a) J_{sc} , (b) V_{oc} , (c) FF, (d) PCE of the reference and cells with CsI, with and without LiF.

From figure 5.4d, it is possible to observe a significant difference between the cells with and without CsI. Specifically, while the reference cells sustain 19.5% of their initial performance, the *reference + CsI* cells in blue retain 33.6%. This is a similar value to the *bottom interface* cell, which has a final performance of 32.6%. Therefore, the addition of Me-4PAcz on top of the HTL or the evaporation of CsI before the ETL, yield comparable results in terms of stability.

Additionally, when LiF is removed from the ETL, the PCE after 1000 hours is higher. The light blue curve in figure 5.4d maintains 64.6% of the initial PCE, in contrast to the blue curve, which retains 33.6%.

The same behaviour can be observed for the *bottom interface* cells in figure 5.5. The samples with CsI maintain a higher performance, respectively 45.6% and 54.9% with and without LiF, while the *bottom interface* cell retains 32.6% of the initial performance.

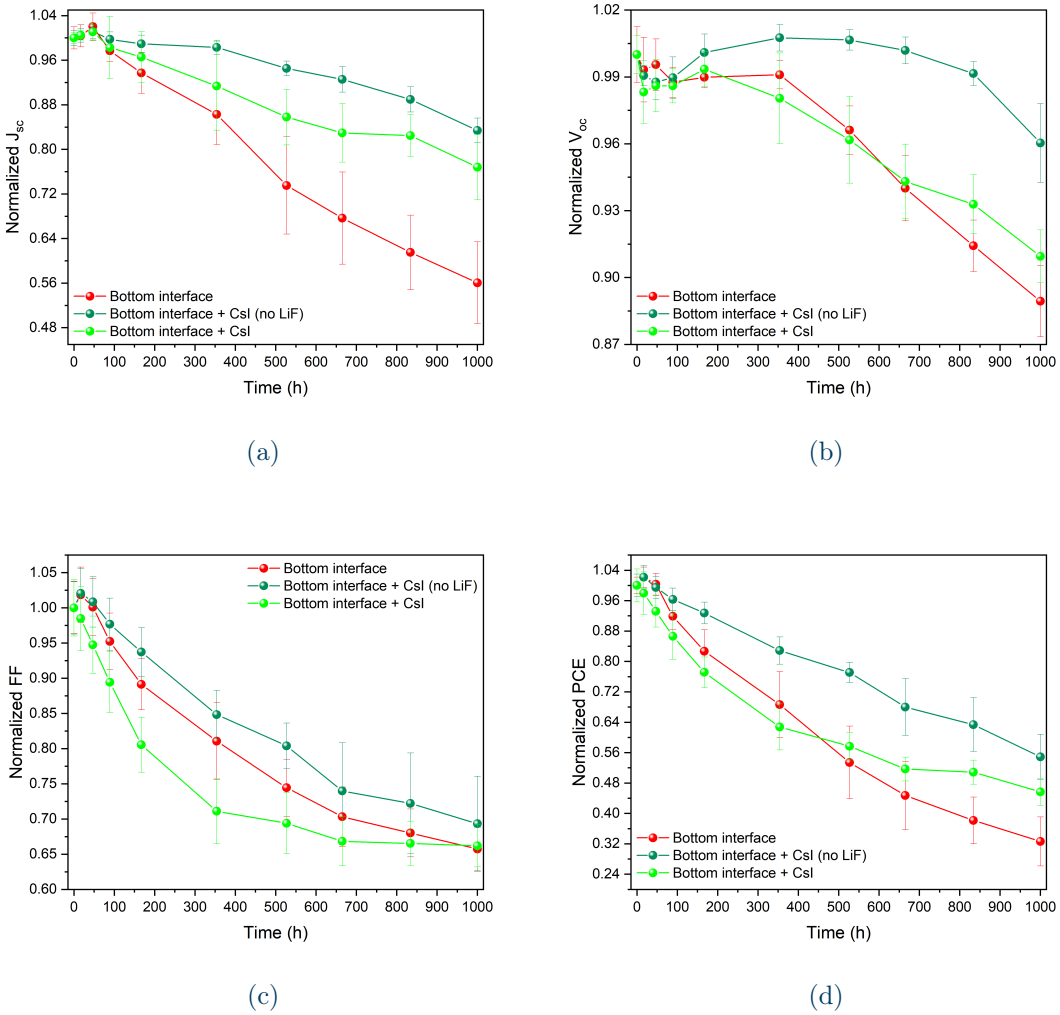

Figure 5.5: Results of the thermal stability test of (a) J_{sc} , (b) V_{oc} , (c) FF, (d) PCE of the *bottom interface* and cells with CsI, with and without LiF.

Examining figure 5.6 provides insights into the PCE over time for all types of devices, allowing us to draw conclusions on the impact of the various added layers on stability.
The two higher curves are for those devices *with* CsI but *without* LiF. The middle two curves are for devices *with* CsI *and* LiF. The two lowest results are for those devices *without* CsI, and the addition only of Me-4PACz between the HTL and the perovskite, or the reference cell alone.
These findings support the notion of CsI contributing positively to stability, while high-

lighting the unfavorable influence of LiF in terms of stability.

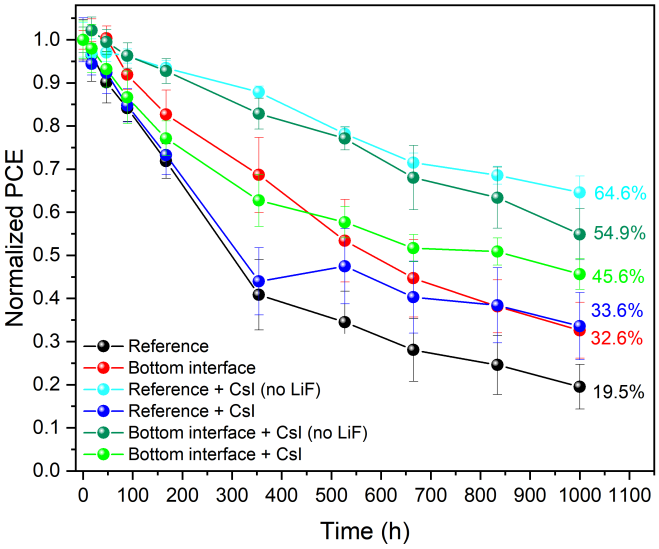

Figure 5.6: Results of the thermal stability test of *PCE* of all types of cells.

A peculiar phenomenon that can be observed is how, while for the *bottom interface* device the Me-4PACz helps with the stability when compared to the reference devices, when CsI is added (and LiF removed), the Me-4PACz is no longer advantageous. Several factors could account for this, and conducting tests with a larger amount of samples for a more accurate statistical analysis may help confirm these findings. Additionally, it is important to note that while Me-4PACz may not be as beneficial in terms of stability, it is in terms of initial performance.

A second aspect that can be pointed out is the significantly reduced PCE values observed after the thermal stability test. Typically, literature suggests an anticipated PCE range of 70% to 90% after 1000 hours, in contrast to the observed low values of around 20%. These reduced values are probably due to the BCP, the last component of the ETL, which is confirmed to show fast aggregation at the temperature of 85°C [139]. For thermal stability tests, it is wiser to replace the BCP with inorganic metal oxides to exclude its negative effect.

5.6. Material characterizations

5.6.1. External quantum efficiency

The analyses were carried out for the *reference + CsI* cells (table S9) and the *bottom interface + CsI* devices (table S10).

The EQE plots of reference and *bottom interface* cells with evaporated CsI between the perovskite and the electron transport layer are shown in figure S15b and 5.7b respectively. The values of J_{sc} are for 23.16 mA cm^{-2} and 23.36 mA cm^{-2} for the bottom interface devices, with and without CsI respectively, and of 22.93 mA cm^{-2} and 23.14 mA cm^{-2} for the reference devices.
The discrepancy between the integrated J_{sc} from EQE and the values from the J-V scan in figures S15a and 5.7a is about 22.69 mA cm^{-2} $\sim$ 0.7 mA cm^{-2} for the *bottom interface* device and 0.8 mA cm^{-2}for the *bottom interface* device.

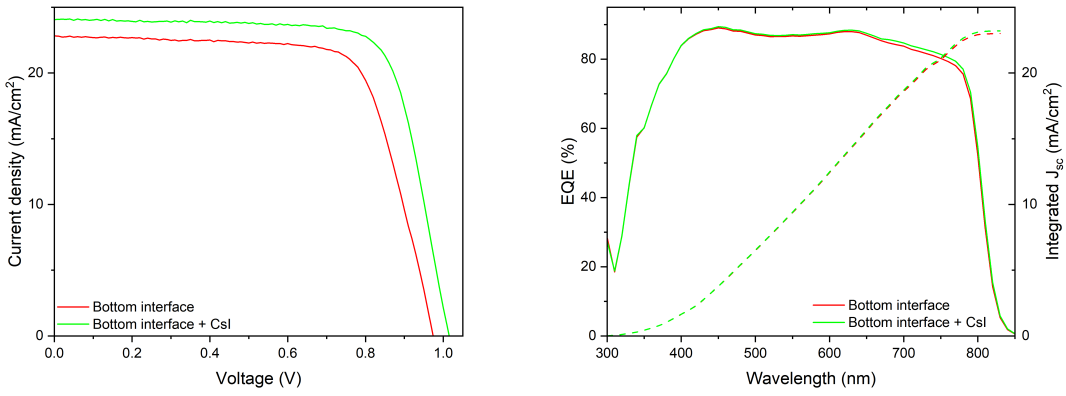

(a) (b)

Figure 5.7: (a) J-V curves and (b) EQE spectra and the integrated J_{sc} of *bottom interface* and *bottom interface + CsI* devices.

The EQE curves of all the types of cells, alongside a table containing all the values of integrated and measured J_{sc}, are shown in figure S16 and table S13.

5.6.2. Photoluminescence

In the steady-state luminescence analyses, the application of CsI over the perovskite seems to have the same consequences, both in the reference and *bottom interface* case, as shown in figure 5.8. In fact, both the reference and *bottom interface* curves have higher intensities than their counterparts without salt, with the same position of the peak with respect to the wavelength.

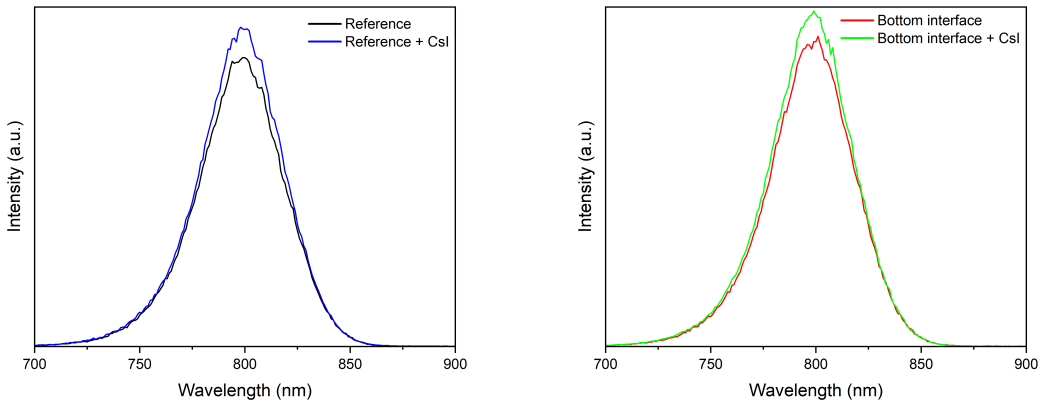

(a) (b)

Figure 5.8: SSPL of (a) reference and *reference +CsI* cells and (b) *bottom interface* and *bottom interface + CsI* cells.

The time-resolved photoluminescence results of the cells with CsI on top of the perovskite, alongside their exponential fitting following equation 2.8, are shown in figure S17. The parameters of the exponential fitting in figure S17 are listed in table S14.
Figure S18 and table S15 show and list the TRPL plots and exponential fitting data for all types of cells.

The steady-state photoluminescence curves of all types of cells are shown in figure S19.

5.6.3. Scanning electron microscopy

Figure 5.9 shows the top SEM of the reference cell, compared to the *bottom interface* with CsI on top of the perovskite (*bottom interface + CsI*, described in table S10 and shown in figure S3e).
There is a clear difference between the two films: the presence of the whiter grains due to residual PbI_2 is no longer visible when CsI is evaporated on top of the perovskite. This confirms the relationship between residual PbI_2 and stability: with the evaporation of CsI, the white grains are no longer visible and the performance in time is greatly improved, as confirmed by the thermal stability test, in figures 5.4 and 5.5.

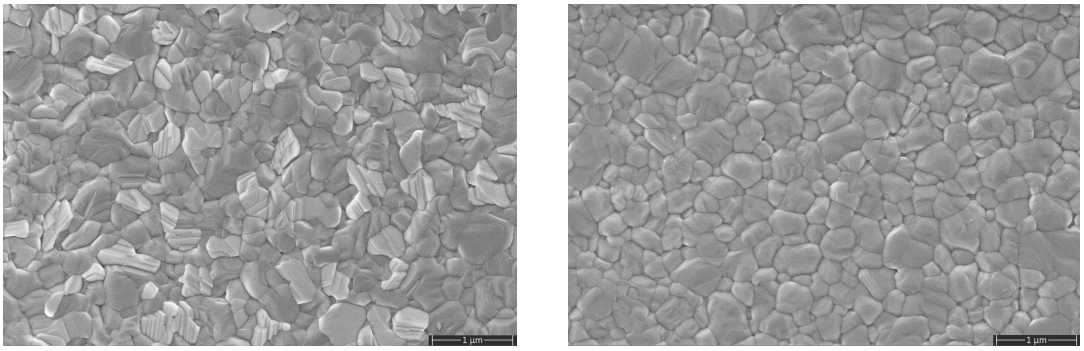

(a) (b)

Figure 5.9: SEM of (a) reference and (b) *bottom interface + CsI* cells.

5.6.4. Transient photocurrent and photovoltage

Similarly to the photoluminescence analyses, we conducted TPC and TPV analyses on *reference + CsI* cells (table S9).

The decay time of the reference cell for TPC is lower than the relative cell with the addition of CsI, denoting a better charge extraction. For TPV the reference cell has a higher decay time indicating less non-radiative recombinations.

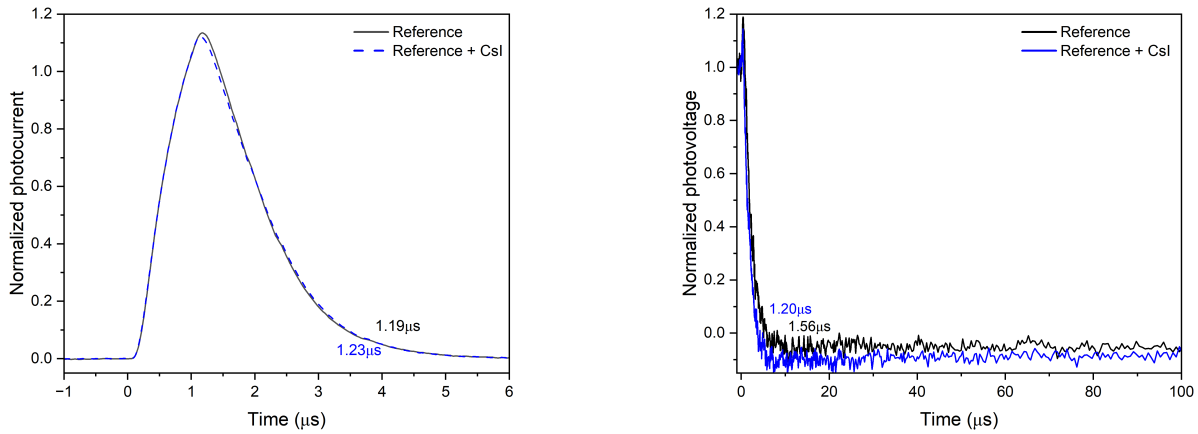

(a) (b)

Figure 5.10: (a) TPC and (b) TPV for the reference and *reference + CsI* cells.

The decay constants for the cells in figure 5.10 are resumed in table S16.
Figures S20 and S21 contains the TPC and TPV plots for the three types of cells (reference, *bottom interface* and *reference + CsI*).

5.6.5. X-ray diffraction

The XRD patterns of the *reference + CsI* and *bottom interface + CsI* cells are shown in figure 5.11, alongside with the FWHM values listed in table S5.
It is possible to observe the same peaks present also in the case of the Me-4PACz treated films (figure 4.6). The reference cells with CsI on top of the perovskite have lower intensity with respect to the reference, implying a worse crystallinity. The same happens for the *bottom interface* cells with CsI, which have lower values than the *bottom interface* counterparts.

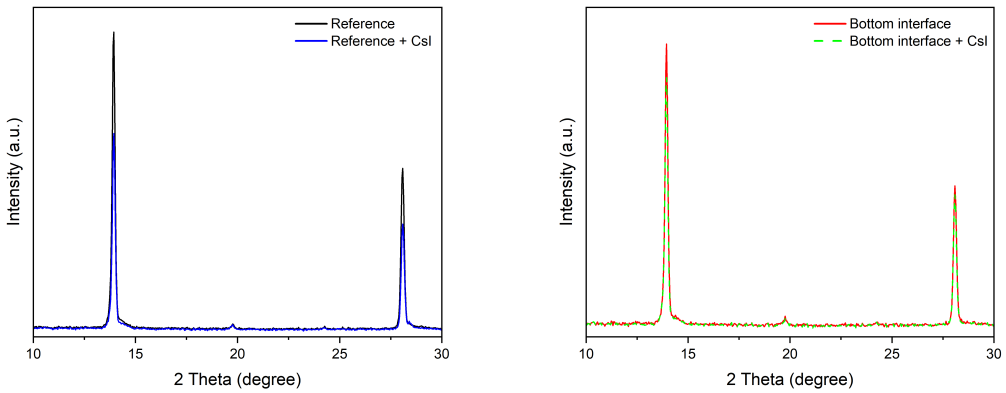

(a) (b)

Figure 5.11: XRD of (a) reference and *reference + CsI* cells and (b) *bottom interface* and *bottom interface + CsI* cells.

6 | Conclusions

In this study, interface engineering techniques were applied to medium-bandgap perovskite solar cells to enhance their efficiency and stability over time.
Passivation of the hole transport layer surface with Me-4PACz resulted in a significant increase in the open-circuit voltage, thereby boosting the overall power conversion efficiency. However, implementation of the same material into the perovskite precursor solution led to performance losses.
Engineering of the interface between the perovskite layer and the electron transport layer using inorganic salts provided valuable insights. This included the influence of different solvents on the perovskite surface and the comparative advantages of thermal evaporation over spin coating. Notably, the deposition of CsI on top of the perovskite hinted at potential positive effects, indicating possibilities for further investigation to optimize device performance.

The investigation into the thermal stability revealed the roles of CsI, Me-4PACz, and LiF on the long-term durability of the devices. While our study involved a limited number of devices tested over 1000 hours, expanding the sample size and conducting other types of stability tests will provide a more comprehensive understanding of stability, a fundamental aspect in the advancement of perovskite solar cell technology.

Furthermore, spectroscopy techniques were employed to gather further insight into the behavior of the passivated devices. Initial interpretations were made based on the obtained results and existing literature on similar devices, and further investigation is necessary to validate these assumptions and expand our understanding.

In conclusion, this work highlights the role and the struggles of interface engineering in enhancing the performance and stability of perovskite solar cells. The findings contribute to the ongoing efforts to develop efficient and sustainable future.

Bibliography

[1] Amira R. M. Alghamdi, Masatoshi Yanagida, Yasuhiro Shirai, Gunther G. Andersson, and Kenjiro Miyano. Surface passivation of sputtered niox using a sam interface layer to enhance the performance of perovskite solar cells. *ACS Omega*, 7(14):12147–12157, 2022.

[2] X. Zheng, Z. Li, Y. Zhang, M. Chen, T. Liu, C. Xiao, D. Gao, J. Patel, D. Kuciauskas, A. Magomedov, R. Scheidt, X. Wang, S. Harvey, Z. Dai, C. Zhang, D. Morales, H. Pruett, B. Wieliczka, A. Kirmani, N. Padture, K. Graham, Y. Yan, M. Nazeeruddin, M. McGehee, Z. Zhu, and J. Luther. Co-deposition of hole-selective contact and absorber for improving the processability of perovskite solar cells. *Nature Energy*, 8:462–472, 2023.

[3] Lucía Fernández. Solar pv-statistics facts, https://www.statista.com/topics/993/solar-pv/topicOverview, 2024.

[4] IEA. Renewables 2023, https://www.iea.org/reports/renewables-2023, 2024.

[5] VDMA. International technology roadmap for photovoltaic (itrpv), https://www.vdma.org/international-technology-roadmap-photovoltaic, 2023.

[6] Ali H. A. Al-Waeli, Hussein A. Kazem, Miqdam Tariq Chaichan, and Kamaruzzaman Sopian. *Introduction*, pages 1–64. Springer International Publishing, Cham, 2019.

[7] Introduction. In J. Theo Kloprogge and Barry J. Wood, editors, *Handbook of Mineral Spectroscopy*, pages xiii–xxv. Elsevier, 2021.

[8] Steven Hegedus and Antonio Luque. *Achievements and Challenges of Solar Electricity from Photovoltaics*, chapter 1, pages 1–38. John Wiley & Sons, Ltd, 2010.

[9] Giles E. Eperon, Maximilian T. Hörantner, and Henry J. Snaith. Metal halide perovskite tandem and multiple-junction photovoltaics. *Nature Reviews Chemistry*, 1(12), Nov 2017.

[10] Louise C. Hirst and Nicholas J. Ekins-Daukes. Fundamental losses in solar cells. *Progress in Photovoltaics: Research and Applications*, 19(3):286–293, 2011.

[11] Ao Wang and Yimin Xuan. A detailed study on loss processes in solar cells. *Energy*, 144:490–500, 2018.

[12] Olivier Dupré, Rodolphe Vaillon, and Martin A. Green. A full thermal model for photovoltaic devices. *Solar Energy*, 140:73–82, 2016.

[13] William Shockley and Hans J. Queisser. Detailed Balance Limit of Efficiency of p-n Junction Solar Cells. *Journal of Applied Physics*, 32(3):510–519, 1961.

[14] Armin Richter, Martin Hermle, and Stefan W. Glunz. Reassessment of the limiting efficiency for crystalline silicon solar cells. *IEEE Journal of Photovoltaics*, 3(4):1184–1191, 2013.

[15] ASTM. Astm international, https://www.astm.org/, 2024.

[16] Yanyun Zhang, Peng Xue, Yifan Zhao, Qianqian Zhang, Gongxun Bai, Jinqing Peng, and Bojia Li. Spectra measurement and clustering analysis of global horizontal irradiance for solar energy application. *Renewable Energy*, 222:119813, 2024.

[17] Sven Rühle. Tabulated values of the shockley–queisser limit for single junction solar cells. *Solar Energy*, 130:139–147, 2016.

[18] Andrew S Brown and Martin A Green. Detailed balance limit for the series constrained two terminal tandem solar cell. *Physica E: Low-dimensional Systems and Nanostructures*, 14(1):96–100, 2002.

[19] L. M. Peter. Towards sustainable photovoltaics: the search for new materials. *Philosophical Transactions of the Royal Society A: Mathematical, Physical and Engineering Sciences*, 369(1942):1840–1856, 2011.

[20] W. Ruppel and P. Wurfel. Upper limit for the conversion of solar energy. *IEEE Transactions on Electron Devices*, 27(4):877–882, 1980.

[21] Thomas Kirchartz and Uwe Rau. Detailed balance and reciprocity in solar cells. *physica status solidi (a)*, 205(12):2737–2751, 2008.

[22] Michael Y. Levy and Christiana Honsberg. Rapid and precise calculations of energy and particle flux for detailed-balance photovoltaic applications. *Solid-State Electronics*, 50(7):1400–1405, 2006.

[23] O. M. ten Kate, M. de Jong, H. T. Hintzen, and E. van der Kolk. Efficiency enhancement calculations of state-of-the-art solar cells by luminescent layers with spectral shifting, quantum cutting, and quantum tripling function. *Journal of Applied Physics*, 114(8):084502, Aug 2013.

[24] C.P. Thomas, A.B. Wedding, and S.O. Martin. Theoretical enhancement of solar cell efficiency by the application of an ideal 'down-shifting' thin film. *Solar Energy Materials and Solar Cells*, 98:455–464, 2012.

[25] Justyna Pastuszak and Paweł Węgierek. Photovoltaic cell generations and current research directions for their development. *Materials*, 15(16), 2022.

[26] Warwick. Iii-v compound semiconductors, http://tinyurl.com/26ay7me4, 2010.

[27] Adolf Goetzberger, Christopher Hebling, and Hans-Werner Schock. Photovoltaic materials, history, status and outlook. *Materials Science and Engineering: R: Reports*, 40(1):1–46, 2003.

[28] D. M. Chapin, C. S. Fuller, and G. L. Pearson. A New Silicon p-n Junction Photocell for Converting Solar Radiation into Electrical Power. *Journal of Applied Physics*, 25(5):676–677, May 1954.

[29] NREL. Best research-cell efficiencies - crystalline silicon cells, https://www.nrel.gov/pv/assets/images/cell-pv-eff-crysi.jpg, 2024.

[30] Longi. Longi sets a new world record of 27.09% for the efficiency of silicon heterojunction back-contact (hbc) solar cells, http://tinyurl.com/2rtrdytt, 2023.

[31] Sidra Khatoon, Satish Kumar Yadav, Vishwadeep Chakravorty, Jyotsna Singh, Rajendra Bahadur Singh, Md Saquib Hasnain, and S.M. Mozammil Hasnain. Perovskite solar cell's efficiency, stability and scalability: A review. *Materials Science for Energy Technologies*, 6:437–459, 2023.

[32] Fraunhofer Institute for Solar Energy Systems. Photovoltaics report, https://www.ise.fraunhofer.de/en/publications/studies/photovoltaics-report.html, 2023.

[33] NREL. Best research-cell efficiencies-thin films, https://www.nrel.gov/pv/assets/images/cell-pv-eff-thinfilm.jpg, 2024.

[34] Kiselman K. Donzel-Gargand O. et al. Keller, J. High-concentration silver alloying and steep back-contact gallium grading enabling copper indium gallium selenide solar cell with 23.6% efficiency. *Nature Energy*, 2024.

[35] Hitoshi Sai, Takuya Matsui, and Koji Matsubara. Stabilized 14.0% -efficient triple-junction thin-film silicon solar cell. *Applied Physics Letters*, 109(18):183506, Nov 2016.

[36] Harald Hoppe and Niyazi Serdar Sariciftci. Organic solar cells: An overview. *Journal of Materials Research*, 19(7):1924–1945, 2004.

[37] NREL. Best research-cell efficiencies - emerging pv, https://www.nrel.gov/pv/assets/images/cell-pv-eff-emergingpv.jpg, 2024.

[38] Lei Zhu, Ming Zhang, Jinqiu Xu, Chao Li, Jun Yan, Guanqing Zhou, Wenkai Zhong, Tianyu Hao, Jiali Song, Xiaonan Xue, and et al. Single-junction organic solar cells with over 19% efficiency enabled by a refined double-fibril network morphology. *Nature Materials*, 21(6):656–663, May 2022.

[39] Havid Aqoma Khoiruddin, Sang-Hak Lee, Imil Imran, Jin-Ha Hwang, Su-Ho Lee, and Sung-Yeon Jang. Alkyl ammonium iodide-based ligand exchange strategy for high-efficiency organic-cation perovskite quantum dot solar cells. *Nature Energy*, pages 1–9, Jan 2024.

[40] Simon Mathew, Aswani Yella, Peng Gao, Robin Humphry-Baker, Basile F. Curchod, Negar Ashari-Astani, Ivano Tavernelli, Ursula Rothlisberger, Md. Khaja Nazeeruddin, and Michael Grätzel. Dye-sensitized solar cells with 13% efficiency achieved through the molecular engineering of porphyrin sensitizers. *Nature Chemistry*, 6(3):242–247, Feb 2014.

[41] A De Vos. Detailed balance limit of the efficiency of tandem solar cells. *Journal of Physics D: Applied Physics*, 13(5):839, May 1980.

[42] NREL. Best research-cell efficiencies - multijunction cells, https://www.nrel.gov/pv/assets/images/cell-pv-eff-mjcells.jpg, 2024.

[43] Patrick Schygulla, Paul Beutel, Stefan Heckelmann, Oliver Höhn, Malte Klitzke, Jonas Schön, Eduard Oliva, Felix Predan, Michael Schachtner, Gerald Siefer, and et al. Quadruple junction solar cell with 47.6% conversion efficiency under concentration, 2022.

[44] Congcong Wu, Kai Wang, Munkhbayar Batmunkh, Abdulaziz S.R. Bati, Dong Yang, Yuanyuan Jiang, Yuchen Hou, Joseph G. Shapter, and Shashank Priya. Multifunctional nanostructured materials for next generation photovoltaics. *Nano Energy*, 70:104480, 2020.

[45] NREL. Best research-cell efficiency chart, https://www.nrel.gov/pv/cell-efficiency.html, 2024.

[46] Akihiro Kojima, Kenjiro Teshima, Yasuo Shirai, and Tsutomu Miyasaka. Organometal halide perovskites as visible-light sensitizers for photovoltaic cells. *Journal of the American Chemical Society*, 131(17):6050–6051, 2009. PMID: 19366264.

[47] Zheng Liang, Yong Zhang, Huifen Xu, Wenjing Chen, Boyuan Liu, Jiyao Zhang, Hui Zhang, Zihan Wang, Dong-Ho Kang, Jianrong Zeng, and et al. Homogenizing

out-of-plane cation composition in perovskite solar cells. *Nature*, 624(7992):557–563, Nov 2023.

[48] Zhengqi Shi and Ahalapitiya H. Jayatissa. Perovskites-based solar cells: A review of recent progress, materials and processing methods. *Materials*, 11(5), 2018.

[49] C. R. Osterwald and T. J. McMahon. History of accelerated and qualification testing of terrestrial photovoltaic modules: A literature review. *Progress in Photovoltaics: Research and Applications*, 17(1):11–33, 2009.

[50] Quinten A. Akkerman and Liberato Manna. What defines a halide perovskite? *ACS Energy Letters*, 5(2):604–610, 2020. PMID: 33344766.

[51] V. M. Goldschmidt. Die gesetze der krystallochemie. *Die Naturwissenschaften*, 14(21):477–485, May 1926.

[52] Zhen Li, Mengjin Yang, Ji-Sang Park, Su-Huai Wei, Joseph J. Berry, and Kai Zhu. Stabilizing perovskite structures by tuning tolerance factor: Formation of formamidinium and cesium lead iodide solid-state alloys. *Chemistry of Materials*, 28(1):284–292, 2016.

[53] Chonghea Li, Xionggang Lu, Weizhong Ding, Liming Feng, Yonghui Gao, and Ziming Guo. Formability of abx3 (x = f, cl, br, i) halide perovskites. *Acta Crystallographica Section B*, 64(6):702–707, 2008.

[54] Qi Chen, Nicholas De Marco, Yang (Michael) Yang, Tze-Bin Song, Chun-Chao Chen, Hongxiang Zhao, Ziruo Hong, Huanping Zhou, and Yang Yang. Under the spotlight: The organic–inorganic hybrid halide perovskite for optoelectronic applications. *Nano Today*, 10(3):355–396, 2015.

[55] Mohammed Istafaul, Haque Ansari, Ahsanulhaq Qurashi, Mohammad Nazeeruddin, and Md Nazeeruddin. Frontiers, opportunities, and challenges in perovskite solar cells: A critical review. *Journal of Photochemistry and Photobiology C: Photochemistry Reviews*, 35:1–24, June 2018.

[56] Feng Hao, Constantinos C. Stoumpos, Robert P. H. Chang, and Mercouri G. Kanatzidis. Anomalous band gap behavior in mixed sn and pb perovskites enables broadening of absorption spectrum in solar cells. *Journal of the American Chemical Society*, 136(22):8094–8099, 2014. PMID: 24823301.

[57] Huanping Zhou, Qi Chen, Gang Li, Song Luo, Tze bing Song, Hsin-Sheng Duan, Ziruo Hong, Jingbi You, Yongsheng Liu, and Yang Yang. Interface engineering of highly efficient perovskite solar cells. *Science*, 345(6196):542–546, 2014.

[58] Haveen Ahmed Mustafa and Dler Adil Jameel. Modeling and the main stages of spin coating process: A review. *Journal of Applied Science and Technology Trends*, 2(03):91 – 95, Aug. 2021.

[59] Anastasia Soultati, Marinos Tountas, Konstantina K. Armadorou, Abd. Rashid bin Mohd Yusoff, Maria Vasilopoulou, and Mohammad Khaja Nazeeruddin. Synthetic approaches for perovskite thin films and single-crystals. *Energy Adv.*, 2:1075–1115, 2023.

[60] Yue Yu, Fu Zhang, Tian Hou, Xiaoran Sun, Hua Yu, and Meng Zhang. A review on gas-quenching technique for efficient perovskite solar cells. *Solar RRL*, 5(10):2100386.

[61] Quentin Guesnay, Florent Sahli, Christophe Ballif, and Quentin Jeangros. Vapor deposition of metal halide perovskite thin films: Process control strategies to shape layer properties. *APL Materials*, 9(10):100703, Oct 2021.

[62] Tze-Bin Song, Qi Chen, Huanping Zhou, Chengyang Jiang, Hsin-Hua Wang, Yang (Michael) Yang, Yongsheng Liu, Jingbi You, and Yang Yang. Perovskite solar cells: film formation and properties. *J. Mater. Chem. A*, 3:9032–9050, 2015.

[63] Junfeng Yan and Brian R. Saunders. Third-generation solar cells: a review and comparison of polymer:fullerene, hybrid polymer and perovskite solar cells. *RSC Adv.*, 4:43286–43314, 2014.

[64] Michael Saliba, Juan-Pablo Correa-Baena, Christian M. Wolff, Martin Stolterfoht, Nga Phung, Steve Albrecht, Dieter Neher, and Antonio Abate. How to make over 20% efficient perovskite solar cells in regular (n–i–p) and inverted (p–i–n) architectures. *Chemistry of Materials*, 30(13):4193–4201, 2018.

[65] Jin-Wook Lee, Sang-Hoon Bae, Nicholas De Marco, Yao-Tsung Hsieh, Zhenghong Dai, and Yang Yang. The role of grain boundaries in perovskite solar cells. *Materials Today Energy*, 7:149–160, 2018.

[66] Handong Jin, Elke Debroye, Masoumeh Keshavarz, Ivan G. Scheblykin, Maarten B. J. Roeffaers, Johan Hofkens, and Julian A. Steele. It's a trap! on the nature of localised states and charge trapping in lead halide perovskites. *Mater. Horiz.*, 7:397–410, 2020.

[67] Xin Mao, Lei Sun, Tao Wu, Tianshu Chu, Weiqiao Deng, and Keli Han. First-principles screening of all-inorganic lead-free abx3 perovskites. *The Journal of Physical Chemistry C*, 122(14):7670–7675, 2018.

[68] Yolla Sukma Handayani, Efi Dwi Indari, Rahmat Hidayat, Yoshiyuki Othsubo, and Shin ichi Kimura. Understanding the role of organic cations on the electronic structure of lead iodide perovskite from their uv photoemission spectra and their electronic structures calculated by dft method. *Materials Research Express*, 6(8):084009, May 2019.

[69] Yasemin Kutes, Yuanyuan Zhou, James L. Bosse, James Steffes, Nitin P. Padture, and Bryan D. Huey. Mapping the photoresponse of ch3nh3pbi3 hybrid perovskite thin films at the nanoscale. *Nano Letters*, 16(6):3434–3441, 2016. PMID: 27116651.

[70] Rahmat Hidayat, Adhita Asma Nurunnizar, Alvin Fariz, Herman, Erlyta Septa Rosa, Shobih, Tomohisa Oizumi, Akihiko Fujii, and Masanori Ozaki. Revealing the charge carrier kinetics in perovskite solar cells affected by mesoscopic structures and defect states from simple transient photovoltage measurements. *Scientific reports*, 10:19197, 2020.

[71] Saba Ahmad, Iffat Ashraf, Muhammad Adil Mansoor, Syed Rizwan, and Mudassir Iqbal. An overview of recent advances in the synthesis and applications of the transition metal carbide nanomaterials. *Nanomaterials*, 11(3), 2021.

[72] Shenghao Wang, Takeaki Sakurai, Weijia Wen, and Yabing Qi. Energy level alignment at interfaces in metal halide perovskite solar cells. *Advanced Materials Interfaces*, 5(22):1800260, 2018.

[73] Pengjun Zhao, Byeong Jo Kim, and Hyun Suk Jung. Passivation in perovskite solar cells: A review. *Materials Today Energy*, 7:267–286, 2018.

[74] Lei Meng, Jingbi You, and Yang Yang. Addressing the stability issue of perovskite solar cells for commercial applications. *Nature Communications*, 9:5265, 2018.

[75] Dictionary.com. Hygroscopic https://www.dictionary.com/browse/hygroscopic, 2024.

[76] Yuanyuan Zhou, Laura M. Herz, Alex K-Y. Jen, and Michael Saliba. Advances and challenges in understanding the microscopic structure–property–performance relationship in perovskite solar cells. *Nature Energy*, 7(9):794–807, Sep 2022.

[77] Rui Wang, Muhammad Mujahid, Yu Duan, Zhao-Kui Wang, Jingjing Xue, and Yang Yang. A review of perovskites solar cell stability. *Advanced Functional Materials*, 29(47):1808843, 2019.

[78] R A Goyer. Lead toxicity: current concerns. *Environmental Health Perspectives*, 100:177–187, 1993.

[79] Zhen Li, Talysa R. Klein, Dong Hoe Kim, Mengjin Yang, Joseph J. Berry, Maikel F. van Hest, and Kai Zhu. Scalable fabrication of perovskite solar cells. *Nature Reviews Materials*, 3(4), Mar 2018.

[80] Y. Pauleau. *Physical Vapor Deposition Techniques I: Evaporation and Sputtering*, pages 135–179. Springer Netherlands, Dordrecht, 1992.

[81] Tingting Niu, Lingfeng Chao, Xue Dong, Li Fu, and Yonghua Chen. Phase-pure -fapbi3 for perovskite solar cells. *The Journal of Physical Chemistry Letters*, 13(7):1845–1854, 2022. PMID: 35175056.

[82] Dawei Tan, Xuejing Zhang, Xiao Liu, Hongmei Zhang, and Dongge Ma. Stability enhancement of inverted perovskite solar cells using lif in electron transport layer. *Organic Electronics*, 80:105613, 2020.

[83] Chuanliang Chen, Shasha Zhang, Shaohang Wu, Wenjun Zhang, Hongmei Zhu, Zhenzhong Xiong, Yanjun Zhang, and Wei Chen. Effect of bcp buffer layer on eliminating charge accumulation for high performance of inverted perovskite solar cells. *RSC Adv.*, 7:35819–35826, 2017.

[84] Christiana Honsberg and Stuart Bowden. Pv education, https://www.pveducation.org/pvcdrom/solar-cell-operation/iv-curve.

[85] Mark V. Khenkin, Eugene A. Katz, Antonio Abate, and et al. Consensus statement for stability assessment and reporting for perovskite photovoltaics based on isos procedures. *Nature Energy*, 5:35–49, 2020.

[86] Wisnu Ananda. External quantum efficiency measurement of solar cell. In *2017 15th International Conference on Quality in Research (QiR) : International Symposium on Electrical and Computer Engineering*, pages 450–456, 2017.

[87] Chapter 3 - the current situation in ultra-precision technology – silicon single crystals as an example. In Toshiro Doi, Ioan D. Marinescu, and Syuhei Kurokawa, editors, *Advances in CMP Polishing Technologies*, pages 15–111. William Andrew Publishing, Oxford, 2012.

[88] Roman Anufriev. Optical properties of inas/inp nanowire heterostructures. 2013.

[89] Michael B. Johnston and Laura M. Herz. Hybrid perovskites for photovoltaics: Charge-carrier recombination, diffusion, and radiative efficiencies. *Accounts of Chemical Research*, 49(1):146–154, 2016. PMID: 26653572.

[90] Ahmer Baloch, Fahhad Alharbi, Giulia Grancini, Mohammad Hossain, Mohammad

Nazeeruddin, and Nouar Tabet. Analysis of photocarrier dynamics at interfaces in perovskite solar cells by time resolved photoluminescence. *The Journal of Physical Chemistry C*, 122:26805, Nov 2018.

[91] Kuan Liu, Qiong Liang, Minchao Qin, Dong Shen, Hang Yin, Zhiwei Ren, Yaokang Zhang, Hengkai Zhang, Patrick W.K. Fong, Zehan Wu, Jiaming Huang, Jianhua Hao, Zijian Zheng, Shu Kong So, Chun-Sing Lee, Xinhui Lu, and Gang Li. Zwitterionic-surfactant-assisted room-temperature coating of efficient perovskite solar cells. *Joule*, 4(11):2404–2425, 2020.

[92] Ashok K. Singh. Chapter 4 - experimental methodologies for the characterization of nanoparticles. In Ashok K. Singh, editor, *Engineered Nanoparticles*, pages 125–170. Academic Press, Boston, 2016.

[93] B.J. Inkson. Scanning electron microscopy (sem) and transmission electron microscopy (tem) for materials characterization. In Gerhard Hübschen, Iris Altpeter, Ralf Tschuncky, and Hans-Georg Herrmann, editors, *Materials Characterization Using Nondestructive Evaluation (NDE) Methods*, pages 17–43. Woodhead Publishing, 2016.

[94] Emilio Palomares, Núria F. Montcada, María Méndez, Jesús Jiménez-López, Wenxing Yang, and Gerrit Boschloo. Chapter 7 - photovoltage/photocurrent transient techniques. In Meysam Pazoki, Anders Hagfeldt, and Tomas Edvinsson, editors, *Characterization Techniques for Perovskite Solar Cell Materials*, Micro and Nano Technologies, pages 161–180. Elsevier, 2020.

[95] George F. Harrington and José Santiso. Back-to-basics tutorial: X-ray diffraction of thin films. *Journal of Electroceramics*, 47:141–163, 2021.

[96] Fawad Ali, Cristina Roldán-Carmona, Muhammad Sohail, and Mohammad Khaja Nazeeruddin. Applications of self-assembled monolayers for perovskite solar cells interface engineering to address efficiency and stability. *Advanced Energy Materials*, 10(48):2002989, 2020.

[97] Daniel K Schwartz. Mechanisms and kinetics of self-assembled monolayer formation. *Annual Review of Physical Chemistry*, 52(1):107–137, 2001. PMID: 11326061.

[98] Seo Yeon Kim, Soo Jin Cho, Seo Eun Byeon, Xin He, and Hyo Jae Yoon. Self-assembled monolayers as interface engineering nanomaterials in perovskite solar cells. *Advanced Energy Materials*, 10(44):2002606, 2020.

[99] Ross A. Hatton, Martin R. Willis, Michael A. Chesters, Frank J. M. Rutten, and

David Briggs. Enhanced hole injection in organic light-emitting diodes using a sam-derivatised ultra-thin gold anode supported on ito glass. *J. Mater. Chem.*, 13:38–43, 2003.

[100] S. Kobayashi, T. Nishikawa, T. Takenobu, S. Mori, T. Shimoda, T. Mitani, H. Shimotani, N. Yoshimoto, S. Ogawa, and Y. Iwasa. Control of carrier density by self-assembled monolayers in organic field-effect transistors. *Nature Materials*, 3:317–322, 2004.

[101] Bobo Li, Yani Chen, Ziqi Liang, Deqing Gao, and Wei Huang. Interfacial engineering by using self-assembled monolayer in mesoporous perovskite solar cell. *RSC Adv.*, 5:94290–94295, 2015.

[102] Lijian Zuo, Zhuowei Gu, Tao Ye, Weifei Fu, Gang Wu, Hanying Li, and Hongzheng Chen. Enhanced photovoltaic performance of ch3nh3pbi3 perovskite solar cells through interfacial engineering using self-assembling monolayer. *Journal of the American Chemical Society*, 137(7):2674–2679, 2015. PMID: 25650811.

[103] Guang Yang, Changlei Wang, Hongwei Lei, Xiaolu Zheng, Pingli Qin, Liangbin Xiong, Xingzhong Zhao, Yanfa Yan, and Guojia Fang. Interface engineering in planar perovskite solar cells: energy level alignment, perovskite morphology control and high performance achievement. *J. Mater. Chem. A*, 5:1658–1666, 2017.

[104] Meihui Hou, Haijuan Zhang, Ze Wang, Yingdong Xia, Yonghua Chen, and Wei Huang. Enhancing efficiency and stability of perovskite solar cells via a self-assembled dopamine interfacial layer. *ACS Applied Materials & Interfaces*, 10(36):30607–30613, 2018. PMID: 30118201.

[105] Qin Wang, Chu-Chen Chueh, Ting Zhao, Jiaqi Cheng, Morteza Eslamian, Wallace C. H. Choy, and Alex K.-Y. Jen. Effects of self-assembled monolayer modification of nickel oxide nanoparticles layer on the performance and application of inverted perovskite solar cells. *ChemSusChem*, 10(19):3794–3803, 2017.

[106] Guang Yang, Changlei Wang, Hongwei Lei, Xiaolu Zheng, Pingli Qin, Liangbin Xiong, Xingzhong Zhao, Yanfa Yan, and Guojia Fang. Interface engineering in planar perovskite solar cells: energy level alignment, perovskite morphology control and high performance achievement. *J. Mater. Chem. A*, 5:1658–1666, 2017.

[107] Artiom Magomedov, Amran Al-Ashouri, Ernestas Kasparavičius, Simona Strazdaite, Gediminas Niaura, Marko Jošt, Tadas Malinauskas, Steve Albrecht, and Vytautas Getautis. Self-assembled hole transporting monolayer for highly efficient perovskite solar cells. *Advanced Energy Materials*, 8(32):1801892, 2018.

[108] Randi Azmi, Wisnu Tantyo Hadmojo, Septy Sinaga, Chang-Lyoul Lee, Sung Cheol Yoon, In Hwan Jung, and Sung-Yeon Jang. High-efficiency low-temperature zno based perovskite solar cells based on highly polar, nonwetting self-assembled molecular layers. *Advanced Energy Materials*, 8(5):1701683, 2018.

[109] Yang Bai, Haining Chen, Shuang Xiao, Qifan Xue, Teng Zhang, Zonglong Zhu, Qiang Li, Chen Hu, Yun Yang, Zhicheng Hu, Fei Huang, Kam Sing Wong, Hin-Lap Yip, and Shihe Yang. Effects of a molecular monolayer modification of nio nanocrystal layer surfaces on perovskite crystallization and interface contact toward faster hole extraction and higher photovoltaic performance. *Advanced Functional Materials*, 26(17):2950–2958, 2016.

[110] Xiao Liu, Kai-Wei Tsai, Zonglong Zhu, Ye Sun, Chu-Chen Chueh, and Alex K.-Y. Jen. A low-temperature, solution processable tin oxide electron-transporting layer prepared by the dual-fuel combustion method for efficient perovskite solar cells. *Advanced Materials Interfaces*, 3(13):1600122, 2016.

[111] Konrad Wojciechowski, Samuel D. Stranks, Antonio Abate, Golnaz Sadoughi, Aditya Sadhanala, Nikos Kopidakis, Garry Rumbles, Chang-Zhi Li, Richard H. Friend, Alex K.-Y. Jen, and Henry J. Snaith. Heterojunction modification for highly efficient organic–inorganic perovskite solar cells. *ACS Nano*, 8(12):12701–12709, 2014. PMID: 25415931.

[112] Zhiqi Li, Jiaxin Guo, Zhuowei Li, Wenbin Han, Guanhua Ren, Chunyu Liu, Liang Shen, and Wenbin Guo. Incorporating self-assembled silane-crosslinked carbon dots into perovskite solar cells to improve efficiency and stability. *J. Mater. Chem. A*, 8:5629–5637, 2020.

[113] P. Topolovsek, F. Lamberti, T. Gatti, A. Cito, J. M. Ball, E. Menna, C. Gadermaier, and A. Petrozza. Functionalization of transparent conductive oxide electrode for tio2-free perovskite solar cells. *J. Mater. Chem. A*, 5:11882–11893, 2017.

[114] Artiom Magomedov, Amran Al-Ashouri, Ernestas Kasparavičius, Simona Strazdaite, Gediminas Niaura, Marko Jošt, Tadas Malinauskas, Steve Albrecht, and Vytautas Getautis. Self-assembled hole transporting monolayer for highly efficient perovskite solar cells. *Advanced Energy Materials*, 8(32):1801892, 2018.

[115] Songran Wang, Huanxin Guo, and Yongzhen Wu. Advantages and challenges of self-assembled monolayer as a hole-selective contact for perovskite solar cells. *Materials Futures*, 2(1):012105, Mar 2023.

[116] Dilpreet Singh Mann, Pramila Patil, Sung-Nam Kwon, and Seok-In Na. En-

hanced performance of p-i-n perovskite solar cell via defect passivation of nickel oxide/perovskite interface with self-assembled monolayer. *Applied Surface Science*, 560:149973, 2021.

[117] Wikipedia. Carbazole, https://en.wikipedia.org/wiki/Carbazole.

[118] Wikipedia. Alkyl group, https://en.wikipedia.org/wiki/Alkyl_group.

[119] TCI chemicals. Self assemble monolayer forming agent for enhancing solar cell performance, https://www.tcichemicals.com/OP/en/product/topics/hole-selective_self-assembled_monolayer-forming_agents.

[120] Luminescence Technology Corp. Self-assembled monolayers materials, https://www.lumtec.com.tw/products-view.php?ID=9826.

[121] Elena J. Cassella, Emma L. K. Spooner, Timothy Thornber, Mary E. O'Kane, Thomas E. Catley, James E. Bishop, Joel A. Smith, Onkar S. Game, and David G. Lidzey. Gas-assisted spray coating of perovskite solar cells incorporating sprayed self-assembled monolayers (adv. sci. 14/2022). *Advanced Science*, 9(14):2270087, 2022.

[122] Seira Yamaguchi, Atsushi Sato, Kaori Ajiro, Miyuki Shiokawa, Yuya Hashimoto, Takuto Maeda, Mutsumi Sugiyama, Takeshi Gotanda, and Kazuhiro Marumoto. Performance improvement mechanisms of perovskite solar cells by modification of niox hole-selective contacts with self-assembled-monolayers. *Solar Energy Materials and Solar Cells*, 258:112428, 2023.

[123] Qi Chen, Huanping Zhou, Tze-Bin Song, Song Luo, Ziruo Hong, Hsin-Sheng Duan, Letian Dou, Yongsheng Liu, and Yang Yang. Controllable self-induced passivation of hybrid lead iodide perovskites toward high performance solar cells. *Nano Letters*, 14(7):4158–4163, 2014. PMID: 24960309.

[124] Fangzhou Liu, Qi Dong, Man Kwong Wong, Aleksandra B. Djurišić, Annie Ng, Zhiwei Ren, Qian Shen, Charles Surya, Wai Kin Chan, Jian Wang, Alan Man Ching Ng, Changzhong Liao, Hangkong Li, Kaimin Shih, Chengrong Wei, Huimin Su, and Junfeng Dai. Is excess pbi2 beneficial for perovskite solar cell performance? *Advanced Energy Materials*, 6(7):1502206, 2016.

[125] Lei Meng, Chenkai Sun, Rui Wang, Wenchao Huang, Zipeng Zhao, Pengyu Sun, Tianyi Huang, Jingjing Xue, Jin-Wook Lee, Chenhui Zhu, Yu Huang, Yongfang Li, and Yang Yang. Tailored phase conversion under conjugated polymer enables

thermally stable perovskite solar cells with efficiency exceeding 21%. *Journal of the American Chemical Society*, 140(49):17255–17262, 2018. PMID: 30449094.

[126] Randi Azmi, Esma Ugur, Akmaral Seitkhan, Faisal Aljamaan, Anand S. Subbiah, Jiang Liu, George T. Harrison, Mohamad I. Nugraha, Mathan K. Eswaran, Maxime Babics, Yuan Chen, Fuzong Xu, Thomas G. Allen, Atteq ur Rehman, Chien-Lung Wang, Thomas D. Anthopoulos, Udo Schwingenschlögl, Michele De Bastiani, Erkan Aydin, and Stefaan De Wolf. Damp heat–stable perovskite solar cells with tailored-dimensionality 2d/3d heterojunctions. *Science*, 376(6588):73–77, 2022.

[127] Zhou Ning, Yiheng Shen, Yu Zhang, Ziqi Xu, Guanhaojie Zheng, Liang Li, Qi Chen, and Huanping Zhou. Csi pre-intercalation in the inorganic framework for efficient and stable fa 1 x cs x pbi 3 (cl) perovskite solar cells. *Small*, 13:1700484, April 2017.

[128] Qin Wang, Chu-Chen Chueh, Ting Zhao, Jiaqi Cheng, Morteza Eslamian, Wallace C. H. Choy, and Alex K.-Y. Jen. Effects of self-assembled monolayer modification of nickel oxide nanoparticles layer on the performance and application of inverted perovskite solar cells. *ChemSusChem*, 10(19):3794–3803, 2017.

[129] Nan Li, Zonglong Zhu, Chu-Chen Chueh, Hongbin Liu, Bo Peng, Alessio Petrone, Xiaosong Li, Liduo Wang, and Alex K.-Y. Jen. Mixed cation faxpea1–xpbi3 with enhanced phase and ambient stability toward high-performance perovskite solar cells. *Advanced Energy Materials*, 7(1):1601307, 2017.

[130] Haoran Chen, Yuetian Chen, Taiyang Zhang, Xiaomin Liu, Xingtao Wang, and Yixin Zhao. Advances to high-performance black-phase fapbi3 perovskite for efficient and stable photovoltaics. *Small Structures*, 2(5):2000130, 2021.

[131] Fluxim. Characterization techniques for organic and perovskite solar cells,

[132] Jianyou Chen, Jinkui Song, Feihong Huang, Hao Li, Shuangshuang Liu, Mingkui Wang, and Yan Shen. The role of synthesis parameters on crystallization and grain size in hybrid halide perovskite solar cells. *The Journal of Physical Chemistry C*, 121(32):17053–17061, 2017.

[133] Yuze Lin, Liang Shen, Jun Dai, Yehao Deng, Yang Wu, Yang Bai, Xiaopeng Zheng, Jiayu Wang, Yanjun Fang, Haotong Wei, Wei Ma, Xiao Cheng Zeng, Xiaowei Zhan, and Jinsong Huang. -conjugated lewis base: Efficient trap-passivation and charge-extraction for hybrid perovskite solar cells. *Advanced Materials*, 29(7):1604545, 2017.

[134] Min Kim, Silvia G. Motti, Roberto Sorrentino, and Annamaria Petrozza. Enhanced

solar cell stability by hygroscopic polymer passivation of metal halide perovskite thin film. *Energy Environ. Sci.*, 11:2609–2619, 2018.

[135] Alyamani-A.Y. Kubicki-D.J. et al. Alharbi, E.A. Atomic-level passivation mechanism of ammonium salts enabling highly efficient perovskite solar cells. *Nature Communications*, 10:3008, 2019.

[136] Thomas P. Baumeler, Essa A. Alharbi, George Kakavelakis, George C. Fish, Mubarak T. Aldosari, Miqad S. Albishi, Lukas Pfeifer, Brian I. Carlsen, Jun-Ho Yum, Abdullah S. Alharbi, Mounir D. Mensi, Jing Gao, Felix T. Eickemeyer, Kevin Sivula, Jacques-E Moser, Shaik M. Zakeeruddin, and Michael Grätzel. Surface passivation of fapbi3-rich perovskite with cesium iodide outperforms bulk incorporation. *ACS Energy Letters*, 8(5):2456–2462, 2023.

[137] Alan R. Katritzky, Dan C. Fara, Hongfang Yang, Kaido Tämm, Tarmo Tamm, and Mati Karelson. Quantitative measures of solvent polarity. *Chemical Reviews*, 104(1):175–198, 2004. PMID: 14719974.

[138] The Ohio State University. Polarity of solvents, https://research.cbc.osu.edu/turro.1/wp-content/uploads/2017/02/PolarityofSolvents.pdf.

[139] Xueqing Zheng, Tingming Jiang, Lizhong Bai, Xu Chen, Zeng Chen, Xuehui Xu, Dongdong Song, Xiaojian Xu, Bo Li, and Yang (Michael) Yang. Enhanced thermal stability of inverted perovskite solar cells by interface modification and additive strategy. *RSC Adv.*, 10:18400–18406, 2020.

[140] ESA. Blackbody radiation, https://sci.esa.int/web/education/-/48986-blackbody-radiation, 2024.

[141] AMOLF. Detailed balance (db) charts, https://www.lmpv.nl/db/, 2023.

[142] Albert Polman, Mark Knight, Erik C. Garnett, Bruno Ehrler, and Wim C. Sinke. Photovoltaic materials: Present efficiencies and future challenges. *Science*, 352(6283):aad4424, 2016.

Supplementary Information

Chapter 1: introduction

1: Working principle and losses

Notes for figure S1a:

- **BB6000K** stands for "black body with a surface temperature of 6000K", where a black body is "a theoretical object that completely absorbs all of the light that it receives and reflects none" [140];
- Defined by ASTM [15, 16], **AM1.5D**, **AM1.5G** and **AM0** are terrestrial spectral irradiance distributions, direct normal, hemispherical on 37° tilted surface, and just outside the earths atmosphere, respectively.

Note for figure S1b: **DB** limit stands for "detailed balance limit", i.e. Shockley-Queisser limit.

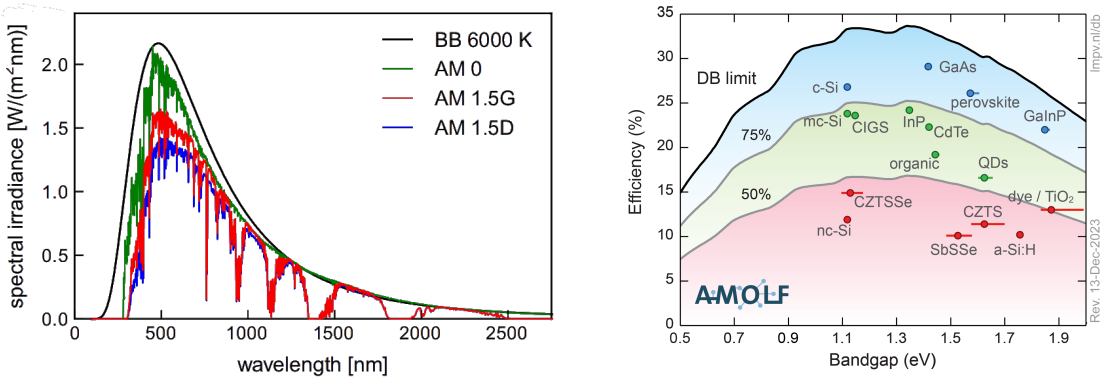

(a) (b)

Figure S1: (a) Solar spectrum according to ASTM G173-03 compared to the spectrum used by Shockley and Queisser of a black body with a surface temperature of 6000 K, reproduced with permission from [17], and (b) fraction of the Shockley-Queisser limit (black line) achieved by record-efficiency cells, gray lines showing 75% and 50% of the limit, updated to December 2023, reproduced with permission from [141, 142].

1.1: PSCs challenges

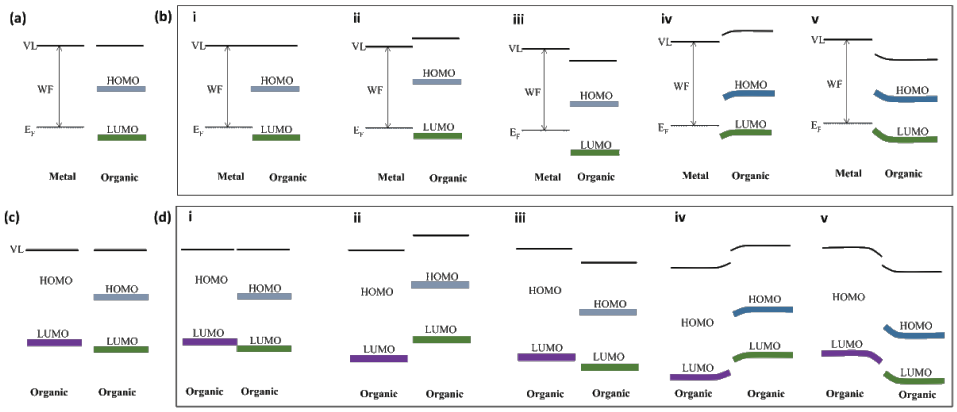

Figure S2: a) Energy levels of metal and organic material before contact. b) Various cases of energy level diagrams of metal/organic interface after contact ((i) vacuum level alignment; (ii and iii) dipole layer formation; (iv and v) occurrence of band bending). c) Energy levels of organic and organic materials before contact. d) Various cases of energy level diagrams of organic/organic interface after contact (i, vacuum level alignment; ii and iii, dipole layer formation; iv and v, occurrence of band bending). Reproduced with permission from [72].

Chapter 2: fabrication and characterization

2.2 Reference cell

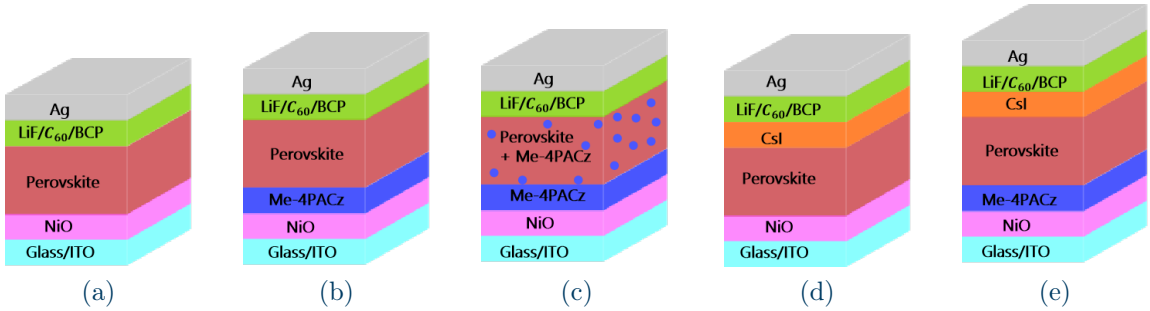

Figure S3: Structures of the (a) reference, (b) *bottom interface*, (c) *Me-4PACz treated*, (d) *reference + CsI* and (e) *bottom interface + CsI* cells.

Layer	Material	Deposition	Thickness/ Concentration
HTL	Nickel oxide	DC sputtering	15 nm
Perovskite	Lead iodide	Thermal evaporation	200nm
	Organic solution	Spin coating and annealing	0.43M
ETL	Lithium fluoride	Thermal evaporation	0.8nm
	Carbon 60	Thermal evaporation	30nm
	Bathocuproine	Thermal evaporation	5nm
Metal	Silver or Copper	Thermal evaporation	100nm

Table S1: Reference cell.

2.3.2 Thermal stability test

Layer	Material	Deposition	Thickness/ Concentration
HTL	Nickel oxide	DC sputtering	15 nm
Perovskite	Lead iodide	Thermal evaporation	200nm
	Organic solution	Spin coating and annealing	0.43M
ETL	Lithium fluoride	Thermal evaporation	0.8nm
	Carbon 60	Thermal evaporation	30nm
	Bathocuproine	Thermal evaporation	5nm
Additional layer	ITO	DC sputtering	70nm
Metal	Silver	Thermal evaporation	100nm

Table S2: Reference cell used for the thermal stability test.

Chapter 3: bottom layer modifications

3.2.3 Optimal concentration of perovskite

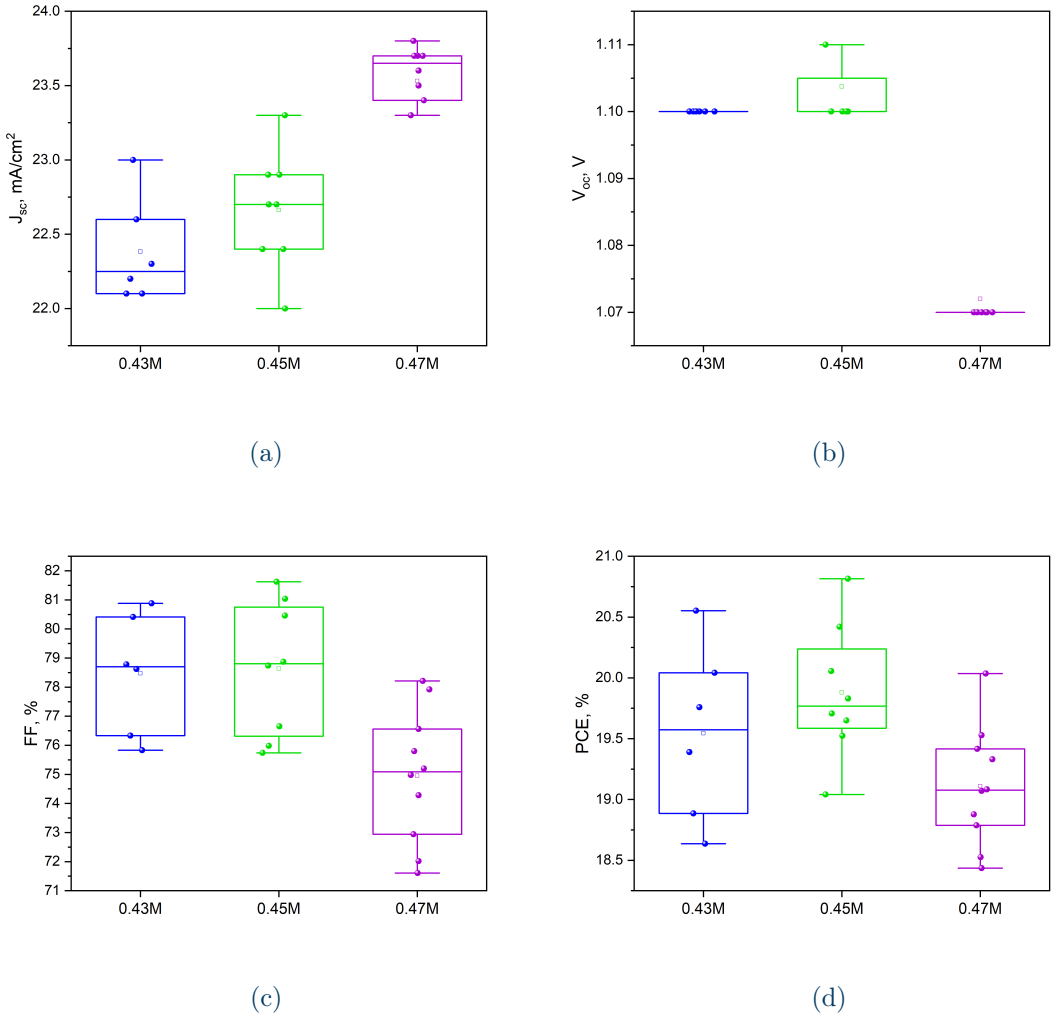

Figure S4: Statistics on (a) J_{sc}, (b) V_{oc}, (c) FF, (d) PCE of cells: Me-4PACz on top of NiOx and higher concentrations of the organic solution of the perovskite.

Layer	Material	Deposition	Thickness/ Concentration
HTL	Nickel oxide	DC sputtering	15 nm
Additional layer	Me-4PACz	Spin coating and rinsing	0.33mg/ml
Perovskite	Lead iodide	Thermal evaporation	200nm
	Organic solution	Spin coating and annealing	0.43M
ETL	Lithium fluoride	Thermal evaporation	0.8nm
	Carbon 60	Thermal evaporation	30nm
	Bathocuproine	Thermal evaporation	5nm
Metal	Silver	Thermal evaporation	100nm

Table S3: *Bottom interface* cell.

3.3.2 Photoluminescence

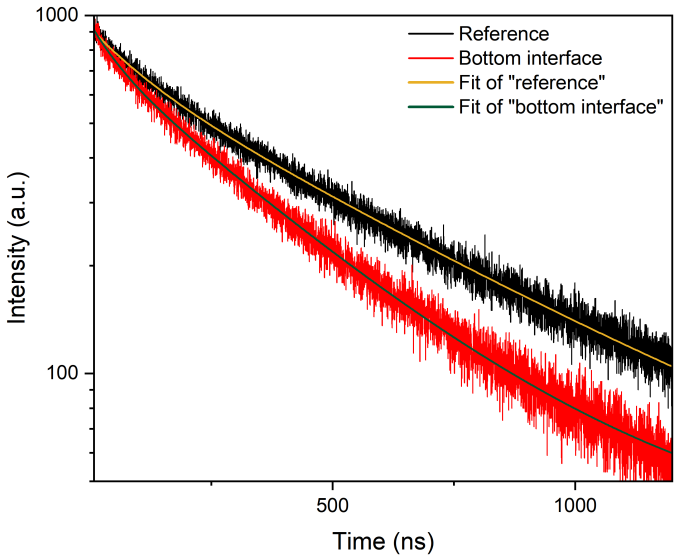

Figure S5: Time-resolved photoluminescence of reference and *bottom interface* cells.

	Reference	bottom interface
A_1	150.48 ± 4.88	179.99 ± 4.22
τ_1	(73.52 ± 4.37) ns	(58.38 ± 2.52)ns
A_2	743.19 ± 3.95	739.02 ± 3.90
τ_2	(488.86 ± 6.32) ns	(362.50 ± 3.0) ns

Table S4: Parameters of the TRPL exponential fit for reference and *bottom interface* cells.

3.3.5 X-ray diffraction

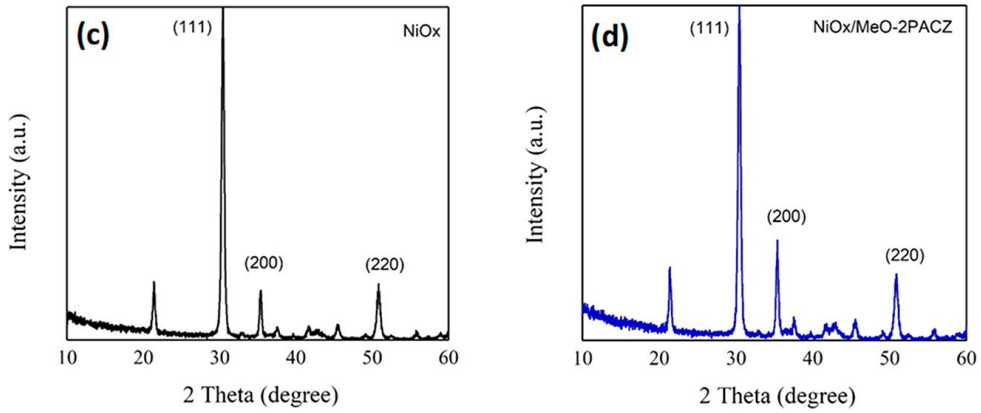

Figure S6: (c) XRD patterns for NiOx and (d) XRD patterns for NiOx/MeO-2PACz SAM, reproduced with permission from [1].

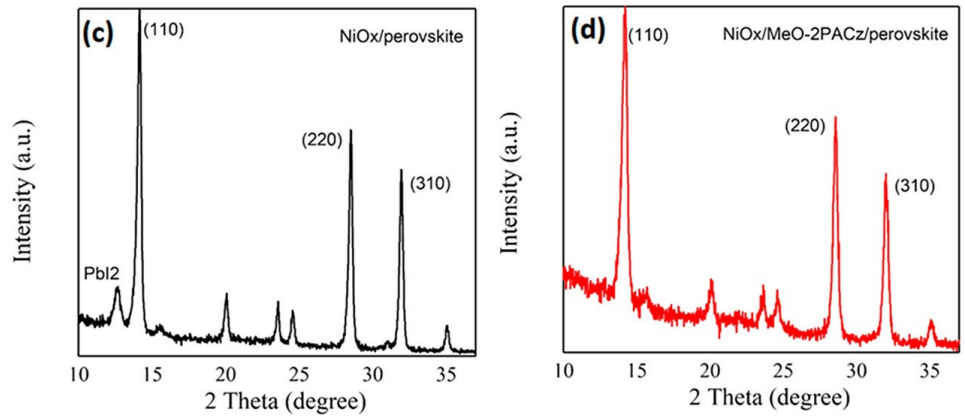

Figure S7: (c) XRD patterns for perovskite films on pristine NiOx and (d) XRD for modified NiOx, reproduced with permission from [1].

	Reference	Bottom interface	Me-4PACz treated	Reference + CsI	Bottom interface + CsI
13.98°	0.168	0.163	0.162	0.167	0.167
28.3°	0.185	0.185	0.189	0.188	0.181

Table S5: FWHM of the peaks of the XRD data of all cells

Chapter 4: bulk modifications

4.2 Electrical results

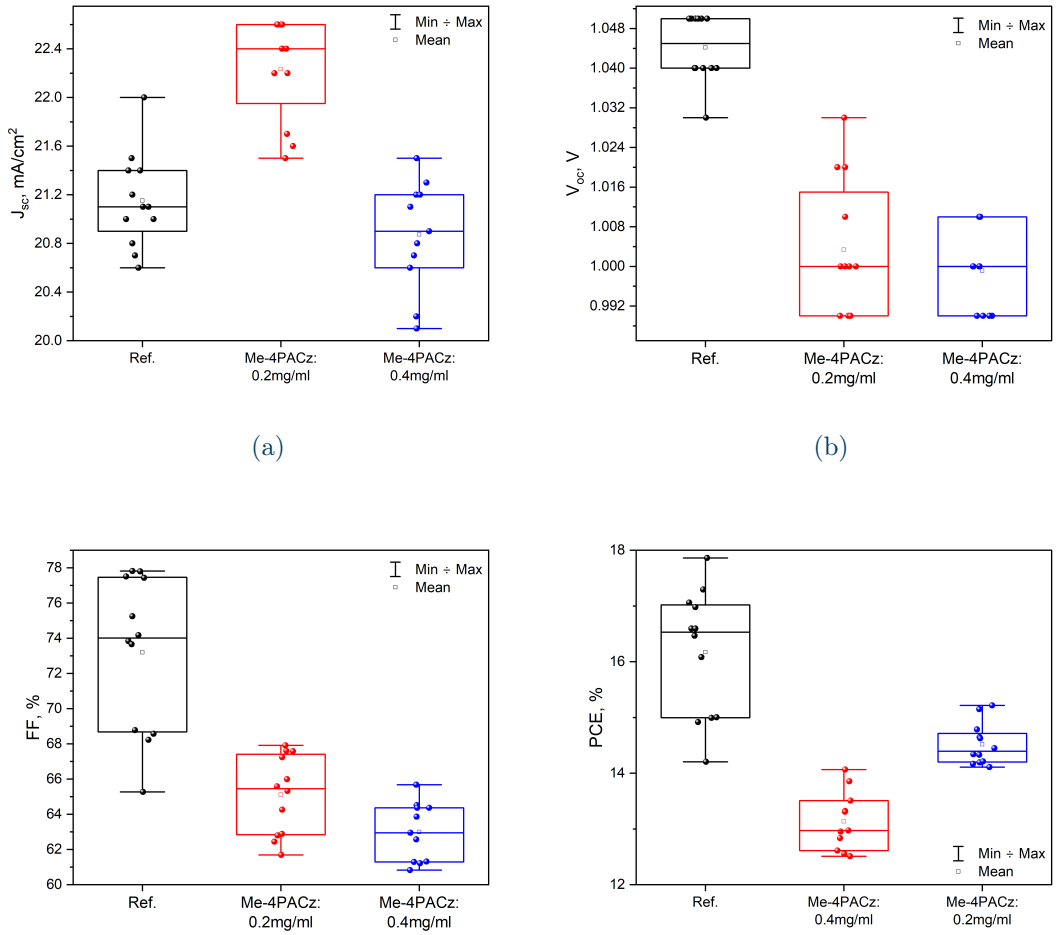

Figure S8: Statistics on (a) J_{sc}, (b) V_{oc}, (c) FF, (d) PCE of cells: reference and higher concentrations of Me-4PACz in the perovskite precursor solution.

4.3 Characterizations and tests

Layer	Material	Deposition	Thickness/ Concentration
HTL	Nickel oxide	DC sputtering	15 nm
Additional layer	Me-4PACz	Spin coating and rinsing	0.33mg/ml
Perovskite	Lead iodide	Thermal evaporation	200nm
	Organic solution	Spin coating and annealing	0.43M
	+ Me-4PACz		+0.1mg/ml
ETL	Lithium fluoride	Thermal evaporation	0.8nm
	Carbon 60	Thermal evaporation	30nm
	Bathocuproine	Thermal evaporation	5nm
Metal	Silver	Thermal evaporation	100nm

Table S6: *Me-4PACz treated* cell.

4.3.2 Photoluminescence

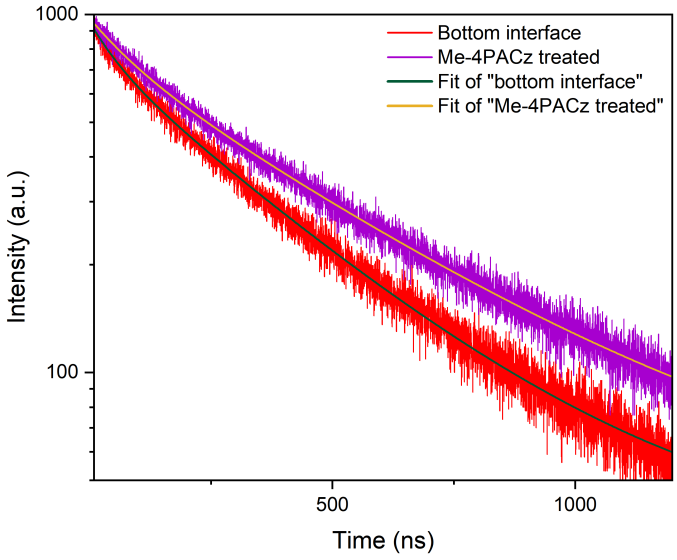

Figure S9: Time-resolved photoluminescence of *bottom interface* and *Me-4PAcz treated* cells, alongside their biexponential fit.

	Bottom interface	Me-4PACz treated
A_1	179.99 ± 4.22	188.07 ± 8.16
τ_1	(58.38 ± 2.52)ns	(92.76 ± 4.86) ns
A_2	739.02 ± 3.90	747.58 ± 6.97
τ_2	(362.50 ± 3.0) ns	(470.10 ± 7.77) ns

Table S7: Parameters of the TRPL exponential fit for *bottom interface* and *Me-4PACz treated* cells.

4.3.3 X-ray diffraction

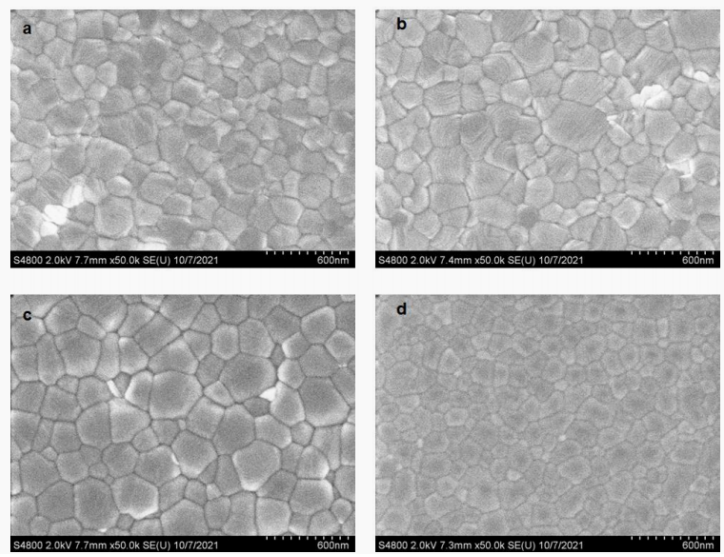

Figure S10: SEM images of (a) neat perovskite film, (b) perovskite film processed with 0.5 mg/mL Me-4PACz in precursor, (c) perovskite film processed with 1 mg/mL Me-4PACz concentrations in precursor, and (d) perovskite film processed with 2 mg/mL Me-4PACz in precursor, reproduced with permission from [2].

Chapter 5: top layer modifications

5.2 The solubility issue

Solvent(s)	Concentration	Solubility
IPA	1mg/ml	Not dissolved
Ethanol	2.5mg/ml	Dissolved
Ethanol	5mg/ml	Not dissolved
Methanol	2.5mg/ml	Dissolved
Methanol	5mg/ml	Dissolved
33% IPA 66% ethanol	2.5mg/ml	Dissolved
66% IPA 33% ethanol	2.5 mg/ml	Not (entirely) dissolved

Table S8: Results of different solvents used to dissolve CsI.

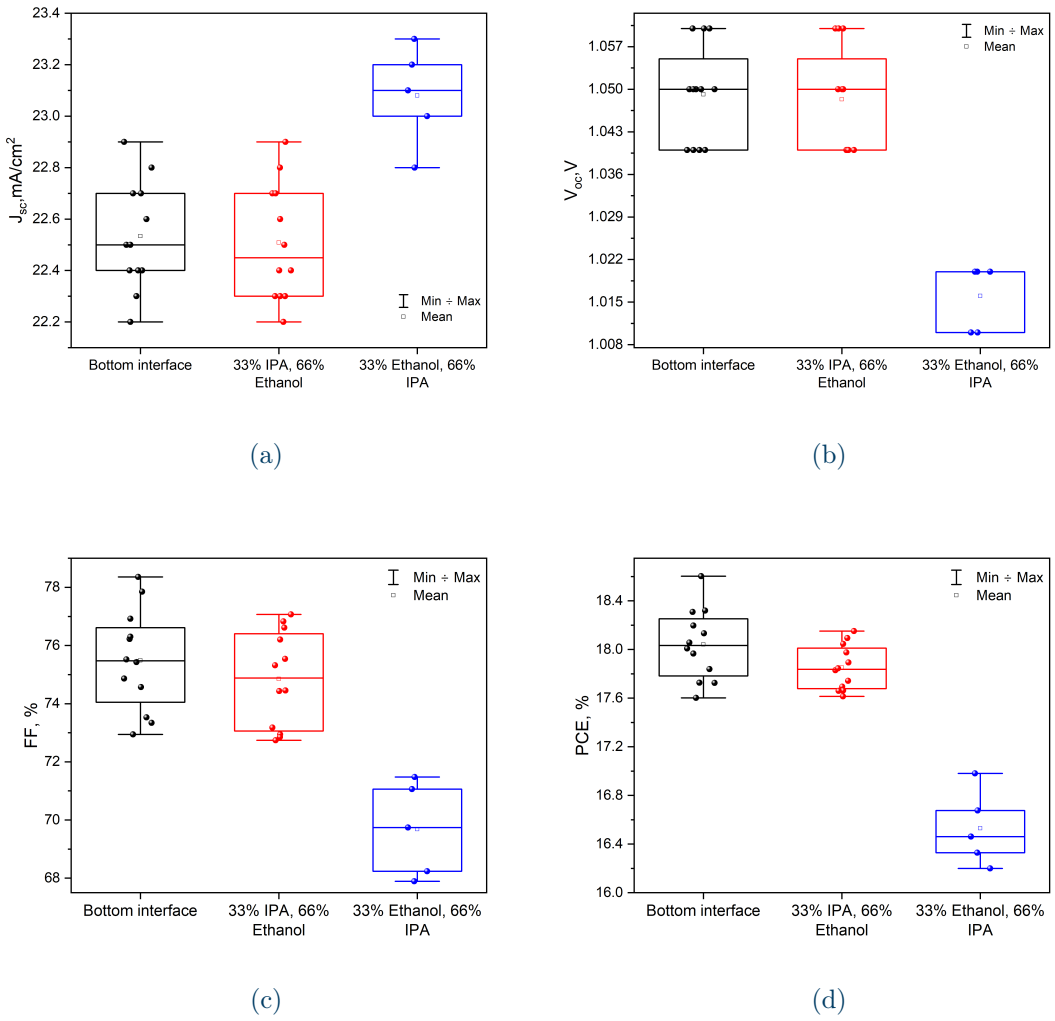

Figure S11: Statistics on (a) J_{sc}, (b) V_{oc}, (c) FF, (d) PCE of cells: *bottom interface* and different percentages of IPA and ethanol on top of the perovskite surface. These results prove again the correlation between polarity of the solvent and worsening of the performance.

5.3 Use of a protection layer for the perovskite

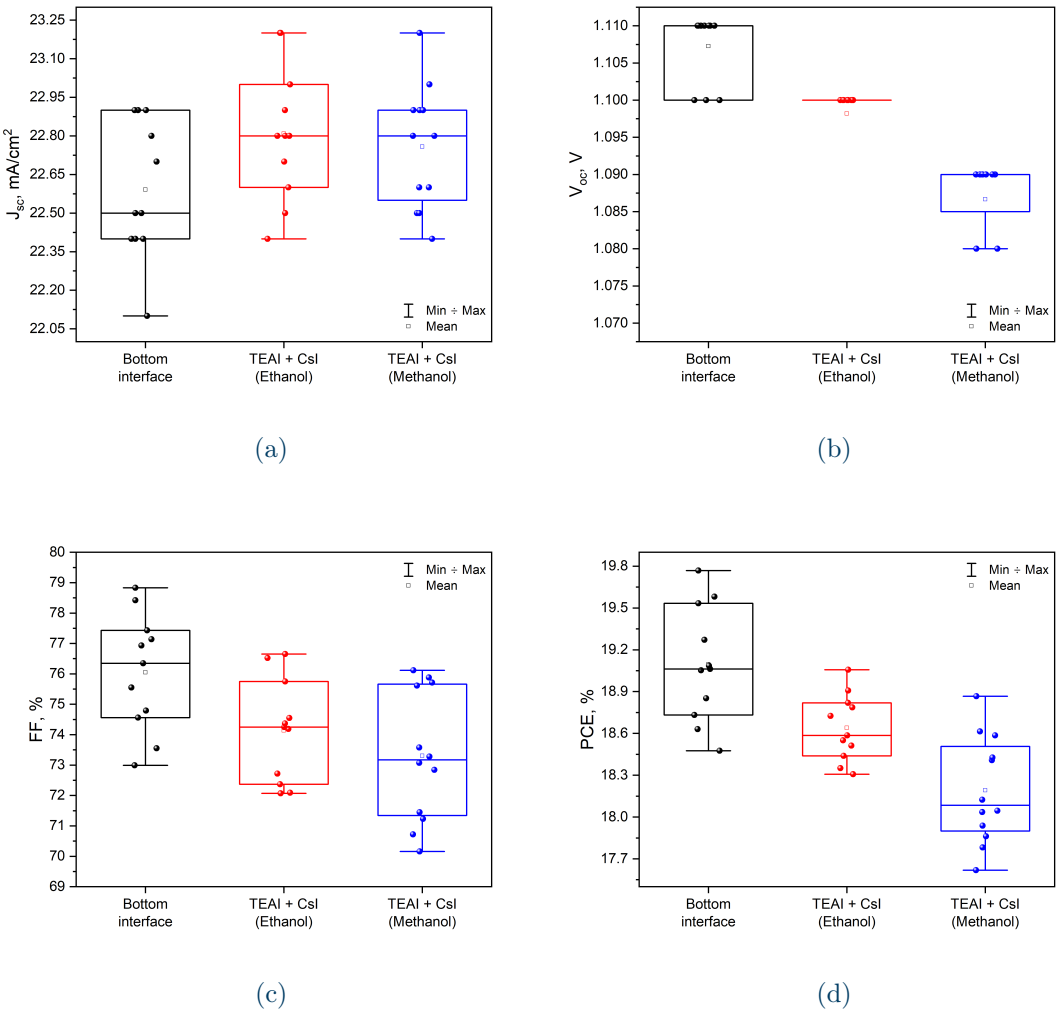

Figure S12: Statistics on (a) J_{sc}, (b) V_{oc}, (c) FF, (d) PCE of cells: *bottom interface* and CsI combined with the protection layer (TEAI).

5.4 Evaporated CsI and CsBr

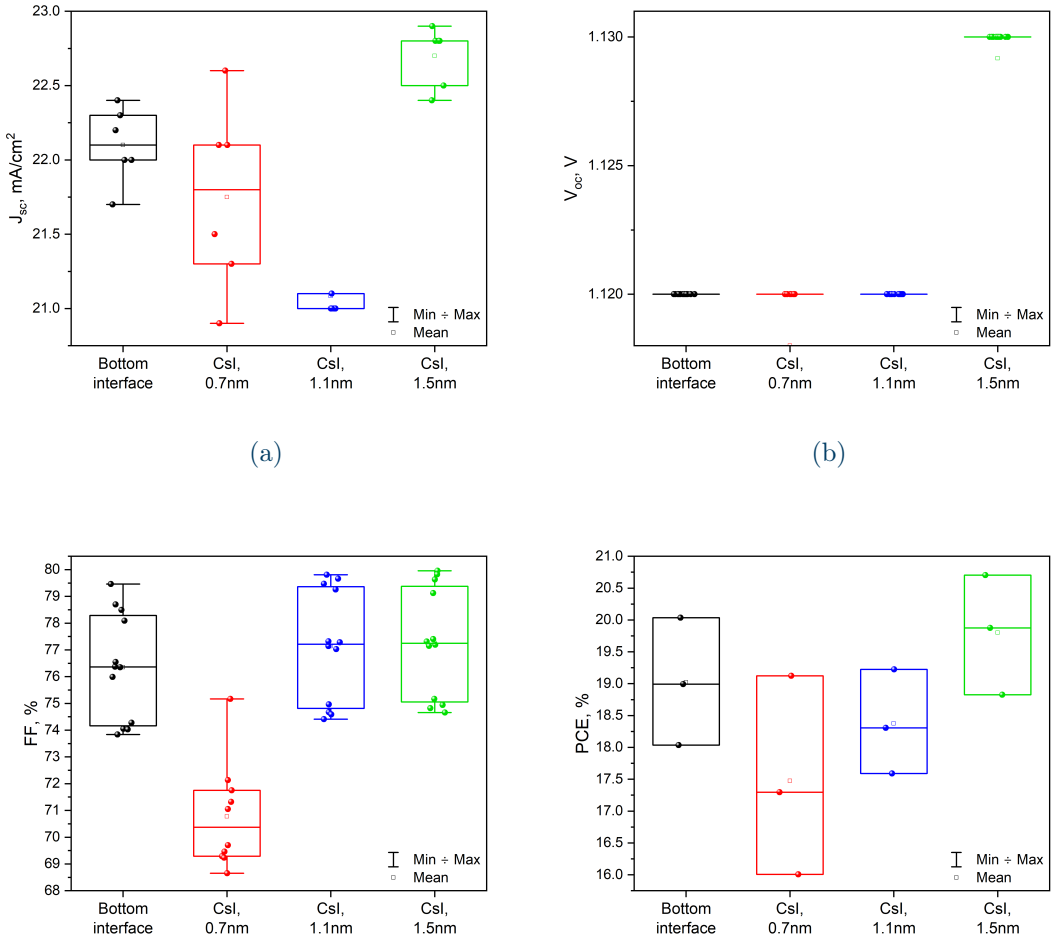

Figure S13: Statistics on (a) J_{sc}, (b) V_{oc}, (c) FF, (d) PCE of cells: *bottom interface* and evaporated CsI.

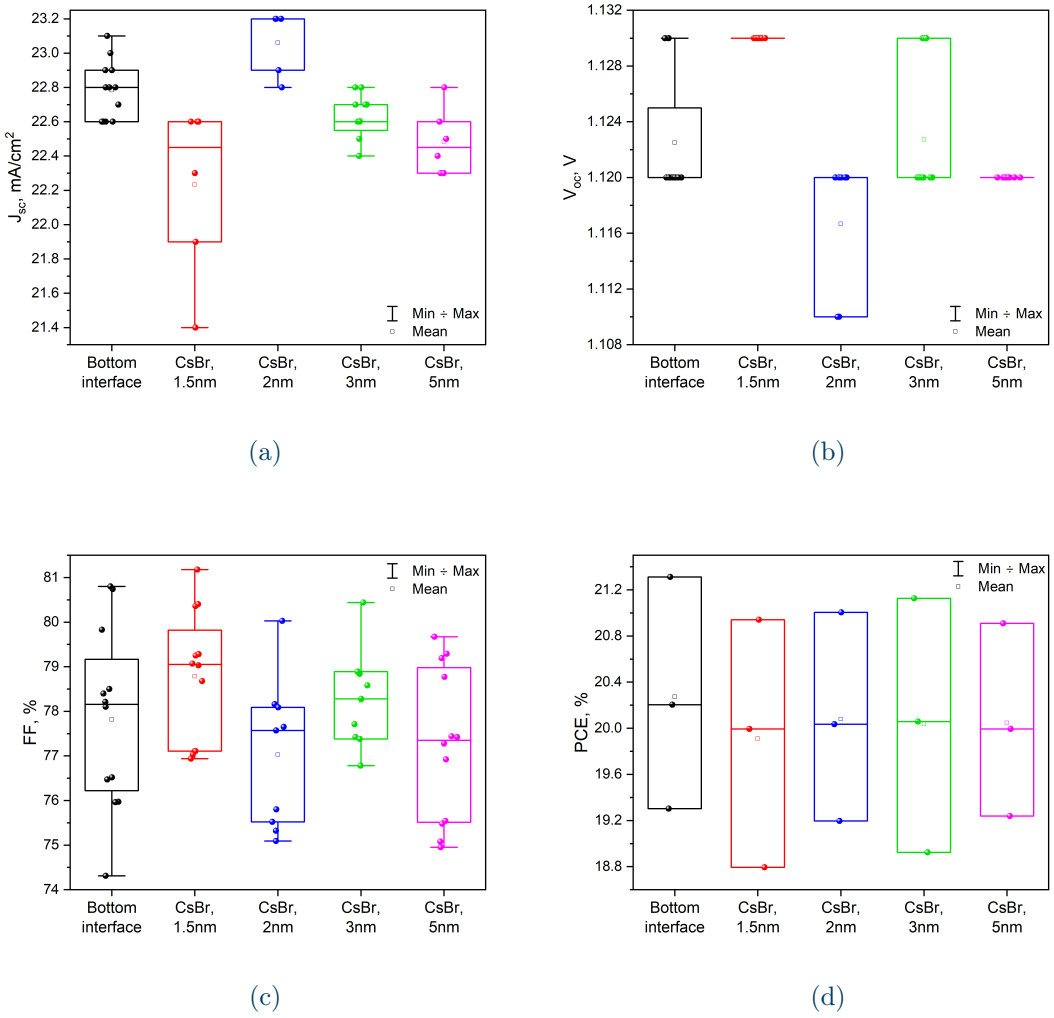

Figure S14: Statistics on (a) J_{sc}, (b) V_{oc}, (c) FF, (d) PCE of cells: *bottom interface* and evaporated CsBr.

5.6 Characterizations and tests

Layer	Material	Deposition	Thickness/ Concentration
HTL	Nickel oxide	DC sputtering	15 nm
Perovskite	Lead iodide	Thermal evaporation	200 nm
	Organic solution	Spin coating and annealing	0.43M
Additional layer	CsI	Thermal evaporation	3nm
ETL	Lithium fluoride	Thermal evaporation	0.8 nm
	Carbon 60	Thermal evaporation	30 nm
	Bathocuproine	Thermal evaporation	5 nm
Metal	Silver	Thermal evaporation	100 nm

Table S9: *Reference + CsI* cell.

Layer	Material	Deposition	Thickness/ Concentration
HTL	Nickel oxide	DC sputtering	15 nm
Additional layer	Me-4PACz	Spin coating and rinsing	0.33mg/ml
Perovskite	Lead iodide	Thermal evaporation	200 nm
	Organic solution	Spin coating and annealing	0.43M
Additional layer	CsI	Thermal evaporation	3nm
ETL	Lithium fluoride	Thermal evaporation	0.8 nm
	Carbon 60	Thermal evaporation	30 nm
	Bathocuproine	Thermal evaporation	5 nm
Metal	Silver	Thermal evaporation	100 nm

Table S10: *Bottom interface + CsI* cell.

5.5 Thermal stability test

Reference	Reference + CsI (no LiF)	Reference + CsI
Nickel oxide	Nickel oxide	Nickel oxide
Perovskite	Perovskite	Perovskite
-	CsI	CsI
LiF C_{60} BCP	- C_{60} BCP	LiF C_{60} BCP
ITO	ITO	ITO
Silver	Silver	Silver

Table S11: Reference, *reference + CsI (no LiF)* and *reference + CsI* devices (used for the thermal stability test in figure 5.4).

Bottom interface	Bottom interface + CsI (no LiF)	Bottom interface + CsI
Nickel oxide	Nickel oxide	Nickel oxide
Perovskite	Perovskite	Perovskite
Me-4PACz	Me-4PACz	Me-4PACz
-	CsI	CsI
LiF C_{60} BCP	- C_{60} BCP	LiF C_{60} BCP
ITO	ITO	ITO
Silver	Silver	Silver

Table S12: *Bottom interface*, *bottom interface + CsI (no LiF)* and *bottom interface + CsI* devices (used for the thermal stability test in figure 5.5).

5.6.1 External quantum efficiency

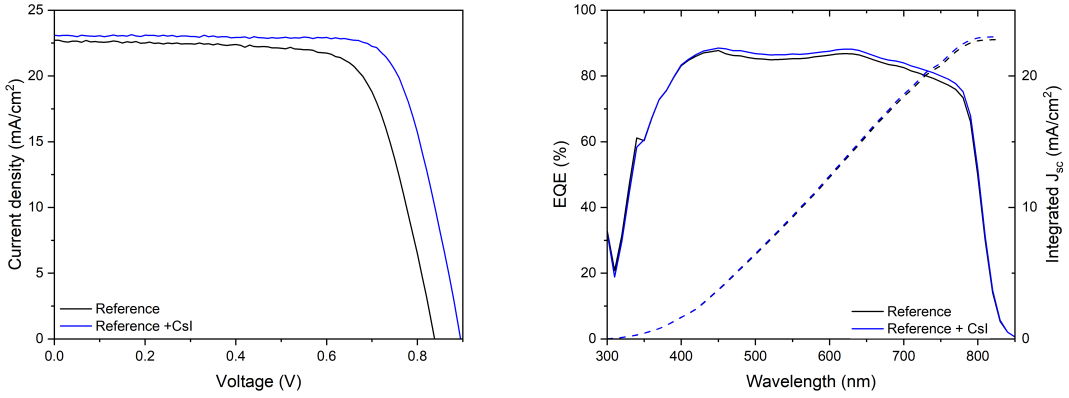

(a) (b)

Figure S15: (a) J-V curves and (b) EQE spectra and the integrated Jsc of reference and *reference + CsI* devices.

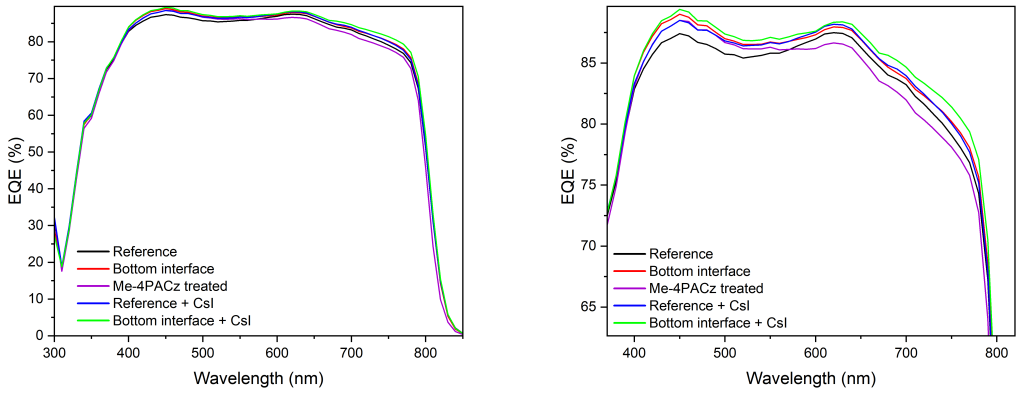

(a) (b)

Figure S16: (a) EQE spectra of all types of cells and (b) zoom on the central part.

Type of cell	Integrated J_{sc}	Measured J_{sc}
Reference	22.93 mA · cm^{-2}	22.7 mA · cm^{-2}
Bottom interface	23.16 mA · cm^{-2}	22.8 mA · cm^{-2}
Me-4PACz treated	22.69 mA · cm^{-2}	21.8 mA · cm^{-2}
Reference + CsI	23.14 mA · cm^{-2}	23.2 mA · cm^{-2}
Bottom interface + CsI	23.36 mA · cm^{-2}	24.1 mA · cm^{-2}

Table S13: Integrated (from the EQE) and measured J_{sc} for all types of cells.

5.6.2 Photoluminescence

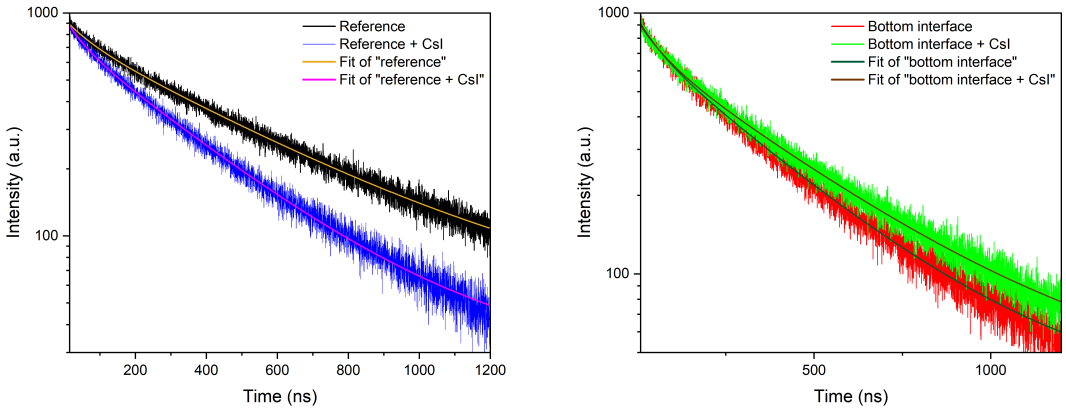

(a) (b)

Figure S17: TRPL of (a) reference and *reference + CsI* cells and (b) *bottom interface* and *bottom interface +CsI* cells.

	Reference	Reference + CsI	Bottom interface	Bottom interface + CsI
A_1	150.48 ± 4.88	179.78 ± 3.82	179.99 ± 4.22	199.24 ± 4.97
τ_1	(73.52 ± 4.37) ns	(53.41 ± 2.12) ns	(58.38 ± 2.52)ns	(71.04 ± 2.82) ns
A_2	743.19 ± 3.95	741.77 ± 3.59	739.02 ± 3.90	693.06 ± 4.37
τ_2	(488.86 ± 6.32) ns	(338.70± 2.40)ns	(362.50 ± 3.0) ns	(426.94 ± 4.96)ns

Table S14: Parameters of the TRPL exponential fit for reference, *reference + CsI*, *bottom interface* and *bottom interface + CsI* cells.

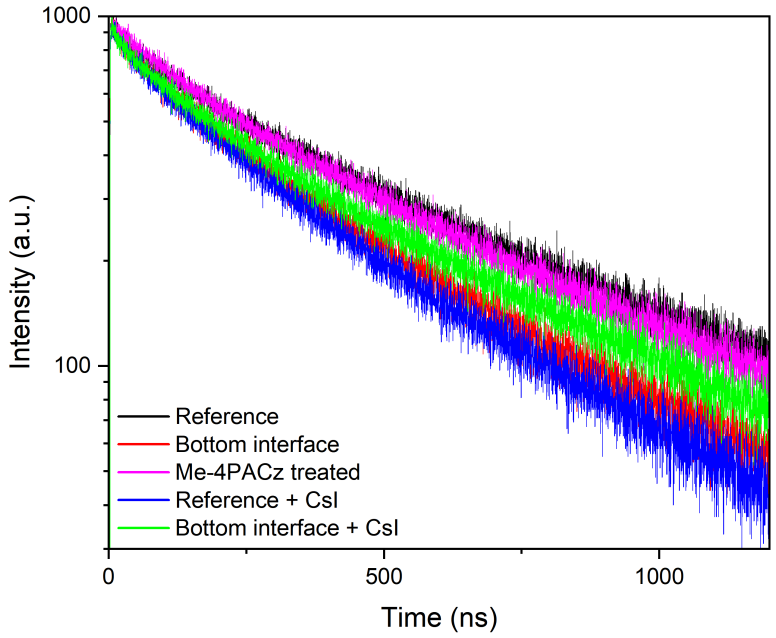

Figure S18: Time-resolved photoluminescence of all the types of cells.

	Reference	**Bottom interface**	**Me-4PACz treated**	**Reference + CsI**	**Bottom interface + CsI**
A_1	150.48 ± 4.88	179.99 ± 4.22	188.07 ± 8.16	179.78 ± 3.82	199.24 ± 4.97
τ_1 [ns]	73.52 ± 4.37	58.38 ± 2.52	92.76 ± 4.86	53.41 ± 2.12	71.04 ± 2.82
A_2	743.19 ± 3.95	739.02 ± 3.90	747.58 ± 6.97	741.77 ± 3.59	693.06 ± 4.37
τ_2 [ns]	488.86 ± 6.32	362.50 ± 3.0	470.10 ± 7.77	338.70± 2.40	426.94 ± 4.96

Table S15: Parameters of the TRPL exponential fit for all the cells.

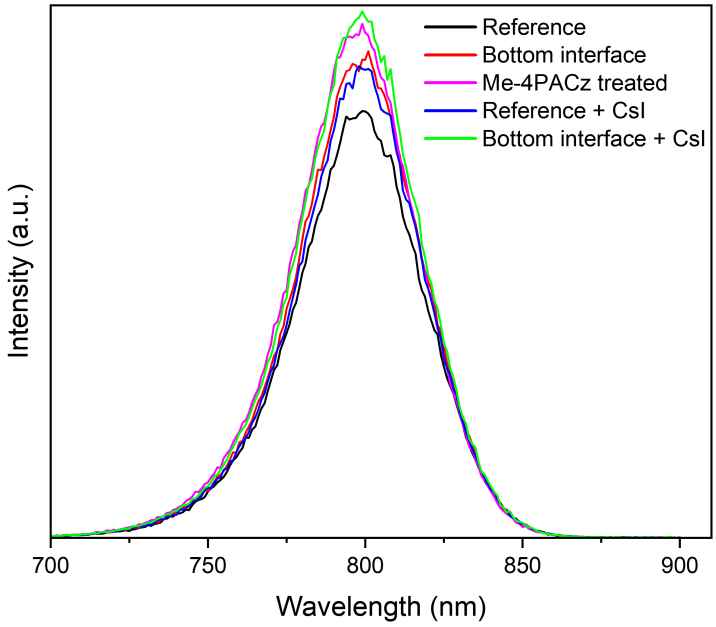

Figure S19: Steady-state photoluminescence of all the types of cells.

5.6.4 Transient photocurrent and photovoltage

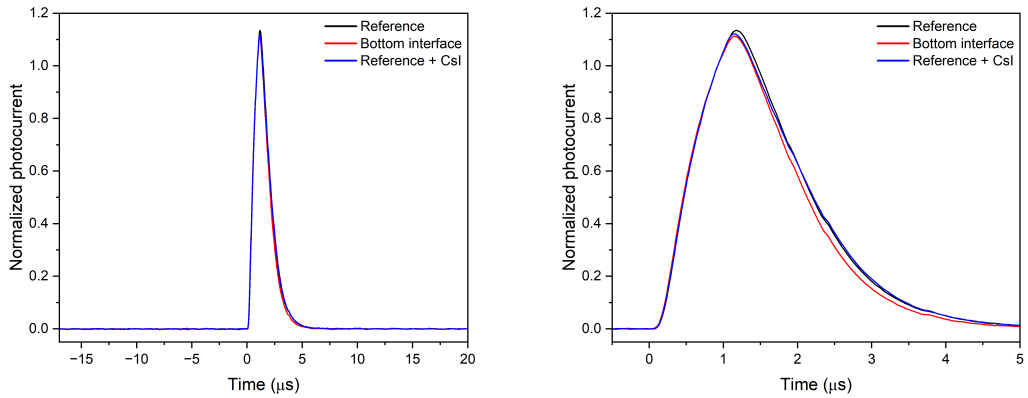

(a) (b)

Figure S20: (a) TPC analyses of reference, *bottom interface* and *reference + CsI* cells and (b) zoom on the peak.

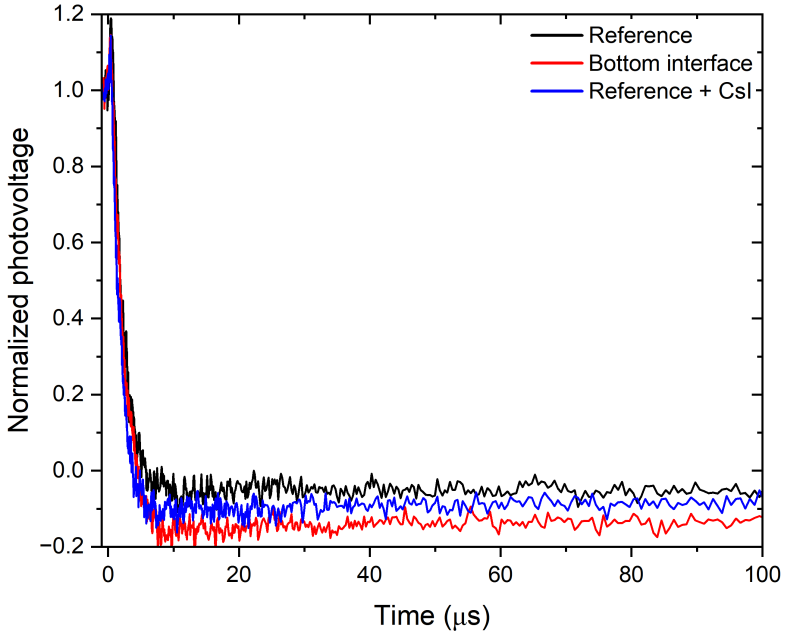

Figure S21: Transient photovoltage analyses of reference, *bottom interface* and *reference + CsI* cells.

Decay constant	Reference	Bottom interface	Reference + CsI
TPC	1.19 μs	1.14 μs	1.23 μs
TPV	1.56 μs	1.61 μs	1.20 μs

Table S16: Decay constants of the TPC and TPV anaylses: reference, *bottom interface* and *reference + CsI* cells.

5.6.5 X-ray diffraction

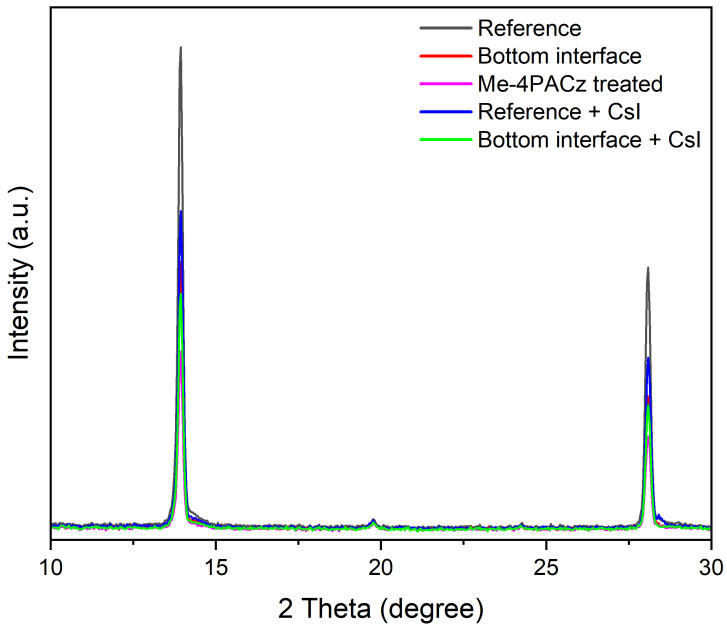

Figure S22: X-ray diffraction of all the types of cells.

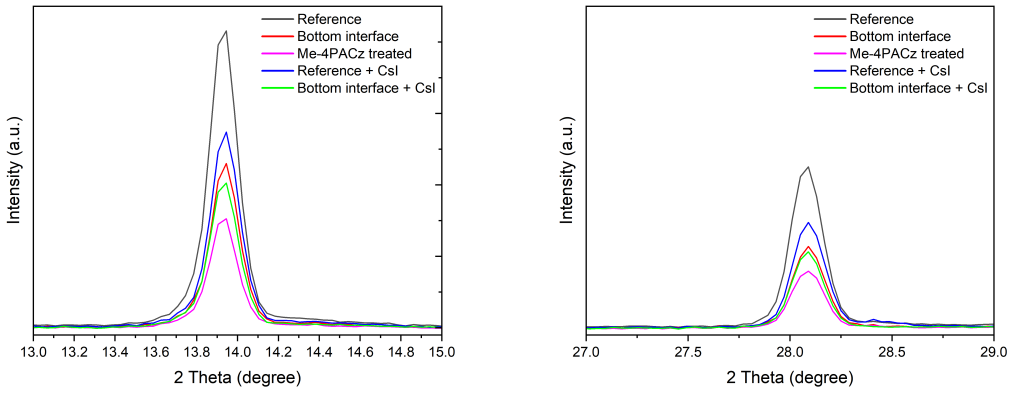

(a) (b)

Figure S23: Zoom on (a) first and(b) second peak in the XRD plot of all types of cells.